Department
Chemie und Pharmazie

FRIEDRICH-ALEXANDER
UNIVERSITÄT
ERLANGEN-NÜRNBERG

NATURWISSENSCHAFTLICHE
FAKULTÄT

Scanning Tunneling Microscopy and Atomic Force Microscopy Studies on the Structure and Growth of Ionic Liquids on Au(111)

Rastertunnelmikroskopie- und Rasterkraftmikroskopieuntersuchungen zu Struktur und Wachstum Ionischer Flüssigkeiten auf Au(111)

Der Naturwissenschaftlichen Fakultät der
Friedrich-Alexander-Universität Erlangen-Nürnberg
zur Erlangung des Doktorgrades

Dr. rer. nat.

vorgelegt von
Manuel Meusel
aus Fürth

Als Dissertation genehmigt von der Naturwissenschaftlichen Fakultät
der Friedrich-Alexander-Universität Erlangen-Nürnberg

Tag der mündlichen Prüfung:	14.02.2022
Vorsitzender des Promotionsorgans:	Prof. Dr. Wolfgang Achtziger
Gutachter:	Prof. Dr. Hans-Peter Steinrück
	Prof. Dr. Jörg Libuda

TABLE OF CONTENTS

LIST OF PAPERS; [P1-P4] IN THE APPENDIX

[P1] Atomic Force and Scanning Tunneling Microscopy of Ordered Ionic Liquid Wetting Layers from 110 K up to Room Temperature

M. Meusel, M. Lexow, A. Gezmis, S. Schötz, M. Wagner, A. Bayer, F. Maier, and H.-P. Steinrück

ACS nano, *14*, 9000-9010 (**2020**)

10.1021/acsnano.0c03841

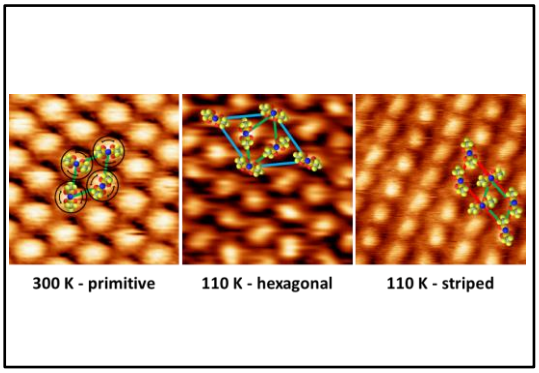

[P2] Growth of Multilayers of Ionic Liquids on Au(111) Investigated by Atomic Force Microscopy in Ultrahigh Vacuum

M. Meusel, M. Lexow, A. Gezmis, A. Bayer, F. Maier, and H.-P. Steinrück

Langmuir, 36, 13670-13681 (**2020**)

10.1021/acs.langmuir.0c02596

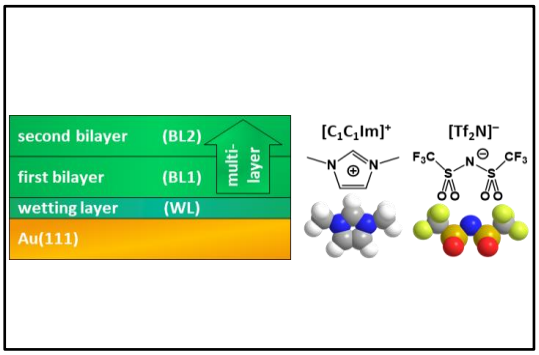

[P3] Time- and Temperature-Dependent Growth Behavior of Ionic Liquids on Au(111) Studied by Atomic Force Microscopy in Ultrahigh Vacuum

M. Meusel, A. Gezmis, S. Jaekel, M. Lexow, A. Bayer, F. Maier, and H.-P. Steinrück

J. Phys. Chem. C,
125, 20439-20449 (**2021**)

10.1021/acs.jpcc.1c06613

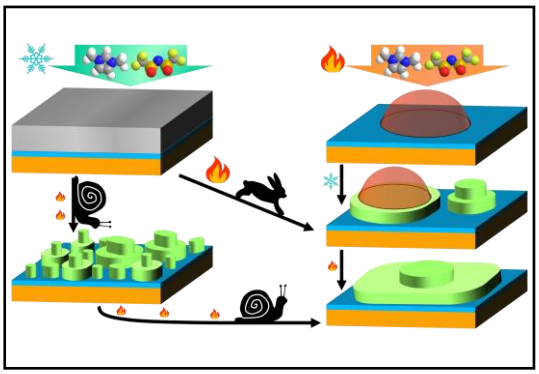

[P4] Growth and stability of Pt nanoclusters from 1 to 50 atoms on h-BN/Rh(111)

F. Düll*, M. Meusel*, F. Späth, S. Schötz, U. Bauer, P. Bachmann, J. Steinhauer, H.-P. Steinrück, A. Bayer, and C. Papp

Phys. Chem. Chem. Phys.,
21, 21287-21295 (**2019**)

10.1039/C9CP04095A

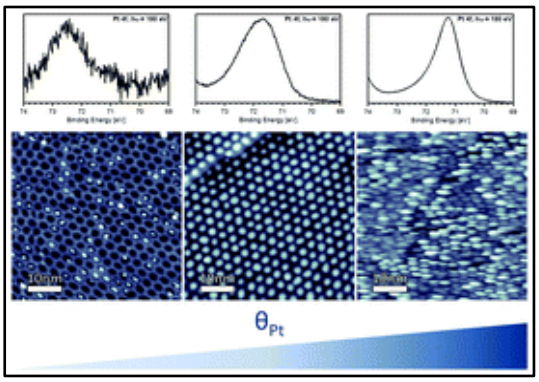

*shared first-authorship. The author's contribution is the STM part.

1. INTRODUCTION

Ionic liquids (IL) are a fascinating class of substances with several unique properties that are interesting for various fields of applications. Although ILs were known for more than a century, the scientific interest has only started to increase within the last two decades.[1-6] Due to the typically low vapor pressure of ionic liquids,[7-11] they are applicable as a liquid component within vacuum conditions and could allow for technical advancements that were out of reach with other materials.[12] As solvents with ionic character, ILs are a natural choice for electrolytes in electrochemistry[13-24] or for catalytic processes.[25-40] This even stimulated novel catalytic concepts such as "supported ionic liquid phase" (SILP)[27-31] and "solid catalyst with ionic liquid layer" (SCILL).[35] Both concepts involve a porous particle support, typically an oxide, that is coated with a thin layer of ionic liquid. In case of SILP, the catalyst is dissolved in the IL film and the reaction takes place as homogeneous catalysis. In SCILL, the catalyst is usually a metal nanoparticle that is dispersed on the support. The reaction is a heterogeneous type with the catalytic center located at the interface between IL and metal particle. The structure and stability of this metal-IL interface is therefore of fundamental importance for the catalytic reaction and strongly impacts the performance of the SCILL system.[1, 4, 37, 41-42]

This thesis aims to open pathways that lead towards a better understanding of the structure and fundamental processes at these ionic liquid to metal nanoparticle interfaces. This objective, however, requires breaking down a very complex system (porous particles with dispersed nanoparticles that are covered with an unconventional liquid at variable temperature and pressure) into smaller, simplified model systems that are accessible by today's scientific methods. One preferred route is the application of surface science techniques. This often involves single crystalline surfaces. They are frequently used in the field, are easy to prepare and allow for investigating fundamental processes while greatly reducing the complexity of real systems to an individual crystal facet. The experiments are often performed in ultrahigh vacuum (UHV) conditions, not least because many surface science methods require or highly benefit from such conditions; however, many techniques are also applicable in ambient conditions.

Multiple techniques such as X-ray photoelectron spectroscopy (XPS), UV photoelectron spectroscopy (UPS), reflection adsorption infrared spectroscopy (RAIRS), X-ray or neutron reflectivity, grazing incidence X-ray diffraction, sum-frequency generation (SFG),

helium ion scattering, and electrochemical methods have led to valuable insights, both in UHV and ambient conditions or even *in-operando*.[4, 42-44] On the microscopic side, the group of scanning probe microscopies offers various techniques for detailed characterization with broad applicability ranging from investigations of single atoms in a highly controlled clean environment over AFM force-distance curves to potential-dependent in-liquid measurement at ambient conditions.[44-46] Those methods, and especially their combination, yielded fascinating insights on ultrathin IL films on metal surfaces. For excellent reviews on the advances in the field the reader is recommended to Hayes *et al.* and Lexow *et al*..[6, 47] Some milestones are highlighted in the following.

One of the first discoveries was the checkerboard structure of the very first layer of 1,3-dimethylimidazolium bis[(trifluoromethyl)sulfonyl]imide ([C_1C_1Im][Tf_2N]) as well as 1-methyl-3-octylimidazolium bis[(trifluoromethyl)sulfonyl]imide ([C_8C_1Im][Tf_2N]) on Au(111).[48] This very first layer is referred to as wetting layer (WL). The checkerboard structure describes an arrangement with anions and cations being adsorbed next to each other, both with direct contact to the substrate. Shortly after the discovery with XPS, the checkerboard structure was also confirmed with STM for [BMP][Tf_2N] on Au(111)[49] and later for a variety of imidazolium- and pyrrolidinium-based ionic liquids. Generally, the formation of a wetting layer appears to be the preferred case and is reported frequently for IL deposition on clean metal and oxide surfaces.[46, 49-60] The special behavior of the WL still holds true if the coverage increases towards multilayers or the interface is investigated within liquid environment. AFM force-distance curves in liquid IL have indicated a reduced thickness and increased stability of the lowest layer at the metal/IL interface.[45, 61-68] The behavior on top of the wetting layer is mainly determined by the specific substrate and ionic liquid. Besides this, the temperature during preparation can influence the structures that evolve.[47] Upon deposition at room temperature, layer-by-layer growth is observed in some cases.[46, 48-49, 52, 54, 69-70] In other cases, large 3D islands form on top of the wetting layer.[52-54, 56, 71-72] Also moderate 3D growth occurs, which is a growth behavior in between 2D and 3D growth. Deposition of ILs at low temperatures often leads to irregular snow-like films (hit-and-stick adsorption).[57-59, 72] Heating can then lead to the formation of 2D layers or 3D islands.[56, 71-72] Furthermore, the growth behavior is prone to influence by contaminations or modifications of the substrate and sometimes also shows time-dependent changes in the structure.[54, 56]

Many of the anteceding findings were derived from spectroscopic investigations (i.e. XPS or UPS). Therefore, one of the major motivations for this thesis was the acquisition of real space information on structure and growth behavior of ionic liquids and to provide microscopic insights into the structure and evolution of ionic liquids at the interface to metallic surfaces; an understanding of the fundamental processes would then in turn allow for the enhancement and development of novel catalytic concepts.

2. METHODS, MATERIALS AND INSTRUMENTAL DETAILS

2.1. SCANNING PROBE MICROSCOPY (SPM)

The following chapter intends to give an overview, highlighting the basic knowledge required for the understanding of the presented data and the functions of the instrument. For fundamentals and in-depth descriptions dedicated publications are advised.[73-76]

Scanning Probe Microscopy (SPM) describes a class of imaging techniques based on an interaction of a probe with a sample in close proximity. The probe is a very sharp tip which spatially limits the interaction to a very small point on the sample. The image is obtained by measuring this interaction at multiple raster points on the sample. The key for this technique is the movement of the tip via piezoelectric actuators that allow for precise spatial positioning down to the sub-picometer regime. Due to this locality and in stark contrast to many other microscopic methods, SPM is not limited to the wavelengths of electromagnetic or matter waves. This allows for atomic resolution while remaining remarkably nondestructive compared to other techniques achieving similar resolution. The individual branches of SPM are named after the interaction type that is used in the imaging process.

2.1.1. SCANNING TUNNELING MICROSCOPY (STM)

The first member of the class of SPM is the Scanning Tunneling Microscope (STM). It was developed by Gerd Binnig and Heinrich Rohrer in 1982. For this invention, they were honored with the Nobel Prize in 1986.[77-78] The underlying principle is the quantum mechanical tunneling effect. At a small enough distance, the wave-functions of tip and sample overlap and electrons can tunnel from tip to sample and *vice versa* through vacuum. By applying a voltage bias, the tunneling probability becomes larger in one direction and a tunneling current is generated. This current is amplified, measured and for most modes used in a feedback loop to readjust one of the measuring parameters. An exact theoretical description of the tunneling process itself is complicated since it is time-dependent, three dimensional, multiple electrons are involved, and the exact shape of the tip is often unknown. The most common approximation is the Tersoff-Hamann Model.[79] It approximates the tips wave function by an s-wave and yields a proportionality

between the tunneling current and the local density of states (LDOS) of the sample at the Fermi level. The resolution of STM is thereby only limited by tip curvature and the vacuum gap distance. Within this description, an STM image does not simply reflect the topographical height of the sample, but a superposition of the topographical height and the LDOS of the sample. More figuratively spoken, the tip portraits the contour of electron density around the surface atoms (Figure 1).

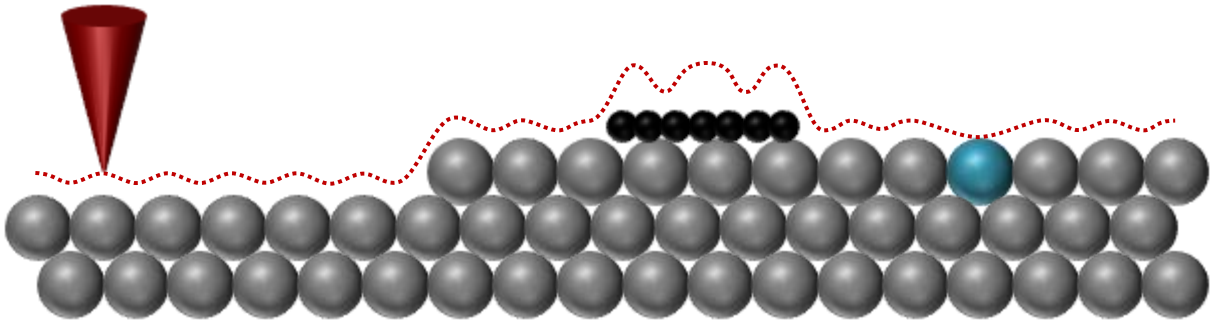

Figure 1: Schematic depiction of the measured height in STM (red tip and red dotted line). As an example, the LDOS of the substrate, and therefore the apparent height in STM, can be superposed with orbitals of an organic molecule (black), or be influenced by a substrate contamination (blue).

STM can be operated in several modes. The most common one is the constant current mode, where a feedback loop re-regulates the height at any scan point so that the tunneling current is held at a set value. This yields a simple and easy interpretable height map; however, it is superimposed by the electronic structure of the surface. A sufficiently sharp STM tip for atomic resolution can be prepared by simply cutting a Pt/Ir wire with a side cutter. If the tip is in a non-beneficial shape for measuring, this often can be improved by short voltage pulses or intentional crashes with the surface. STM does not require the regulation of an oscillation and is therefore much faster compared to other SPM techniques. For those reasons, the main advantage of STM is its simplicity. The main disadvantage, however, is that it requires a conductive sample. To some extent, it is still possible to apply STM to nonconductive materials.[80-81] With isolated tips, it is also possible to operate an STM within liquid environment,[82-84] but a large group of materials is not accessible by STM due to missing conductivity. To access most salts or oxides, a different probing interaction is necessary that is not reliant on electric current. This leads to another branch of SPM, the atomic force microscopy.

2.1.2. Atomic Force Microscopy (AFM)

The first atomic force microscope (AFM) was developed only three years after the STM in 1985 by Gerd Binnig, Calvin Quate und Christoph Gerber.[85] In contrast to STM, the concept bases on the measurement of a vertical dislocation of a cantilever with a sharp tip at the front (instead of only a tip that is brought close or in contact to a sample). Forces between tip and sample bend the cantilever or influence its vibrational properties, what can be measured and used to obtain an image. Multiple attractive and repulsive forces contribute to the overall force-distance relation, ranging from electrostatic, magnetic, van-der-Waals, and capillary forces to quantum mechanical effects, as Pauli repulsion or the Casimir effect.[74-76] Additionally, those forces often have short- and long-range components. A correct theoretical description including all these forces would be very complex. Therefore, a model system is employed. In most cases, the Lennard-Jones potential is used,[75]

$$U(r) = 4U_e\left[\left(\frac{r_0}{r}\right)^{12} - \left(\frac{r_0}{r}\right)^{6}\right]$$

with U_e as the potential minimum, r as the atomic distance and r_0 as the distance when U(r) equals zero (Figure 2). It offers good results with an attractive part of $(r_0/r)^6$ and a repulsive component of $(r_0/r)^{12}$. However, this is an empirical description and the actual force-distance relation slightly varies between different substrate-tip combinations.

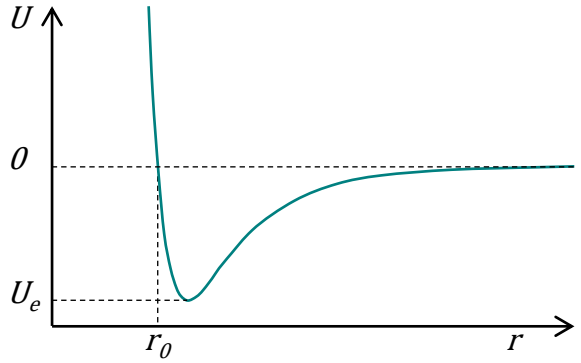

Figure 2: Graphical depiction of the Lennard-Jones Potential.

The classification of AFM modes is not very strict and often terms are used synonymously. AFM is distinguished into static and dynamic, or into contact and noncontact. The difference between dynamic and static techniques is whether the cantilever is stimulated to vibrate or not. For example, the non-contact AFM (NC-AFM) refers to a dynamic mode in the long-range regime of the forces where the shape of tip and sample mostly remain unchanged during measurement. For all dynamic modes, the cantilever is stimulated to vibrate, usually at or near its resonance frequency, and regulated via a feedback cycle. Forces on the cantilever will shift the eigenfrequency of the cantilever and therefore change the resonance amplitude and the phase shift of the regulation. One of these parameters is fed back into the feedback loop and the regulation parameter is adjusted. The parameters, which are used for regulation define the measuring mode. For example, in case of a frequency modulated AFM (FM-AFM) the shift in the resonance frequency is detected and the height of the tip is re-regulated in a way, that the frequency shift Δf remains at a constant pre-set value.

While the first concept of Binnig, Quate and Gerber used an STM to determine the dislocation of the AFM cantilever, the most common method today is the beam deflection approach, where a laser is reflected from the backside of the cantilever. Forces on the tip bend the cantilever, the laser reflection is deflected, and finally detected at a segmented photodiode.[86] With four-segmented photodiodes not only the vertical, but also the horizontal dislocation, and therefore shear forces, can be measured. Another option to measure the dislocation of the cantilever is the Q-Plus approach developed by Franz Giessibl.[87] It combines the high precision of piezo actuators with the high vibrational stability of a quartz tuning fork. Q-Plus sensors can achieve high resolutions, especially at low temperatures in UHV and often allow for performing AFM and STM simultaneously.[88] Q-Plus sensors have typically very high quality factors (Q-factors). This Q-factor is one of the main characteristics of a cantilever. It has higher values with lower energy loss per oscillation cycle what strongly benefits stability and resolution.[74, 87]

2.2. MATERIALS

2.2.1. SINGLE CRYSTALLINE SURFACES

Surface science works best in extremely well-defined conditions. Investigated surfaces are therefore often single crystalline substrates with a defined crystallographic orientation. The face centered cubic (fcc) (Figure 3 a) and the hexagonal close packing (hcp) crystal structures are the two structures with the closest possible packing density for identical spheres. They differ in the stacking sequence of planes; stacking in A-B-A fashion yields an hcp lattice and A-B-C forms an fcc lattice. Crystalline materials have a defined geometry and the structure of an interface highly depends on the angle of the surface plane relative to the crystallographic main directions. This orientation or structure of a crystallographic surface is described by Miller indices, in brackets. For fcc crystals, the (111) surface (Figure 3 b) is an especially stable surface. It has a hexagonal structure with high symmetry vectors in <110> directions. However, single crystalline surfaces are never perfectly flat or defect free. Slight variations in roughness or angular aberration lead to abrupt step edges between terraces of highly crystalline surface. Step edges, defects, contaminations or special points in reconstructions (like the corners in the herringbone structure of the Au(111) 22x$\sqrt{3}$ reconstruction; discussed below), are often preferential adsorption sites and sometimes even catalytically active.

The 22x$\sqrt{3}$ Herringbone Reconstruction of Au(111)

Reconstructions on a crystalline surface are formed if a rearrangement of the surface is energetically favored over the structure of the bulk crystal. This leads to different surface unit cells and therefore a reconstruction is described via length multiplicators of the base unit cells vectors. Examples are the 7x7 reconstruction of Si(111) or the 22x$\sqrt{3}$ reconstruction of Au(111).[89] The Au(111) reconstruction (Figure 3 d) origins from a one dimensional compression of the generally hexagonal surface. This leads to a surface structure that alternates between fcc- or hcp-like regions of the topmost layer relative to lower layers. This results in a double-striped appearance that alternates its orientation between the three available high symmetry directions of the substrate and creates a herringbone like appearance. This reconstruction is well visible in AFM and STM and allows for easy determination of the crystallographic directions.

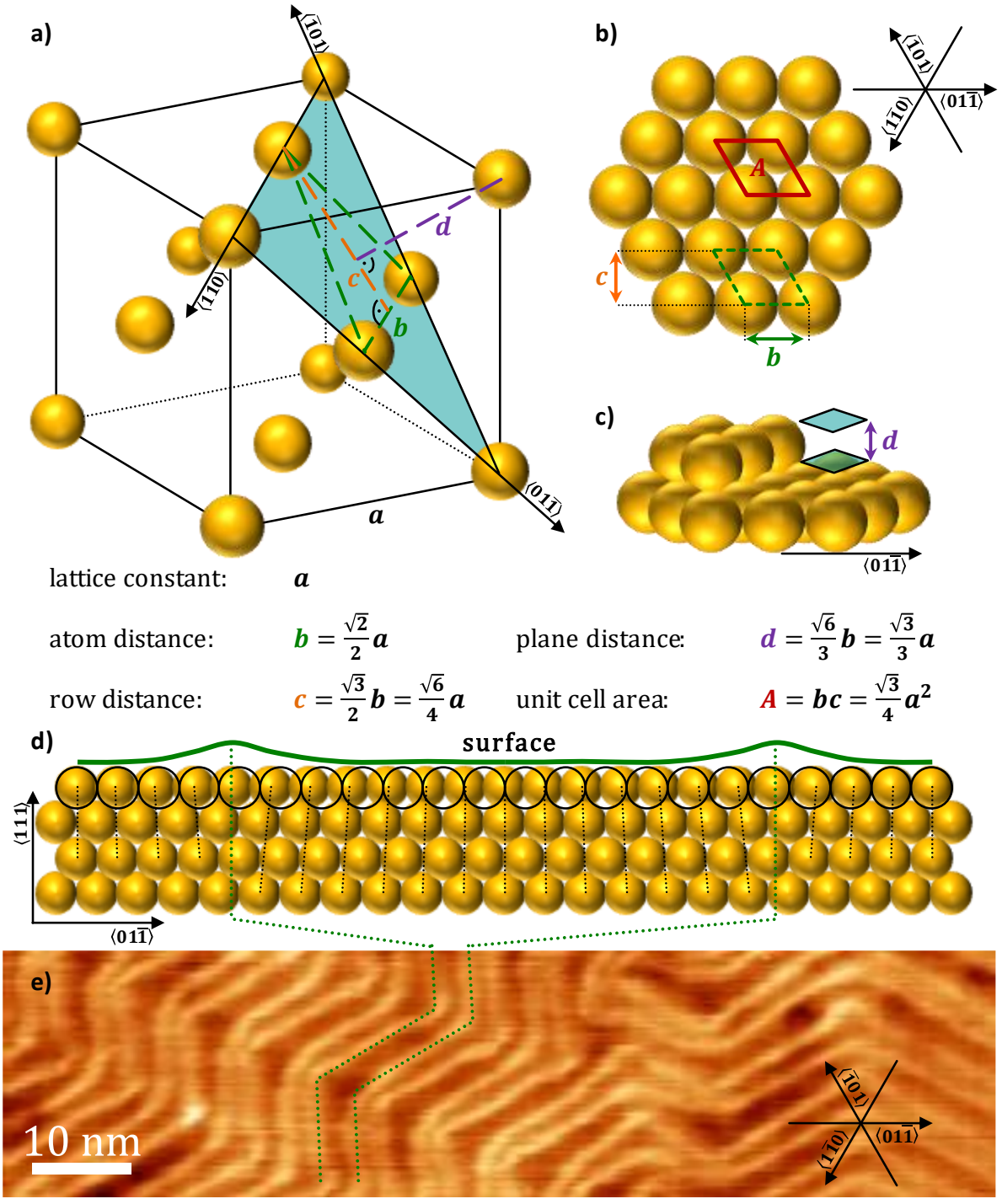

Figure 3: Overview on the face-centered cubic (fcc) crystal structure and the relation to the Au(111) surface reconstruction. a) Unit cell for fcc crystals. The blue triangle highlights a (111) plane with the edges corresponding to high symmetry vectors. Specific distances are drawn with colored lines and the corresponding relation to the lattice constant is presented below. b) Top view of a (111) plane with highlighted surface unit cell. c) Side view of a (111) plane including a step edge. d) Vertical cut of a Au(111) surface. The 22x√3 reconstruction origins from 23 atoms in the top layer being compressed to 22 lattice spacings. The resulting mismatch forms stripe pairs that alternate between the three high symmetry directions and form a herringbone like appearance. e) STM image of a Au(111) surface. U=0.7 V, I=0.5 nA.

Hexagonal Boron Nitride (h-BN) on Rhodium (111)

Hexagonal boron nitride (h-BN) is one of the crystal structures of boron nitride. It is an analogue to graphite with an alternating pattern of boron and nitrogen atoms. Just like graphite, it is composed of single sheets. Analogously to graphene, h-BN can be grown as a 2D sheet on a templating substrate, for example, from borazine via chemical vapor deposition (CVD).[90-92] In most cases, the lattice constants of the substrate and the 2D structure on top are not identical. This lattice mismatch results in a Moiré pattern. On large scales this mismatch would cause tension, which is corrected by vertical corrugation effects. The resulting surface offers a vertical structuring depending on the combination of substrate and 2D material.[93] In the case of h-BN on Rh(111), the Moiré pattern is a honeycomb like pattern with so called pores, where the h-BN sheet is close to the substrate. The rims of these pores, with a larger distance to the substrate, are referred to as wires. For h-BN on Rh(111), the transition between pore and wire is especially abrupt and offers a high energy barrier. For this reason, this Moiré structure can be used as a template for the growth of nanostructured materials like nanoclusters with narrow size distribution.[94-99]

2.2.2. IONIC LIQUIDS (ILS)

Ionic liquids (ILs) are salts with a very low melting point, per definition below 100°C, and a very low vapor pressure.[100-103] Often their melting point is even below room temperature. The low vapor pressure makes ILs vacuum stable and allows for the usage in liquid phase under vacuum conditions. These properties are achieved by the selection of ion combinations with strong steric hindrance to reduce the lattice energy. ILs are highly tunable by the selection of different anion-cation combinations.[1, 25-26, 104] Typical cations are imidazolium, pyridinium or pyrrolidinium based ions, usually with one longer alkyl substituent and one methane group. Other typical cations are quaternary ammonium or phosphonium ions. Typical anions are fluorinated borane, phosphane, or methanesulfonate derivatives, or simply halogenides. Figure 4 shows an overview for common ILs. The alkyl chains can further be functionalized in various ways to tailor specific properties, for example fluorinating the alkyl chains to enrich them at the IL-surface.[105]

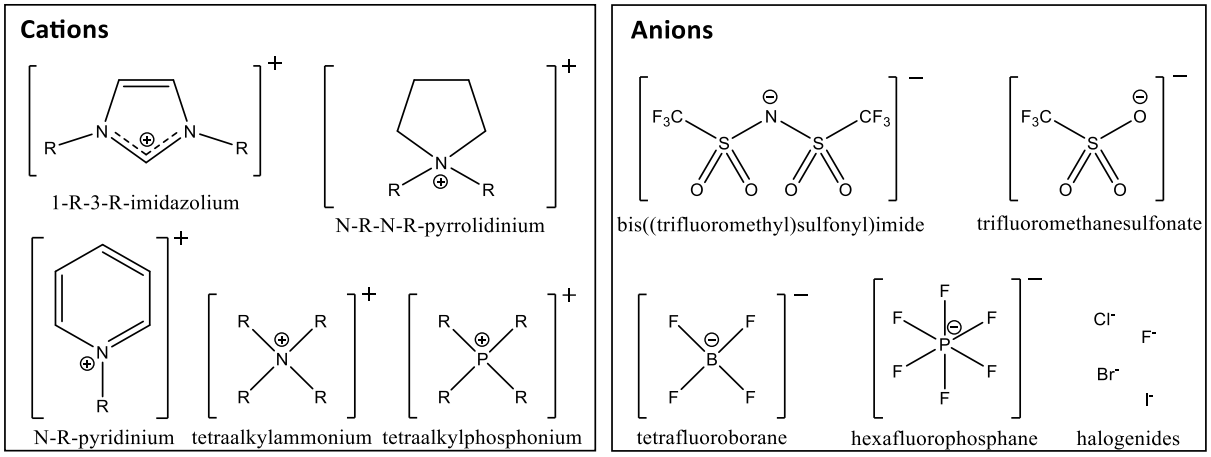

Figure 4: Overview on typical cations (left) and typical anions (right) of ionic liquids. The substituent groups R are typically alkyl chains, functionalized alkyls, or methyl groups.

2.3. DETAILS ON THE INSTRUMENT

The measurements shown in this thesis are performed in an STM and AFM machine with Q+ option from Scienta Omicron intended for variable temperatures between 90 and 500 K (VT-AFM-Q+-XA). It is a two-chamber UHV setup containing the analysis chamber with the microscope, the preparation chamber equipped with LEED, manipulator, multiple flanges for supplemental devices, and a Load Lock (LL; or Fast Entry Lock: FEL) with separate pumping (see Figure 5). The machine also involves a UHV suitcase for inter-chamber transfer of samples. Further components are an electronics rack with room for additional controllers, and a desktop workspace including the MATRIX electronics and a preinstalled computer. The machine was delivered and initialized 2016/2017. The general machine is described in the manual "PN00659_System_Manual_143725" and the microscope itself in "PN05015 VT AFM XA QPlus V4.3.1". The instrument was later modified in several points and equipped with additional devices.

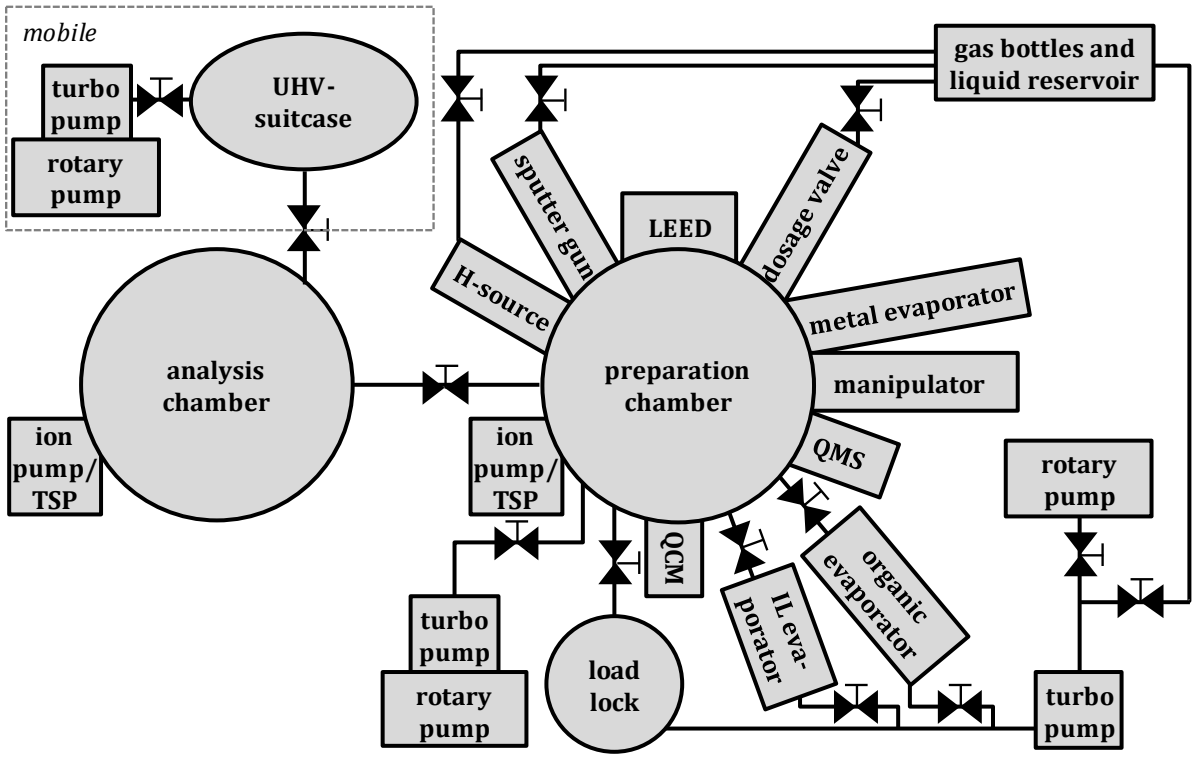

Figure 5: Schematic drawing of the chamber including connected devices and valve setup.

2.3.1. MODIFICATIONS FROM FACTORY STATE

Thermocouples of Manipulator and Sample

In the factory state, one thermocouple (type K) was placed on the manipulator and one at the cooling reservoir of the manipulator. The temperature of the cooling reservoir is of minor importance for our research. Therefore, the thermocouple at the cooling reservoir was removed and a setup for temperature measurement directly on the sample was constructed instead. It involves a special setup on the sample holder that is described in Chapter 2.3.3. The contact between sample and manipulator is made by two pins on the sample, which are pushed into two springs at the side of the manipulator. The design took inspiration from the DASSA chamber (an angle resolved XPS machine at our chair that is designed for liquid samples).[106] The construction of both chambers is very similar; however, the manipulators of each system have different dimensions (i.e., all metallic parts of the sample temperature reading are different). In contrast, the ceramic part is identical and interchangeable. The STM/AFM chamber has one K-type thermocouple, and not both K-type and C-type as used in DASSA. Samples are fully interchangeable between both chambers. Making use of the UHV suitcase, samples can be interchanged under UHV conditions. Technical drawings are provided in the appendix (Figures A1-A5).

Security Switches and Manipulator Z-Drive

The z-Drive of the manipulator is the central function for exchanging samples between analysis chamber, preparation chamber, load lock and UHV suitcase. In the factory state, it was moved via a small crank utilized by hand. A drilling machine was mounted instead, and the maximum rotational speed was decreased via the power supply. To reduce the risk of crashes between manipulator and gate valve, or manipulator and sample lift, security switches and a slider were mounted at the manipulator, gate valve, and at the microbalance. The switches were set up to power the drilling machine only if the manipulator is in a safe position, and give an acoustical warning if not (Figure 6). Technical drawings are provided in the appendix (Figures A6-A7).

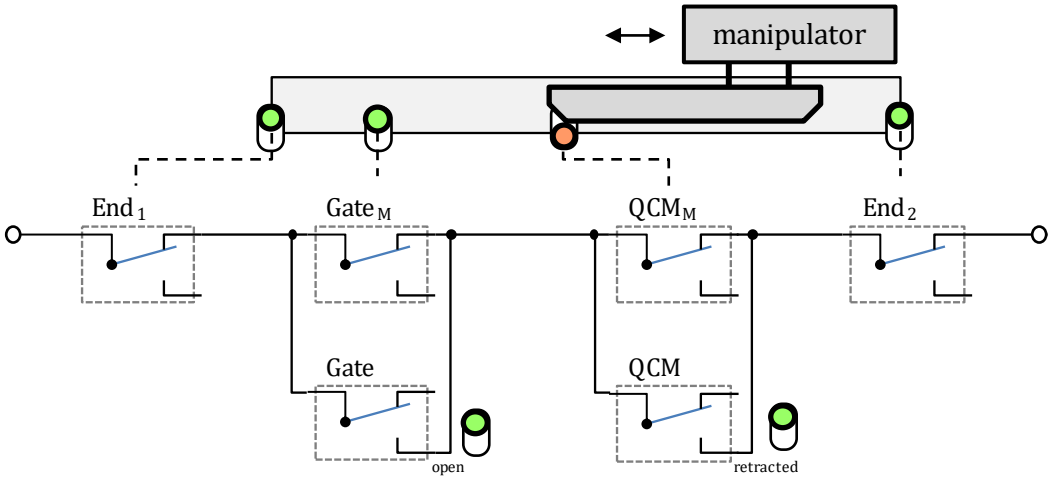

Figure 6: Wiring diagram of the security switches for the manipulator z-drive and schematic drawing of the manipulator. If the manipulator is moved into a non-allowed state (depicted by green and red switches), the power of the z-drive motor is cut, and an acoustic warning is played. This prevents accidental collisions in the machine.

Load Lock

The factory state of the Load Lock (LL) did not offer the option to shut off the pumping without venting the LL. Therefore, a gate valve and a pressure reading were installed, to allow for closing the connection to the pumps while under vacuum but still have a pressure display. Furthermore, a corrugated tube connection with valves on both sides was installed to allow for pumping and baking two evaporators independently from the main chamber (organic and IL evaporator; see Chapter 2.3.2). In addition, a T-pipe with two valves was added at the connection between the roughening pump and the turbopump (see Figure 5). In this way, one pumping line leads towards the LL turbopump and another one leads towards gas lines and dosage valve. With these modifications, gas lines and gas handling system can be evacuated after an exchange of a gas bottle or if required experimentally (see Chapter 2.3.2). Careful utilization is required to not accidently vent the LL turbopump from behind or even the chambers.

Cable Switch for Q+/AFM

The change between AFM and Q+ measurement mode requires the switching of one plug, namely “F_N” (AFM) or ”ω-out” (Q+) into F_N-IN, in the back of the MATRIX electronics. This step was simplified by building a cable extension and a small box with all three plugs that is placed on the desk. The plug can now be changed there.

2.3.2. ADDITIONAL EQUIPMENT

The machine was equipped with additional devices that allow for a versatile set of possible experiments. Details on the single devices can be found in the respective manuals. This chapter aims to highlight mutual complementation and experimental limits that originate from the overall setup.

LEED/Auger

The LEED/Auger (Scienta Omicron SPECTALEED with LaB_6 filament) was included in the factory state of the machine. However, since it is not covered in the main manual of the device, it is mentioned here. The Auger spectroscopy option is built on top of the LEED function and requires both, the Auger- and the LEED-software, to run. While not in use, the LEED screen is covered with a shutter and is retracted. The screen can be damaged by acetone, so for maintenance in the camber, only isopropanol should be used.

Mass Spectrometer

The machine has a Pfeiffer Vacuum (QMA 200, QME 220, QMG 220) quadrupole mass spectrometer (QMS) in the preparation chamber. It covers a range from 0 to 100 atomic units and a pressure up to $1x10^{-4}$ mbar. Until now, it is mainly used for helium leak tests, comparison of background spectra and for identification of impurities in the gas lines. Due to the geometry of the evaporator and QCM flanges, evaporated substances cannot be detected in line of sight by the QCM. It has a distance to the sample of about 15 cm, so TPD would be possible, but the setup is not optimal.

Gas Dosing and Ion Sources

The system is equipped with an ion source for sputtering, an atomic hydrogen source and a dosage valve (Agilent Technologies 9515106) for variable dosing of gases or liquids (see Figure 5). All three devices are connected to an individual gas line and valve setup that uses Linde Minicans (or equivalents, e.g. Air Liquide). The dosage valve is

equipped with a glass vessel that allows for dosing of liquid precursors (as long as the vapor pressure of the liquid is sufficiently high). All gas lines can be pumped via the load lock pumping setup. The SPECS (IQE 11/35) sputter gun is used with Ar. Due to its positioning, opposing the organic and IL evaporators, it is prone to contamination and requires extensive degassing from time to time. The hydrogen source (Focus EFM H) is capable of splitting H_2. It shares the electronics with the metal evaporator.

Evaporators

The machine is equipped with evaporators for metals and organic substances (e.g. porphyrins), and a specialized evaporator for ionic liquids (see Figure 5). Both the organic and the IL evaporator can be refilled without venting the preparation chamber. When performing organic or ionic liquid evaporation, the deposition dose can be determined with a quartz crystal microbalance.

The Organic Evaporator is a OmniVac (EV300) four-fold evaporator that allows for evaporation temperatures up to 720 °C (993 K). The shutter was modified (holes for simultaneous evaporation are blocked with Ta foil) to inhibit unintended contamination.

The IL evaporator was developed in our group especially for evaporation of ILs. It is based on a Tectra KC3-BODY with individualized head. Details on the construction are available elsewhere.[57, 107] Due to the special properties of ILs, it does not possess a shutter. The deposition is started and stopped by moving the sample (via the manipulator) out of or behind a shutter that is mounted on the microbalance. Then the evaporator is retracted and the gate valve is closed. The IL evaporator uses the electronics of the organic evaporator.

The quartz crystal microbalance (QCM) is from Prevac (Quartz balance, TM13, TMC13). Both the organic and the IL evaporation dose can be measured with the QCM. It is not possible to position the QCM at the position of the sample, even with fully retracted manipulator. Instead, it is positioned in the evaporation cone of the respective evaporator (besides the sample). Therefore, it can measure a signal that is proportional to the deposited amount on the substrate. However, this is not an absolute thickness and needs regular calibration for each substance. At the backside of the QCM, a shutter with a 10x20 mm^2 hole is mounted to reduce the amount of contamination deposited on devic-

es in the background of the manipulator (LEED, H-source, sputter gun), and to have a clear transition of free and blocked line of sight between evaporator and sample. It would be possible to install water cooling to the QCM; however, this was not required until now.

The metal evaporator is a Focus (EFM 3T) three-fold evaporator that utilizes metal rods of 40 mm length. It is mounted upside down at the top of the chamber. This is beneficial for soft metals as Cu, because in this way they are less likely to bend when heated. The metal evaporator shares the electronics controller with the hydrogen source.

2.3.3. SAMPLE MOUNTING

The sample plates are standard Scienta Omicron sample plates that are modified for different purposes. The sample setup allows for inter chamber transfer, most importantly, between STM/AFM and DASSA (an angle resolved XPS machine designed for liquids),[106] but also for other machines that use the Scienta Omicron sample plate design. The temperature reading of the samples was designed to be compatible with DASSA, which uses a 4-pin setup with C- and K-type thermocouples (also see Chapter 2.3.1). A C-type is not necessary for STM/AFM and therefore spared out. Samples from DASSA with all four connections also fit in the STM/AFM. Figure 7 shows a mounted Cu(111) single crystal (left) and a Rh(111) single crystal during annealing (right).

The temperature reading on the samples is achieved by mounting a boron nitride ceramic with threads at the backside of the sample (see Figure 7). Two screws made from type-K alloy are screwed into the ceramic and serve as connection pins to springs at the manipulator. Wires (type-K) connect to the point where the temperature is meant to be measured. In case of the single crystals used for this thesis, the wire connects into two holes in the crystal itself. Screws, ceramic and sample plate blanks are interchangeable between STM/AFM and DASSA.

The single crystals were bought from MaTeck and are cylindrical (height 2.0 mm, diameter 8.5 mm, purity 99,9999%, roughness <0.01 µm, alignment < 0,1°), with two notches at the side and two holes (0.3 mm) at the front. They are strapped to the sample plate by two strips of Ta foil. With this setup, the highest protruding part of the sample is the surface of the crystal. This prevents contaminations to be deposited on the sample during sputtering.

Another type of sample holder is the resistive heating sample holder. It does not offer direct temperature reading. Samples as Si can reach much higher temperatures with direct heating; however, it is only suitable for low conductive samples.

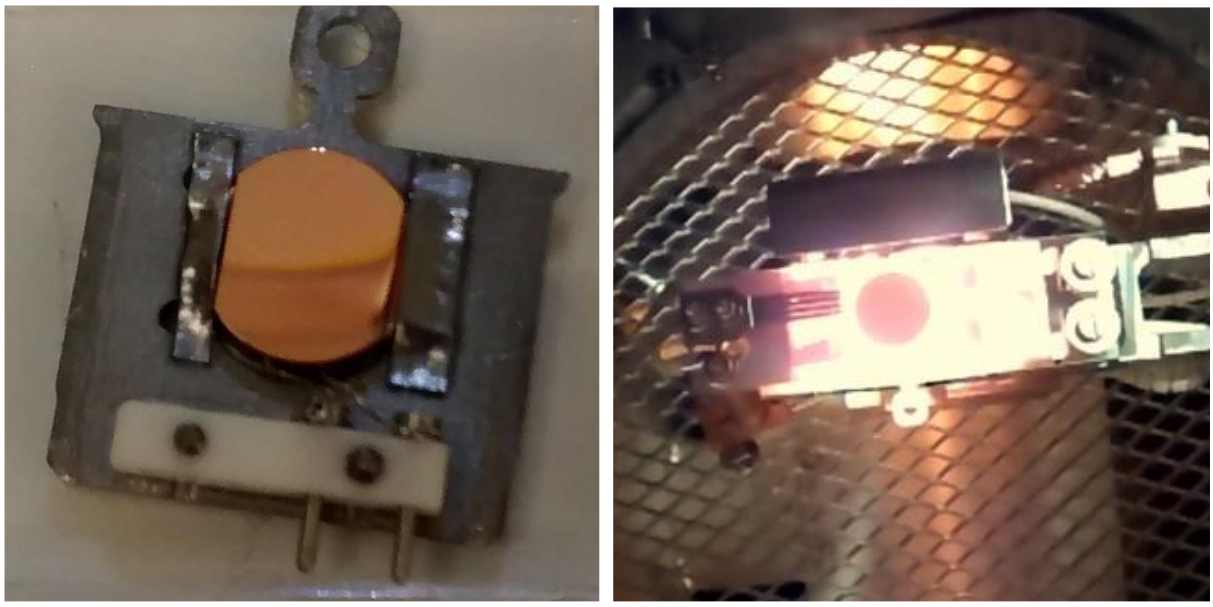

Figure 7: Cu(111) single crystal (left) mounted on the sample plate, with thermocouple connections at the bottom and Rh(111) single crystal (right) during annealing on the manipulator at $T_S \approx 1300$ K.

2.3.4. Range and Limits of Operation Conditions

The instrument has several hard and soft limitations and operation ranges. Limitations, standard parameter, and examples of preparations are summarized in Table A1 in the appendix.

Pressure Ranges

The instrument consists of several devices that can be damaged by sudden pressure changes or utilization in the wrong pressure regime. Both, the preparation and the analysis chamber are secured by an interlock, that is set to $8 \cdot 10^{-5}$ mbar and $1 \cdot 10^{-7}$ mbar. High pressures and pressure spikes will often not destroy parts, but rather contribute to the aging of running filaments. Therefore, the pressure is a soft limit, and it is sometimes acceptable to trespass it to some extent. One important exception is the microscope itself. Additional to operation in UHV, it is possible to operate the STM (not AFM) outside

of the chamber in ambient conditions for testing. However, the operation of the coarse motor in the pressure regime in between UHV and ambient (10^{+1} to 10^{-3} mbar) is dangerous due to the possibility of corona discharges. This will manifest itself in the coarse motor controller displaying an overload error message.

Temperature Ranges

Temperature is the most versatile parameter since several components and conditions are counter influencing the limits here. The sample stage in the microscope can be heated up to 500 K. If the connection of the cooling shroud inside the chamber would be dismounted, it could be heated higher. Upon cooling via the bath cryostat, the temperature plateaus around 110 K. If evacuated subsequently, the nitrogen freezes and the temperature equalizes around 90 K. The base temperature is then stable for 9-13 hours, slightly depending on the sample being counter-heated or not. If the bath cryostat runs empty, the temperature rises with 10-20 K/h. During this time, the bath cryostat is prone to blocking by frozen water vapor. An effective method to prevent this is to put the exhaust tube into a 10 l nitrogen Dewar, effectively creating a cryo trap.

The manipulator offers two heating methods. The first is the electron bombardment heating “E beam heating”. It can reach a manipulator temperature (T_M) of 630 K, what equals around 900 K sample temperature (T_S) without external cooling, and T_M = 960 K ($T_S \approx$ 1400 K) if the manipulator is simultaneously cooled via liquid nitrogen (see text below). The reachable temperature is limited due to the copper parts of the manipulator. The highest sample temperature, reached without exceeding the manipulator limit, is achieved by applying strong cooling and fast heating with high emission currents. The maximum temperature (around 1400 K) is only achievable with an acceleration voltage of -600 V. At this voltage, often visible arc discharges appear at the manipulator, especially, if it was not used at this condition for a longer period. This often originates from thin metal deposits created by sputtering. This is not necessarily a problem and often disappears upon repeated heating. Figure 8 shows the correlation between T_M and T_S, however, the achieved temperature strongly depends on heating parameters like acceleration voltage, emission current or the N_2 pressure upon counter cooling.

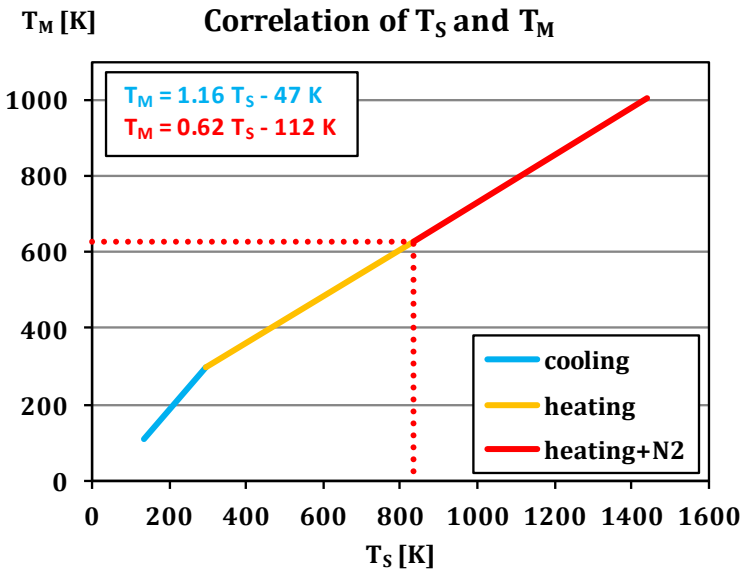

T_M [K]	T_S [K]
110	135
127	150
185	200
243	250
295	295
360	400
484	600
608	800
630	835
732	1000
856	1200
960	1368

Figure 8: Rough correlation between manipulator temperature (T_M) and sample temperature (T_S). Above T_M = 630 K, counter cooling must be applied. The formulars in the top left corner give an estimate of the correlation upon cooling (blue) and heating (red). However, the achieved temperature strongly depends on the applied heating or cooling parameters.

The second method, the direct heating of samples like a Si wafer, is rather unproblematic. The current flows directly through the sample and heats it resistively. This means the limit is the highest temperature that does not damage the sample. However, it is solely applicable to samples with a significantly higher resistance than manipulator and connector cables, to avoid heating these instead.

The manipulator is cooled by a copper cooling shroud that is submerged in liquid nitrogen. A steady stream of gaseous nitrogen from the gas line liquefies inside and flows into the cooling reservoir at the manipulator. The lowest achievable temperature is dependent on the pressure of the gas line. At 2.0 bar (the limit given in the manual) a minimum temperature around 140 K can be achieved. Higher pressures and therefore stronger cooling were possible, but this bears a significant risk. It is recommended to observe the chamber pressure during cooling and, if necessary, re-tighten the inner screws of the cooling shroud inside the manipulator.

2.4. SAMPLE PREPARATION

This chapter summarizes the preparation and evaluation methods used for the data contained in this thesis. In addition, information that is helpful for future utilization of the machine is presented. The parameters and values are often highly specific to the machine on hand, redundant, given in ranges, or contain information that is beyond the data discussed in this thesis. The intention on this is to allow for the identification of future changes on individual parts or to have comparative values for starting new projects. For precise and concise details on the data the interested reader is referred to the respective publications.

2.4.1. CLEANING PROCEDURES FOR SINGLE CRYSTALLINE SUBSTRATES

Most cleaning approaches in UHV involve sputtering and annealing. Sputtering is the acceleration of heavy ions by an applied potential to a target surface. The ions will collide with the surface and the impact depletes material from the surface. On the opposing side of the target, the material will be deposited, so sputtering can be applied for cleaning, or as deposition technique. If the target is the sample, it will be cleaned. If the target is the deposition material and the sample is positioned accordingly, material is ablated from the target and deposited on the sample. If a single crystal was sputter-cleaned, the surface is rough afterwards. To create a flat and crystalline surface, the substrate must be annealed high enough that the surface can rearrange. This is typically a few hundred degrees below the melting point. A good overview on preparation conditions for numerous substrates can be found elsewere.[108]

Cleaning of Au(111), Ag(111) and Cu(111)

All single crystals were cleaned via Ar^+ sputtering at a pressure of 5×10^{-5} mbar, 1 kV acceleration voltage, 10 mA emission current and a sputter current of 10-30 µA. For smoothing the surface, the Au(111), Ag(111), and Cu(111) single crystals were annealed for 10 min at a maximum sample temperature (T_S) of 800-900 K, which equals a manipulator temperature (T_M) of 630 K. This is also the highest temperature that should be applied without additional cooling. A description of the temperature readings is given in

Chapter 2.3.1. The heating was performed on the manipulator via electron bombardment, with a filament current (I_{Fil}) of 1.70 to 1.95 A, an acceleration voltage (U) of -450 V and an emission current (I_{Em}) of 30-50 mA.

Preparation of Rh(111)

The Rh(111) single crystal was sputtered as described above. For initial preparations, the surface was oxidized and reduced: first, for 10 min in O_2 at a pressure of 2 x 10^{-6} mbar at T_S = 800 K (T_M = 600 K); subsequently, for 10 min in H_2 at a pressure of 1 x 10^{-6} mbar at T_S = 500 K (T_M = 400 K). For all preparations, the Rh(111) was annealed afterwards for 10 min to T_S = 1300-1400 K (T_M = 960 K, crystal glows orange) with I_{Fil} at 1.80-2.00 A, with a U of -600 V, and I_{Em} of 80-100 mA. At this temperature, counter cooling of the manipulator is necessary with a N_2 pressure in the cooling shroud of 1.5-1.7 bar.

Resistive Heating

The machine also offers an option for resistive heating (or direct heating) for samples with low resistance (like Si wafers). For using this option, the cable at the manipulator must be switched and the correct sample holder must be used.

2.4.2. Deposition Techniques

Surface science knows various techniques for the preparation of thin films on surfaces. For vacuum applications, often vapor deposition is deployed due to high purity of deposited films with high precision and often relatively small effort. In the scope of this thesis, physical vapor deposition (PVD) and chemical vapor deposition (CVD) are most relevant; a complete overview can be found elsewhere.[109]

Deposition of Ionic Liquid (PVD)

The ionic liquid used in this thesis, $[C_1C_1Im][Tf_2N]$, was synthesized in ultraclean conditions as described in a previous publication.[110] The IL was deposited from an effusion

cell that was developed in our group especially for IL deposition. Deposition took place at a temperature (of the crucible with the IL) between 373 and 383 K, a filament current of 1.26 A, a voltage of 8.5 V and with water cooling.[57, 107] It was deposited on a substrate that was either cooled (in most cases below 170 K) or held at RT. During the deposition, a quartz crystal microbalance (QCM) was positioned in the evaporation cone of the evaporator. With the assumption that the IL sticks to the surface, this allows for a direct correlation of the signal on the QCM to the substrate coverage. The QCM was calibrated via coverage determination of layers on the surface, which yields a correlation between the QCM signal and the absolute deposition dose. An example for such a calibration is shown in Figure 9 (c.f. Chapter 3.1.2).

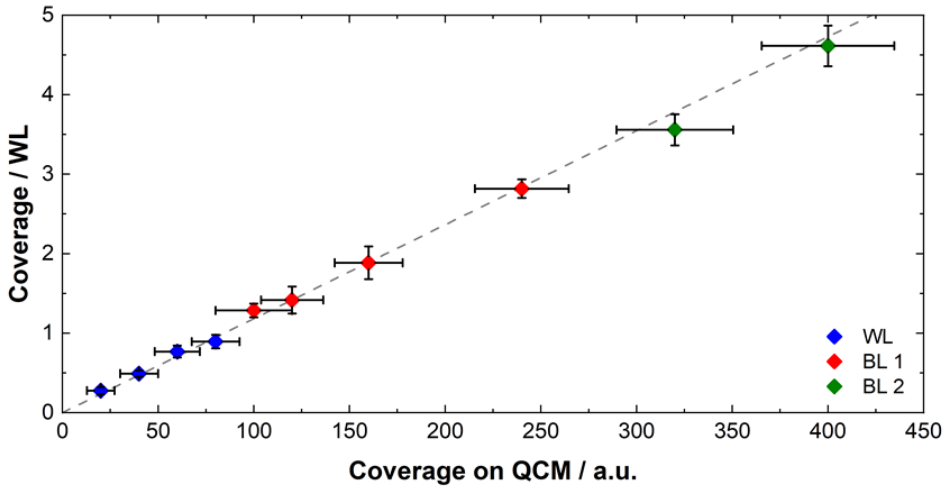

Figure 9: Calibration of the QCM. The microbalance is positioned close to the substrate during deposition. This allows for the correlation of the measured signal on the microbalance to the relative amount that was deposited. If the deposited substance grows in layers on the substrate, the QCM signal can be converted into a dose equivalent of one layer. Original image from [P2].

Deposition of Organic Molecules (PVD)

While the organic evaporator was not employed for the acquisition of the data for this thesis, it was used during the testing and establishment phase of the machine. As an example, 2H-tetraphenylporphyrin (2H-TPP), a commonly used porphyrin, was deposited on Au(111) for test purposes (Figure 10). The evaporation of porphyrins is achieved with 5-20 min at 640-700 K, a filament current of 1.4-1.7 A, a voltage of 2.7-3.0 V, and applied water cooling. Analog to the IL evaporation, the QCM can be used to determine surface coverage of the organic material during deposition.

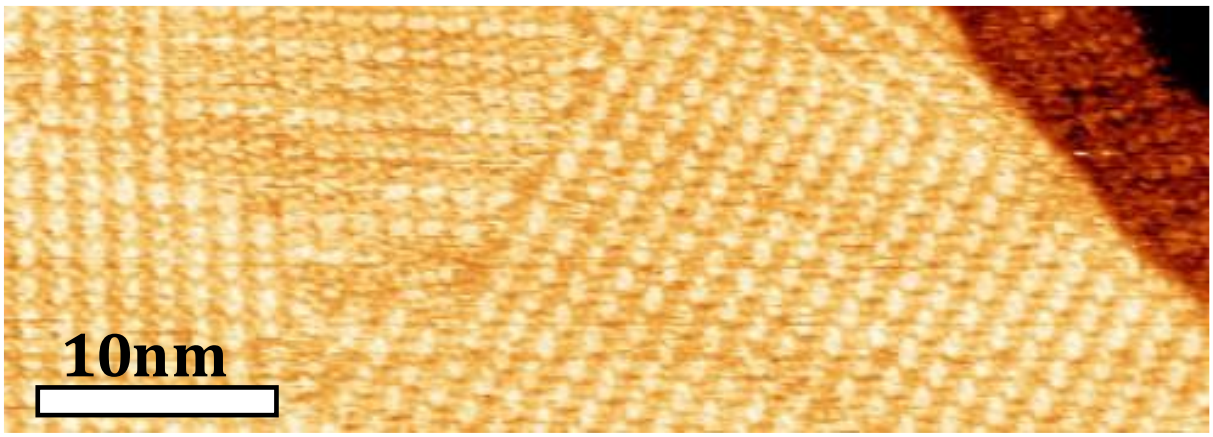

Figure 10: STM image of a densely packed layer of 2HTPP on Au(111). U=0.4 V, I=0.15 nA.

CVD of h-BN (CVD)

For Chapter 3.2 [P4], hexagonal boron nitride (h-BN) was grown on Rh(111) via chemical vapor deposition (CVD) from borazine directly after the cleaning process described above. Each time, prior to the deposition borazine was degassed in an UHV suitable glass vessel directly at the chamber via several freeze-pump-thaw cycles with liquid nitrogen until no visible bubbles developed upon thawing. Subsequently, h-BN was grown at a borazine pressure of 2 x 10^{-8} mbar and T_S at 1050 K (T_M = 750 K) for 30 min.[90] Thereafter, the dosage valve was closed and the surface was annealed for additional 5 min before cooling down to avoid adsorption from the gas phase.

Metal Deposition (PVD)

Metals can be deposited from the three-fold metal evaporator. It works by selectively heating the tip of a metal rod via electron bombardment. For Chapter 3.2 [P4], Pt was deposited on h-BN/Rh(111). Before Pt deposition, the manipulator was allowed to cool down and the background pressure was given time to normalize. After this, the crystal was shortly annealed to T_S = 800 K (T_M = 600 K) for 10 min to desorb CO that adsorbed on the surface during that time. Pt was deposited from an electron beam evaporator at a filament current of 2.0-2.3 A, a voltage of 1 kV, an emission current of 11 mA, and a flux of 8 nA. The dose was controlled via the deposition time (often 5 min). For the so-called wedge deposition (see Chapter 3.2) the manipulator was gradually moved into the deposition range of the evaporator by 0.1 mm every 3 s. This created a wedge-shaped increase in coverage from one side of the crystal to the other.

2.4.3. DATA ACQUISITION, CORRECTION AND EVALUATION

Raw images in microscopy and other image processing science branches rarely offer direct insights into all the information that is contained in an image. Sparingly applied processing that corrects existing artifacts, errors, or just facilitates the observation of features while not falsifying the information is often required. It strongly depends on the scientific statement that is meant to be extracted from the data and image corrections that are good for one measurement type can be problematic for another.

Typical Image Processing

In all cases, the images were treated and evaluated with WSxM software.[111] Typical image processing involved background subtraction and contrast/brightness adjustment. In some cases, single line scans with obvious errors (spikes) were removed or cut out. Videos often received a digital drift correction. Area determinations were carried out via the flooding function of the software, with threshold values extracted from a height histogram of the respective image. Fourier transformations were derived from cuts of single domains on single images.

Common Artifacts or Errors and how they are Approached

In SPM, common artifacts are thermal drift, piezo creep, curvature of the image, vibrations, or spontaneous changes in the tip geometry due to attachment or deattachment of molecules. This section gives an overview of some that have been relevant in past experiments.

Thermal drift, i.e., constant movement of the scan area, can be tackled by active drift correction during the measurement, which is approximated to the drift over a few images of the same region. A similar correction is also possible in the post processing. However, images taken with a drift on the sample will be distorted. They can either be stretched/compressed along the slow scan direction, warped in the fast scan direction, or both. Distortions like this can be corrected in the image processing. However, without known orientation points, measurements of molecular distances and angles are subject to a relevant error. Drift correction will become better with time. While recording videos

(e.g., for the investigation of molecular movement), it is ideal to use the drift correction to stabilize the sample position.

A tilted image plane is common and origins from slight tilt in the sample construction. A curved image plane is often caused by the piezo actuators. A tilt or a curvature in the image plane can be corrected by background subtraction. If working on single crystalline surfaces, single terraces can act as reference for a perfectly 2D plane.

Vibrations of mechanical or electronic origin arise as uniform stripes that stretch out over the entire image in the same direction for a constant vibration and in uniformly curved stripes for changing vibrations. Such vibrations can be corrected with a fourier filter, however periodic structures in the same magnitude will receive a strong bias. Ideally, the origin of a vibration is identified and suppressed instead. Often, it is more advisable to leave a vibrational artifact in the images instead of filtering it out.

The tip itself can also be subject to problems. Attachment or deattachment of molecules can create spikes in the image or cause a contact loss in AFM. Furthermore, edge effects broaden protruding features (this always occurs to some extent). With a very blunt tip, this leads to blurred images. A double tip, that is a tip with two most protruding parts instead of one, can create a duplication of all features on the image that are all displaced in the same direction. In all these cases, the tip can be reshaped by voltage pulses or (in case of soft substrates like gold) via intended crashes into the surface.

3. RESULTS

The solid liquid interface between ionic liquids and metal surfaces is of crucial importance for the optimization and tailoring of SCILL systems. This work focuses on the understanding of such interfaces on a molecular level and in real space. There have been several studies concerning this issue, but only very few microscopic studies in clean UHV environment were available. To our knowledge, these are the first UHV studies using AFM. With this work we aim to build a bridge from spectroscopic data to microscopic data under ambient conditions and to connect insights from highly controlled clean environments to more realistic conditions.

3.1. SOLID-LIQUID INTERFACE - $[C_1C_1Im][Tf_2N]$ ON Au(111)

The central topic of this thesis is to gather real space information on a molecular level on the growth, arrangement, and rearrangement of the IL-metal interface by applying scanning probe techniques. Since SPM was rarely applied before in this field, one of the first questions is which methods, specifically AFM or STM, are suited best for what types of measurements, and what are the commonalities and limitations. Furthermore, we aim to understand the general behavior of the IL-metal interface. To do this and to be able to compare results, we always investigated the same model system of 1,3-dimethylimidazolium bis[(trifluoromethyl)sulfonyl]imide ($[C_1C_1Im][Tf_2N]$) on Au(111) at multiple conditions and compared the results with corresponding spectroscopic data, mainly from XPS. We chose a very simple representative of a commonly used class of ionic liquids, imidazolium salts with $[Tf_2N]^-$ as anion. The cation, 1,3-dimethylimidazolium ($[C_1C_1Im]^+$) is an imidazolium ion without a long alkane chain, but two methyl groups. This creates a high symmetry, reducing many difficulties in the interpretation of molecular structures. The substrate was chosen for similar reasons. The Au(111) surface is not only inert, but it also features a unique herringbone reconstruction that enables the determination of crystal directions without atomic resolution and often even with a few layers of adsorbants.

3.1.1. MOLECULAR STRUCTURE OF THE WETTING LAYER [P1]

The aim of our first microscopic study on this system is to compare spectroscopic and microscopic data, elucidate differences and advantages between STM and AFM, as well as to gather fundamental information on the adsorption behavior of ILs on metallic surfaces.[112] Initially, we prepare an IL film by depositing a large amount of $[C_1C_1Im][Tf_2N]$ on Au(111), followed by thermal desorption of all IL that is not incorporated in the first layer. As a result, only a densely packed film remains. For ILs, this film is typically described as the wetting layer (WL) and often cations and anions are adsorbed besides each other, both in contact to the substrate. This arrangement is referred to as checkerboard configuration. Due to the usually stronger adsorption (and several other aspects that will be discussed in detail in the following chapters), the WL must be differentiated from layers on top, so called multilayers. These describe preparations with more ionic liquid present as required for the formation of the WL. By controlling the deposited amount one can create a partially covered surface that is then described in fractions of one complete WL. Such sub-WL films were analyzed with STM and AFM.

Primitive Order of the Wetting Layer

The first observation for the wetting layer is that it consists of large domains with a highly crystalline order. This order prevails even at room temperature (RT) and is observed with both STM and AFM (Figure 11 e,f). Remarkably, on large scaled images it is even possible to observe domains of IL with AFM up to 30-50 K above the melting point of bulk $[C_1C_1Im][Tf_2N]$ around RT. The highest temperature known to us at which a crystalline ordering was identified with STM was 240 K for $[C_2C_1Im][Tf_2N]$ on Au(111).[46]

The crystalline order of the wetting layer is investigated in more detail by probing the IL films at low temperatures. With less thermal motion it is possible to resolve single molecules, appearing as oval protrusions. Interestingly, although the IL is composed of two ions, we only find one type of protrusions in both AFM and STM independent on applied voltage bias in STM or polarization of the AFM tip or other measurement conditions. Considering previous publications on similar systems, we interpret these protrusions as $[Tf_2N]^-$ anions while the $[C_1C_1Im]^+$ cations (that are lying flat on the substrate as known from XPS)[48] are not resolved due to their smaller height compared to Tf_2N^- . Further-

more, we do not observe an amorphous phase that was found with STM for other ILs and substrates.[46, 49, 113] The reason for this difference is likely the high symmetry of the $C_1C_1Im^+$ cation.

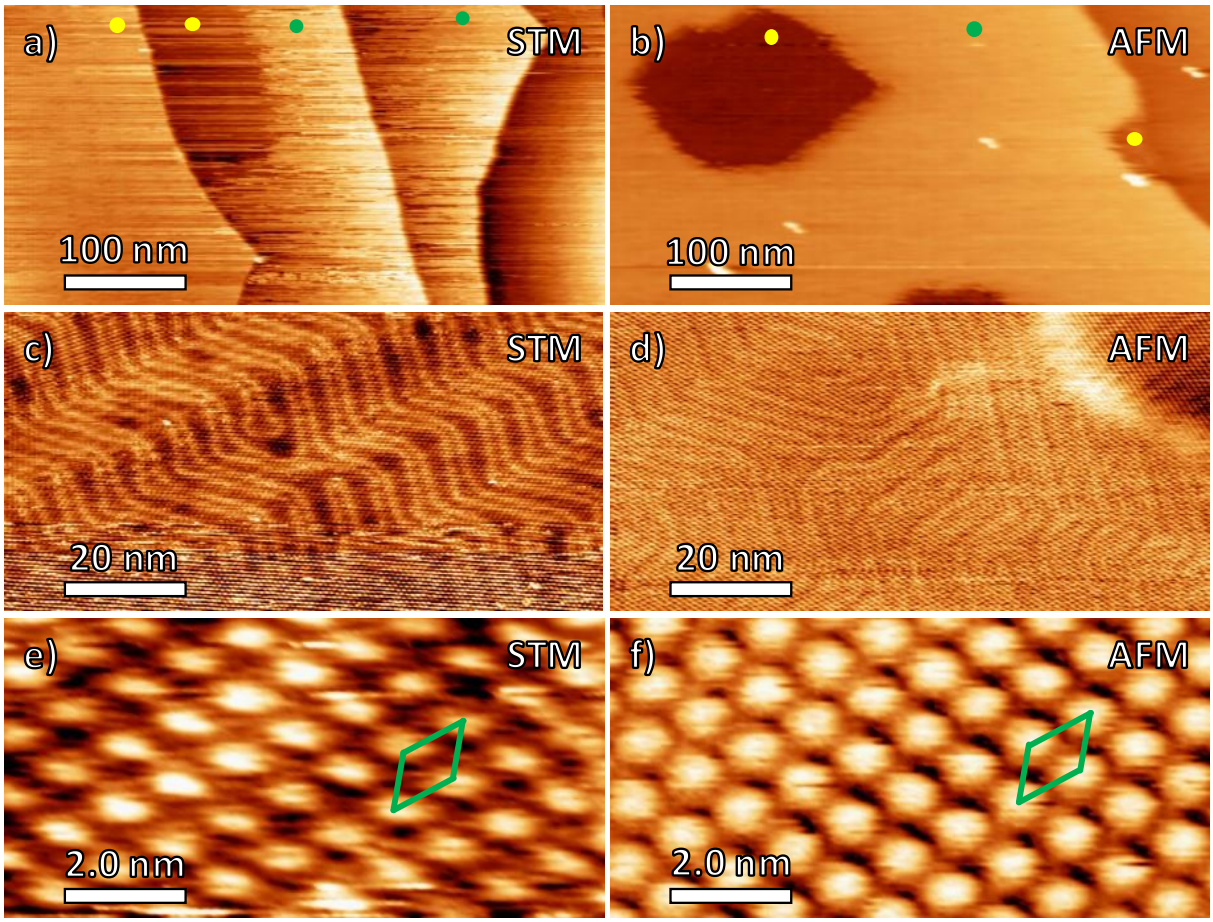

Figure 11: STM (left) and AFM (right) images of sub wetting layer coverages of [C_1C_1Im][Tf_2N] on Au(111), measured at 300 K. The IL (coverage in WL) is deposited between ~170 and 322 K and the sample was annealed prior to the imaging. Dots (a, b) mark free Au(111) (yellow) and wetting layer covered (green) surface. The primitive unit cell of the wetting layer is highlighted in green (e, f). Coverage, annealing temperature, and imaging parameter: a) 0.5 WL, 322 K, -1.2 V, 300 pA; b) 0.75 WL, 300 K, -300 Hz; c) 1.0 WL, 379 K, -1.2 V, 300 pA; d) 0.75 WL, 300 K, -400 Hz; e) 1.0 WL, 376 K, -1.2 V, 80 pA; f) 0.5 WL, 300 K, -200 Hz. Original image from [P1].

Orientational Superstructures at Low Temperature

While at RT only a hexagonal structure of the IL film is observable, one can find two different phases at low temperatures; see Figures 12 and 13. Fourier transformations of those phases reveal two different superstructures, a (2x1) superstructure for the S phase (striped) and a ($\sqrt{3}$x$\sqrt{3}$)R30° superstructure for the H phase (hexagonal); see Figure 14. The difference in those three (RT, H and S) originates from the orientations of the molecules. While the H phase is formed by three molecules per unit cell, which are

rotated towards each other by 60°, the S phase consists of double rows in an A-B pattern with only two molecules per unit cell. Thus, there are only two orientations. Both low temperature phases appear to be congruently arranged to the <110> axes of the Au(111) substrate, resulting in six orientations for the S and two for the H phase. Remarkably all three phases (RT, H, and S) exhibit nearly the same, primitive lattice for the molecular positions. We believe that at RT the molecules are mobile on the timescale of STM/AFM and rotate faster than we can resolve them. Therefore, roundish protrusions arise and an orientational superstructure is absent at RT.

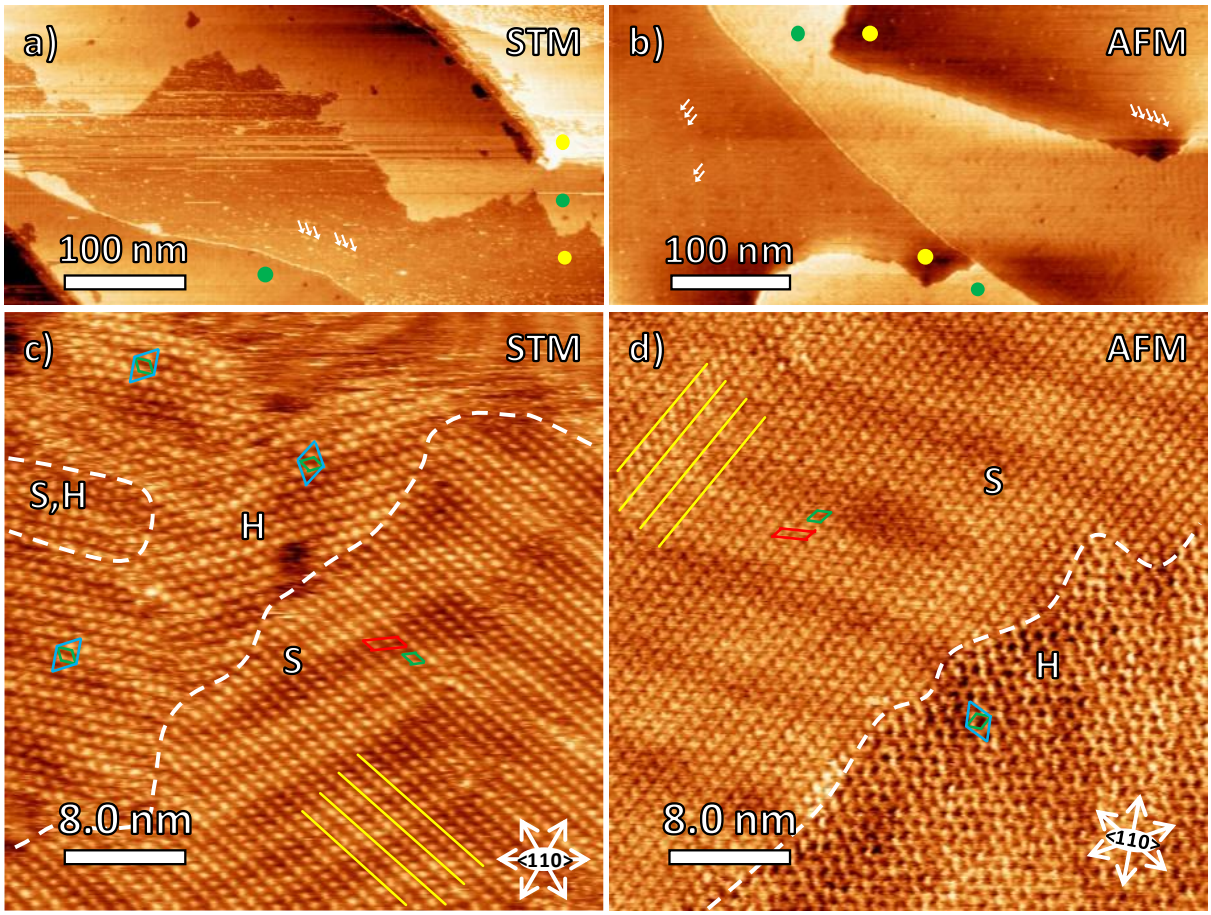

Figure 12: STM (left) and AFM (right) images of sub wetting layer coverages of [C_1C_1Im][Tf_2N] on Au(111), measured at 110 K, after annealing and cooling. Dots in the large-scale images (a, b) highlight free Au(111) surface (yellow) and extended wetting layer islands (green). White arrows mark some small IL islands at the elbows of the Au(111) 22x$\sqrt{3}$ reconstruction. The medium-scale images (c, d) show the two distinct phases of the wetting layer, marked with "S" for the "striped" and "H" for the "hexagonal" phase. Yellow lines highlight the stripe directions of the S phase; in addition, the unit cells of the orientational superstructures (H: blue, S: red) and the primitive unit cell (green) are shown. The <110> directions are shown in the bottom right corner. Coverage, annealing temperature, and imaging parameter: a) 0.5 WL, 295 K, -1.3 V, 300 pA; b) 0.5 WL, 381 K, -300 Hz; c) 1.0 WL, 370 K, -1.4 V, 35 pA; d) 0.5 WL, 381 K, -400 Hz. Original image from [P1].

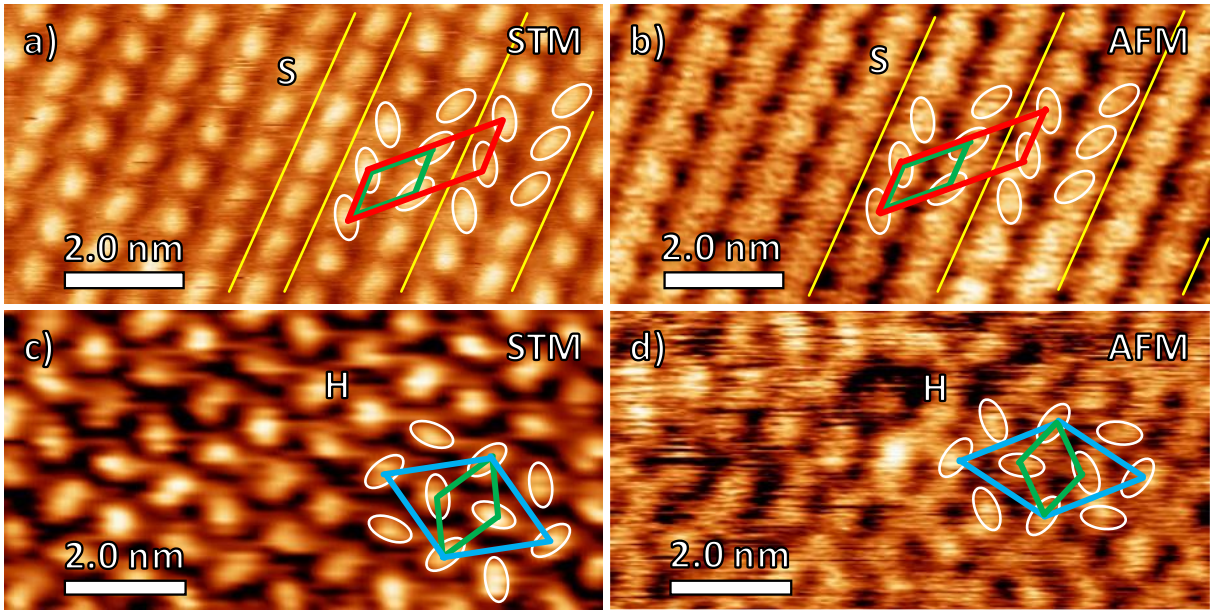

Figure 13: High-resolution STM (left) and AFM (right) images of sub wetting layer coverages of [C_1C_1Im][Tf_2N] on Au(111), measured at 110 K, after annealing and cooling. Yellow lines highlight the stripe directions of the S phase. White ovals mark the orientations of individual Tf_2N^- ions. The unit cells of orientational superstructures (H: blue, S: red) and primitive unit cell (green) are shown. Coverage, annealing temperature, and imaging parameter: a) 1.0 WL, 370 K, -1.4 V, 35 pA; b) 0.5 WL, 381 K, -400 Hz; c) 1.0 WL, 368 K, -1.4 V, 35 pA; d) 1.0 WL, 390 K, -450 Hz. Original image from [P1].

Comparison of STM and AFM

Comparing STM and AFM (Figures 11-13: STM left, AFM right), we find that STM is well suited for recording high resolution images of the molecular arrangement of the WL at low temperature. At RT however, AFM tends to be more stable than STM and allows for recording larger images with less noise. Furthermore, for coverages exceeding one WL, STM is not suitable at all for stable imaging anymore. AFM, however, still works fine. This is most likely caused by the ionic nature of IL. Stronger interactions with the tip inhibit STM strongly, while the imaging mechanism of AFM is barely influenced, even with multilayered films. AFM is therefore especially suitable for multilayered systems at elevated temperatures.

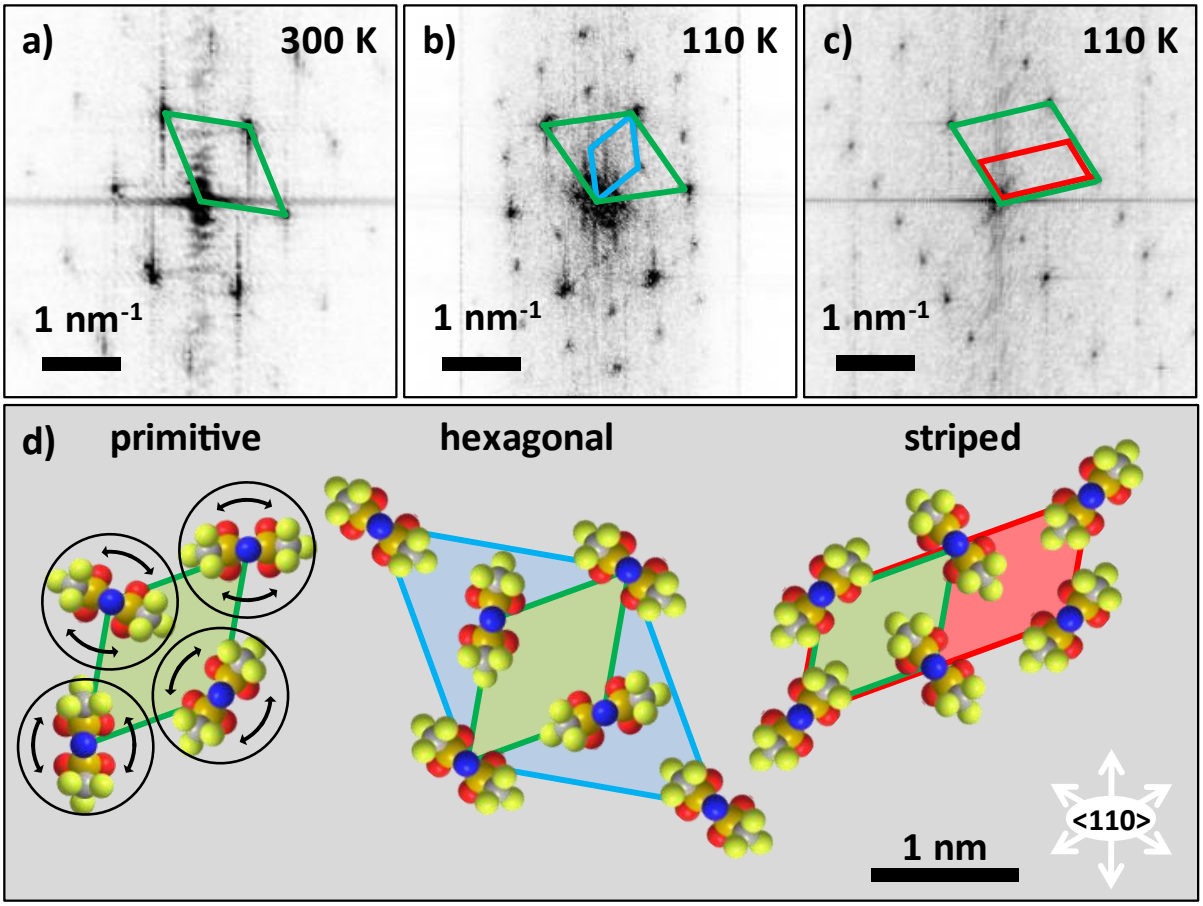

Figure 14: Fourier transformations of single-phase images (a-c) of the three phases observed with [C_1C_1Im][Tf_2N] on Au(111): the RT phase (a), the hexagonal phase (b) and the striped phase (c). The reciprocal unit cells of the orientational superstructures (blue and red) and the primitive unit cell (green) are shown in the FTs. Corresponding real space unit cells including scaled models of [Tf_2N]$^-$ ions and their orientation are depicted below (d). The positions and orientations of the cations could not be determined and are not shown. Source image parameter: a) 0.5 WL, 300 K, -200 Hz; b) 1.0 WL, 368 K, -1.4 V, 35 pA; c) 0.25 WL, 380 K, -2.0 V, 200 pA. Original image from [P1].

3.1.2. GROWTH AND ORDERING IN MULTILAYERED FILMS [P2]

After identifying the molecular structure of the wetting layer, the next step is to gain knowledge about the behavior of higher coverages and the dependency on time and temperature.[114] This chapter focuses on the growth and morphology of $[C_1C_1Im][Tf_2N]$ on Au(111) with respect to the deposited coverage up to several multiples of one WL. For this part, we only use AFM since we found it to be superior to STM in this coverage, temperature, and resolution regime.

Determination of Coverage

The central part of the measurements in this chapter is the precise determination of the surface coverage. By positioning a quartz crystal microbalance (QCM) next to the crystal during the deposition of the IL we are able to correlate the surface coverage, measured directly from AFM images, to the signal of the microbalance. With this setup, it is possible to give the exact dose of IL that is deposited on the crystal in units of one complete wetting layer. This deposition dose is referred to as one wetting layer equivalent (WLE).

Growth Characteristics of Wetting Layer and Multilayers

Films with coverages below 1 WLE show distinctly different adsorption and annealing behavior compared to multilayer coverages. While sub-WL coverages (Figure 15) lead to the formation of island like structures directly after the deposition at below 170 K, coverages exceeding this dose (Figure 16) tend to form a “snow-like” unordered structure. The annealing temperatures required to observe a comparable ripening of the islands is around 200 K in the sub-WL regime, and around 250 K for multilayer doses. Furthermore, and in contrast to sub-WL films, it is not possible to measure AFM images of the multilayer preparations above 280 K, since the images become increasingly distorted due to strong IL-tip interactions. These distortions prevail for multiple hours, even if the sample is cooled back again and measurements are then performed at low temperature. For sub-WL films however, it is possible to measure with AFM up to even 400 K without significant technical problems.

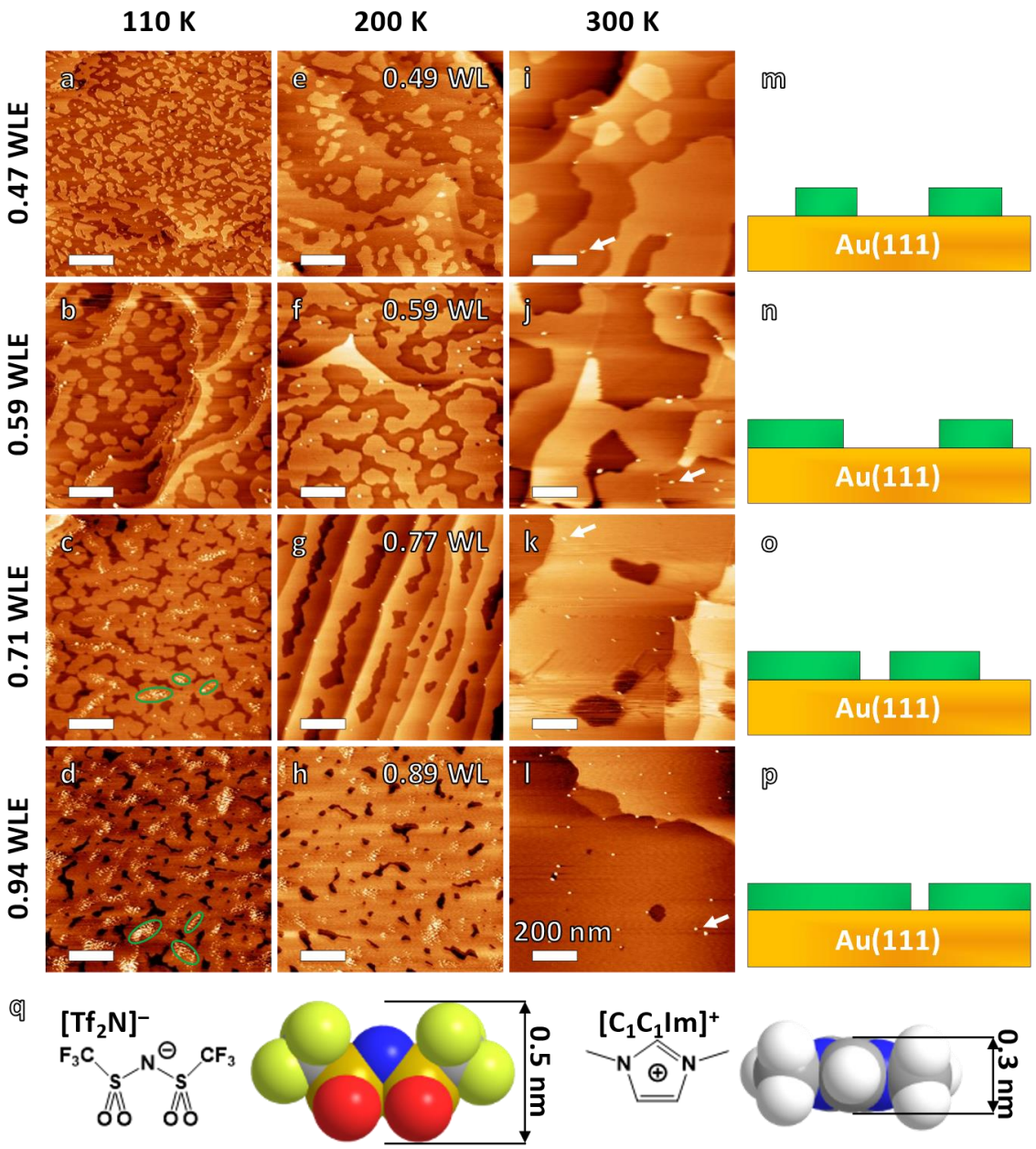

Figure 15: AFM images of different sub-WL coverages of [C_1C_1Im][Tf_2N], deposited on Au(111) at <170 K. The images were measured at 110 K (left), 200 K (middle), and 300 K (right) and the IL doses (in WLE) for one preparation series are denoted left to the images. The measured coverages (in WL) are denoted in the upper right corner of the 200 K images. On the right side (m-p), schematic representation of the prepared WL films, and at the bottom (q), a rough size estimation of the ions is shown. After the deposition of low coverages, small WL islands form that grow upon annealing. For higher coverages, small multilayer islands form on top of the WL islands (green ellipses) that decrease and eventually vanish upon annealing. Some protrusions, likely contaminations, are indicated by arrows. Coverage, annealing temperature, and imaging parameter: a) 0.47 WLE, 170 K, -350 Hz; b) 0.59 WLE, 170 K, -300 Hz; c) 0.71 WLE, 200 K, -300 Hz; d) 0.94 WLE, 168 K, -300 Hz; e) 0.47 WLE, 200 K, -300 Hz; f) 0.59 WLE, 200 K, -300 Hz; g) 0.71 WLE, 200 K, -300 Hz; h) 0.94 WLE, 200 K, -300 Hz; i) 0.47 WLE, 300 K, -200 Hz; j) 0.59 WLE, 300 K, -500 Hz; k) 0.71 WLE, 300 K, -300 Hz; l) 0.94 WLE, 300 K, -300 Hz. Original image from [P2].

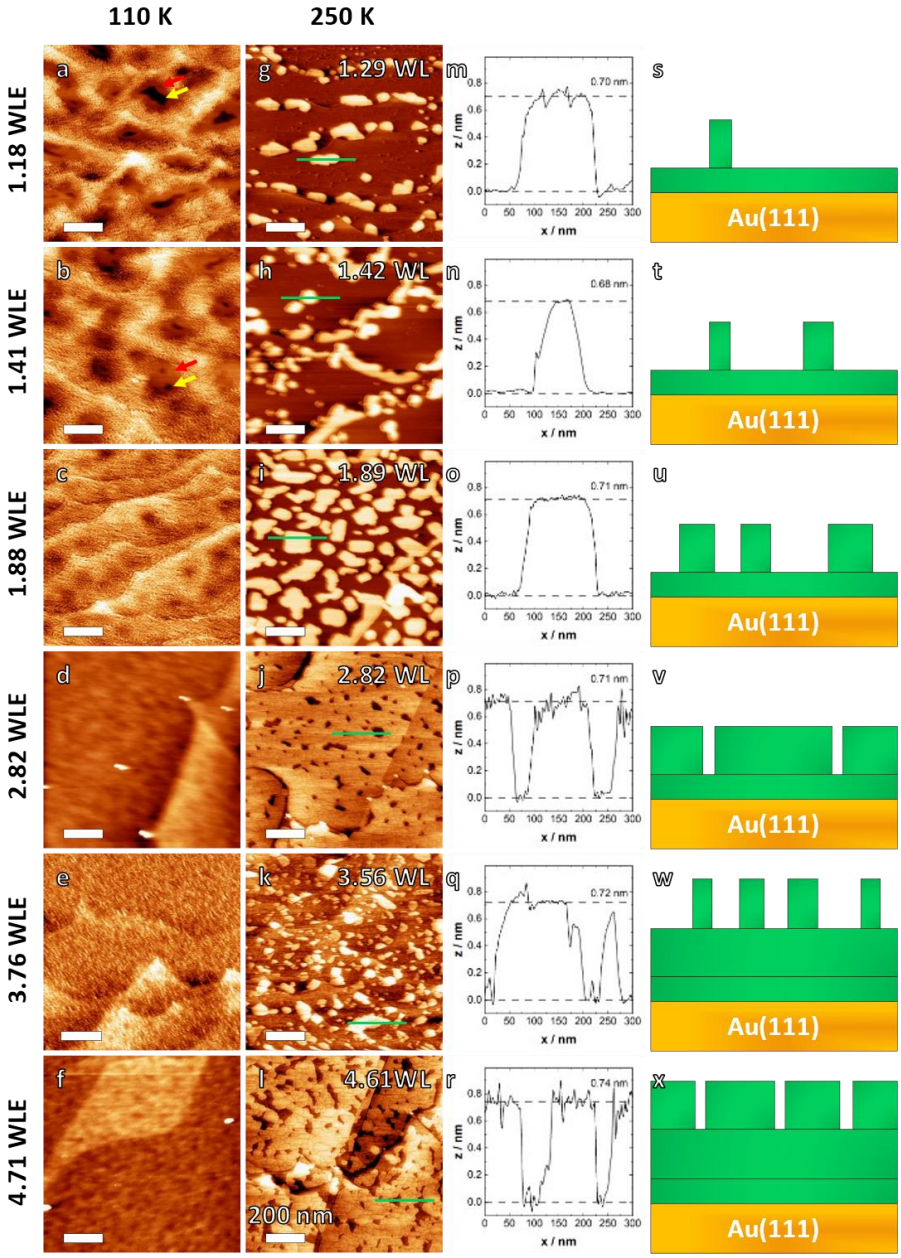

Figure 16: AFM images of multilayer coverages, of [C_1C_1Im][Tf_2N], deposited on Au(111) at <170 K. The images were measured at 110 K (left) and 250 K (right). The IL doses (in WLE) for one preparation series are denoted left to the images. At low temperatures, a WL forms with multilayer islands on top. For low coverages, some patches of free substrate (yellow arrow), surrounded by ~50 nm terraces (red arrow), are still present. At higher coverages, the surface has a smooth, snow-like appearance. Upon annealing at 250 K bilayer islands with heights of 0.71 nm form. A line profile and a schematic representation are shown on the right side. Coverage, annealing temperature, and imaging parameter: a) 1.18 WLE, 170 K, -400 Hz; b) 1.41 WLE, 163 K, -300 Hz; c) 1.88 WLE, 158 K, -300 Hz; d) 1.82 WLE, 153 K, -180 Hz; e) 3.76 WLE, 151 K, -200 Hz; f) 4.71 WLE, 189 K, -150 Hz; g) 1.18 WLE, 250 K, -300 Hz; h) 1.41 WLE, 250 K, -200 Hz; i) 1.88 WLE, 250 K, -150 Hz; j) 2.82 WLE, 250 K, -350 Hz; k) 3.76 WLE, 250 K, -180 Hz; l) 4.71 WLE, 250 K, -300 Hz. Original image from [P2].

Formation of Bilayers in the Multilayer Regime

After the deposition of different doses of IL, we determine the area that is covered with IL islands. To do this, the samples are first annealed until the island diameter is between 50-100 nm. At this size, the measured structures are significantly larger than the tip apex and the error by edge effects, originating from the tip shape, can be neglected. A plot of the covered area determined from the images against the deposited amount in WLE shows a sawtooth like shape that can be explained with a layer-by-layer growth; see Figure 17. Interestingly, for the layers that form on top of the WL, the slope in the graph is half of the slope in the WL regime. This can only be explained by layers that require twice the amount of IL per layer than the WL. We therefore conclude that the layers on top of the WL must be bilayers (BL). This interpretation matches a previous XPS study that describes layer-by-layer growth for this system; although it discusses growth as single layers, bilayer growth is in the scope of scatter.[56]

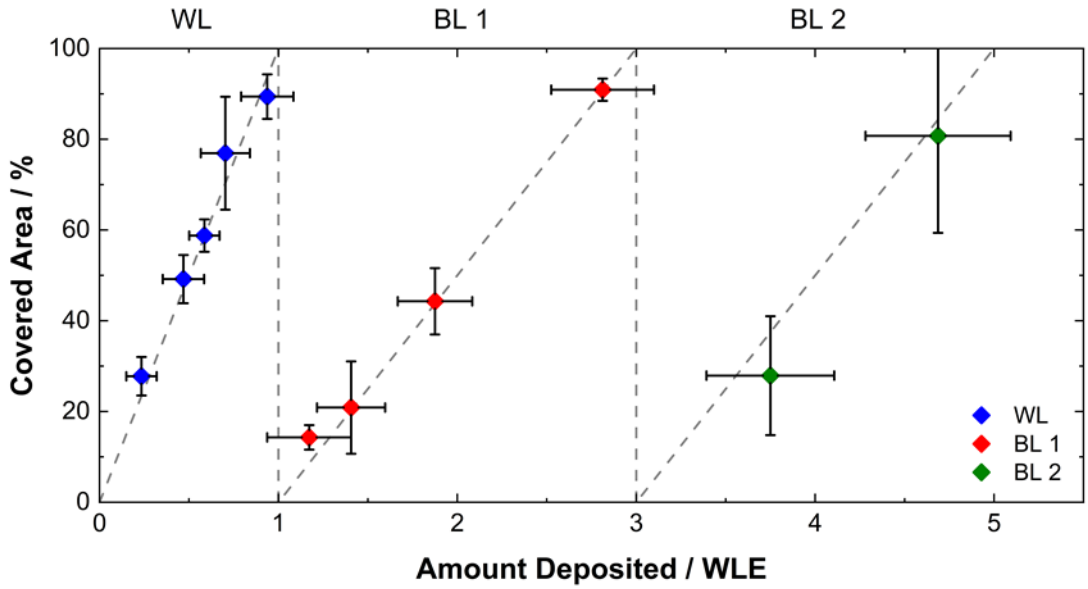

Figure 17: Average values of the covered area of the topmost layer of [C_1C_1Im][Tf_2N] on Au(111) as function of the IL dose (in WLE). Each layer covers more of the surface upon growing. After one layer is complete, the next layer starts to grow. The dashed line provides a guide to the eye. The layer growth shows a sawtooth-like behavior. The growth of the first layer (the WL, blue) follows a linear trend. The layers on top (BL1 in red, BL2 in green) also follow a linear trend but with half the slope of the WL. They require twice the coverage of the WL to complete. The layers on top of the WL therefore must be bilayers. Original image from [P2].

To further verify this interpretation, we measure thicknesses of layers by AFM line scans (see Figure 16 m-r). Unfortunately, we are unable to measure the height of the WL with AFM, because the force-distance relation of the metal surface and the tip is different to the force-distance relation between IL island and tip. This leads to apparent heights that vary with the resonance frequency shift Δf of the AFM measurement and (for very low Δf) can produce images with apparently negative heights of the WL islands. However, the measured heights of the BLs are constant in that regard. Fortunately, the height of the WL can be derived from XPS: The WL was reported to have a checkerboard arrangement with a height of 0.37 nm.[56] With AFM we find that the BLs have thicknesses of 0.71 ± 0.05 nm, which is twice the thickness of the WL, and also roughly the sum in height of both ions; a rough height estimation of the ions is shown in Figure 15 q.

Molecular Structure of Bilayers

High resolution images reveal that there are minor deviations from the bilayer structure. At the edges of bilayer islands, step-like terraces with lateral sizes of up to a few nm and a height of half a bilayer can exist. For both, the top of the bilayers and the step-like terraces, the molecular arrangement of the ions is closely related to the striped phase of the

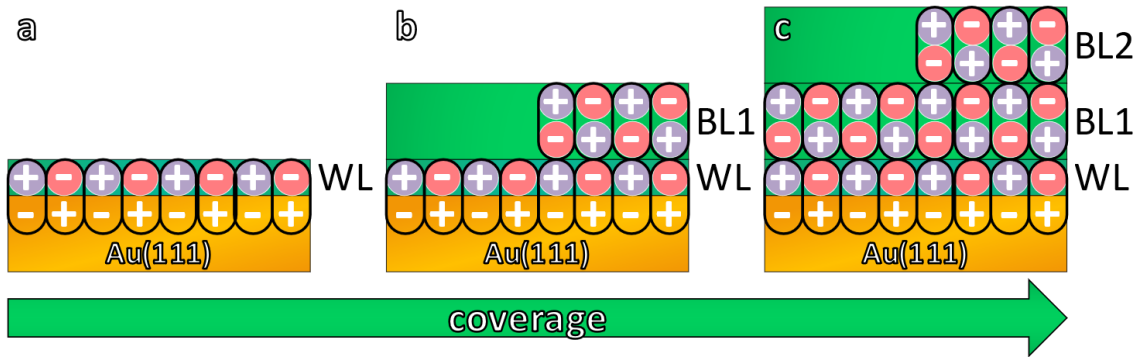

Figure 18: Schematic representation of the growth behavior of [C_1C_1Im][Tf_2N] on Au(111). The wetting layer forms with cations and anions adsorbed next to each other in a checkerboard fashion, creating opposing dipoles with image charges in the substrate. In the bilayers on top of the WL also dipoles of oppositely oriented ion pairs are formed, but now composed of two ions, respectively. The layers are stabilized laterally by attractive interactions of the oppositely oriented dipoles and the structure of the BLs is similar to the arrangement of the striped phase of the WL that is discussed in Chapter 3.1.1 [P1]. Original image from [P2].

WL (the striped phase is one of the two possible low temperature phases of the WL; see Figure 13). This observation leads to the conclusion that the overall arrangement in the WL and the BLs is similar. The trend to the formation of a single wetting layer in a checkerboard configuration and bilayers on top can be explained by the ionic nature of the IL. We assume that the ions create image charges in the metal substrate and form vertical dipoles with attractive lateral interactions. Ions on top also form oppositely oriented vertical dipoles while generally keeping the checkerboard arrangement of the WL. This arrangement is schematically drawn in Figure 18.

3.1.3. TIME DEPENDENT 3D-2D TRANSITION AT MULTILAYER COVERAGES [P3]

After taking a closer look on molecular structure and annealing behavior of the wetting layer and subsequent bilayers, that is, 2D growth behavior upon stepwise annealing, this chapter now focuses on 3D growth of $[C_1C_1Im][Tf_2N]$ on Au(111).[115] We find that 3D growth can occur for multilayer coverages under certain conditions. The 3D growth is related to the temperatures of the sample during and directly after deposition. This contrasts sub-WL coverages, which show no significant difference in the obtained film morphology between cold deposition (with the sample at 170 K and below) followed by heating to RT and warm deposition (sample at around RT), apart from larger islands due to more pronounced ripening at RT (Figure 19 a-c). Multilayer coverages, however, do feature a drastically different growth mode, when comparing films that are deposited at low temperature and around room temperature.

Formation of 3D Droplets upon Deposition of Multilayers at RT

Multilayer coverages that were deposited on a cold substrate (Figure 19 d,e) initially show a disordered snow-like film morphology. Upon slow annealing (several minutes to days, and/or at successively increased temperature) this morphology transforms to a 2D bilayered structure as discussed in Chapter 3.1.2 [P2] (Figure 19 g,h). In contrast, multilayer coverages that are deposited on a warm substrate result in the formation of large droplets with heights of 2-30 nm and diameters up to 500 nm. Between the droplets, large flat areas form that are free of any protrusions (Figure 19 f,i). Notably, this surrounding area is not the bare Au(111) substrate but the wetting layer, as deduced from molecularly resolved high resolution images (SI of [P3]). In contrast to slowly annealed low temperature preparations, the images after deposition at RT feature no individual bilayer islands, but instead terrace-like BL-rings around some of the droplets and occasionally small islands at step edges. Since the formation of the droplets occurred around RT, an investigation of these droplets at RT would be interesting. Unfortunately, we are unable to measure the droplets directly at RT due to the tip IL interaction already mentioned in Chapter 3.1.2 [P2]. Instead, it is necessary to cool the sample to study the droplets. This, however, leads to a compulsory cooling step what can have an influence on the droplets.

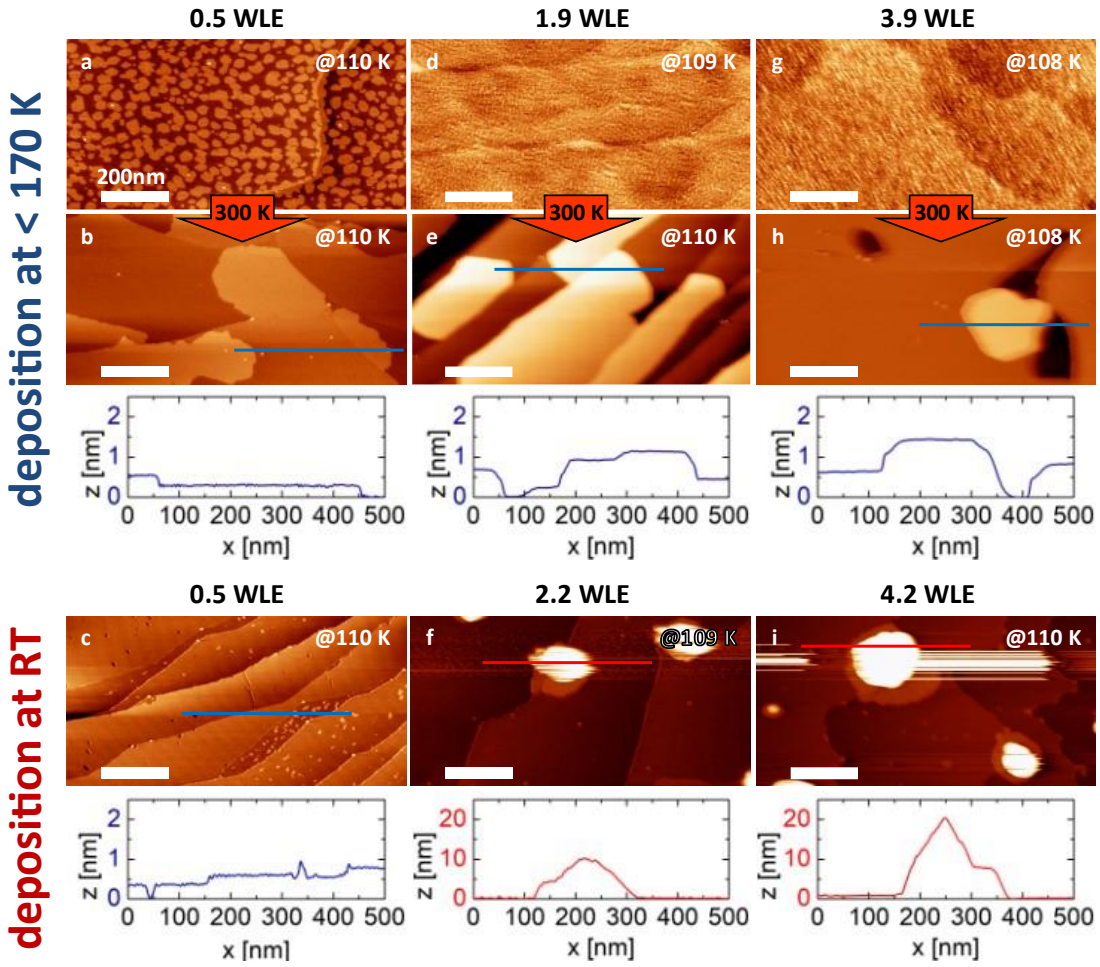

Figure 19: AFM images of [C_1C_1Im][Tf_2N] on Au(111), measured at 110 K. Different coverages (denoted above) were deposited at <170 K and slowly annealed to RT (two rows at the top). These are compared to samples that were directly deposited at RT (bottom). For sub-WL films, the resulting films are similar. For coverages in the multilayer regime, drastic differences in the observed morphologies are observed. Large droplets form on the surface with large flat areas in between. Line scans are shown below the respective images - note the different height scales. Coverage and imaging parameter: a) 0.5 WLE, -100 Hz; b) 0.5 WLE, -300 Hz; c) 0.5 WLE, -300 Hz; d) 1.9 WLE, -300 Hz; e) 1.9 WLE, -300 Hz; f) 2.2 WLE, -200 Hz; g) 3.9 WLE, -200 Hz; h) 3.9 WLE, -180 Hz; i) 4.2 WLE, -300 Hz. Original image from [P3].

The adsorption behavior is complicated, and the droplet formation is best described with the help of five series of experiments (Figure 20). They are referred to as (1),(2),(3),(4), and (5), and are discussed in [P3] in detail. First, we analyze, how the time at RT directly after the deposition influences the formation of droplets. The samples in the first two experiments were prepared similarly to the sample in Figure 19 i. However, while the sample in (1) was left at RT for 26 hours before the cooling step, in (2) the sample was transferred to the pre-cooled AFM stage as fast as possible. Interestingly, we do not observe a difference in the obtained structures. In both cases,

comparably large droplets form. After the AFM measurements, and therefore after the compulsory cooling step, the samples warm up to RT. In (1), the sample is cooled down again for a second measurement after several hours. Now the droplets have vanished, and only bilayer islands are present (Figure 20 b). In contrast, in (2), the sample was left at RT for only a few minutes. This, however, did not lead to a spreading of the droplets and similarly sized droplets are observed like before (c.f. Figure 20 c and d). We thus find that the IL droplets are stable at RT up to days, however if cooled once and heated to RT again, they start to spread out into bilayers within hours.

For experiment (3), a multilayer coverage is deposited on a cold substrate to create the initial snow-like structure described above (Figure 19 d,g). Interestingly, upon heating to 300 K for 2 min and immediate cooling to 110 K, the 3D droplets form as well. After subsequent annealing, the droplets vanish again and 2D bilayers emerge, just like in the first two experiments after the compulsory cooling step and enough time at RT. Fast annealing (a few minutes at RT) of a cold deposited IL film therefore also leads to droplet formation. On the other hand, slow annealing does not yield droplets, but a 2D bilayer structure forms as discussed in Chapter 3.1.2 [P2]. This behavior shows that the formation of the droplets does not solely occur during the deposition, but rather indicates that kinetic processes are involved in the formation of the droplets.

To narrow the temperature region, in which the formation of droplets and ripening to 2D bilayers occurs, we perform experiments (4) and (5). Instead of cooling below 170 K (deposition) or 110 K (AFM measurements), we perform both steps at 250 K. For (4), the IL is deposited on a warm substrate, followed by immediate cooling to 250 K. Like in (2), droplets are observed. After subsequent annealing at RT for roughly two hours, the droplets are completely transformed into 2D bilayers, like in experiment (1). This shows that the ripening process of the droplets to BL islands is also enabled by cooling to 250 K instead of 110 K. In Experiment (5), the sample was prepared and immediately measured at a substrate temperature of 250 K, each. Now, no droplets, but only 2D bilayers are present and upon annealing to RT no droplet formation is induced. Experiments (4) and (5) tell that the transitions between droplet formation on a warm substrate and the initialization of the droplet spreading on a cold substrate lie between 250 and 300 K. Notably, with 295[102] to 299[116] K also the bulk melting point of $[C_1C_1Im][Tf_2N]$ lies within this range.

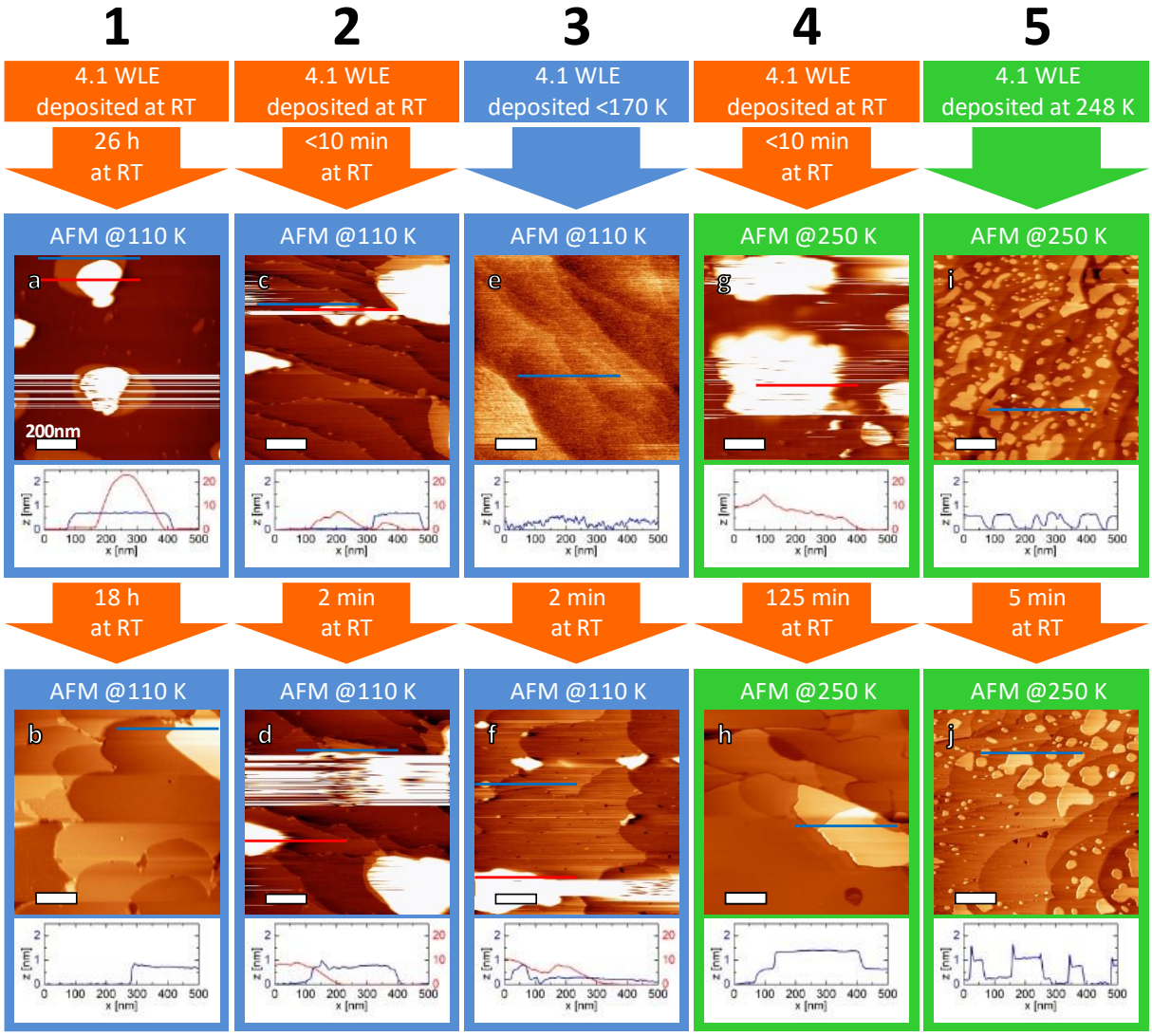

Figure 20: AFM images of 4.1 WLE of [C_1C_1Im][Tf_2N] on Au(111), measured at 110 K (blue frame) or 250 K (green frame). Line scans below the images show the heights of droplets or BL islands – note the different scales. Experiment 1: The droplets that have formed upon deposition at RT are stable for 26 h, but completely spread out into bilayers after being cooled once and left at RT overnight. Experiment 2: The droplets do not spread out to bilayers if the second time at RT is too short (2min). Experiment 3: Droplets can also form upon cold deposition (no bilayers have formed yet) and subsequent annealing to RT for 2 min. Experiment 4: Cooling the sample to 250 K for measurement (instead to 110 K) also enables the spreading of the droplets into bilayers (and already takes place at 250 K). Experiment 5: Deposition at 250 K (instead of RT) does not lead to the formation of droplets, but large bilayer islands are observed instead. Droplets formed neither after short annealing at RT. Imaging parameter: a-g) -300 Hz, h-j) -100 Hz. Original image from [P3].

These observations indicate that the droplets are a kinetically stabilized metastable phase. We explain their formation via processes with very different timescales. Initially upon deposition of [C_1C_1Im][Tf_2N], ion pairs on top of the wetting layer are very mobile

and can diffuse. Compared to isolated ion pairs, the 3D droplets have a higher and energetically favored coordination, therefore the ion pairs initially agglomerate to 3D droplets. This happens much faster than the nucleation and growth of 2D bilayers can occur and therefore is too fast for 2D bilayers to compete with the formation of 3D droplets.

Droplet Ripening and Bilayer Growth

As a next step, we follow the ripening behavior of the droplets (droplet spreading) *in situ* at constant temperature. Since we are unable to measure in the multilayer regime at RT, we perform the following experiments at 250 K instead. Figure 21 shows selected frames from an AFM video of a droplet of $[C_1C_1Im][Tf_2N]$ on Au(111) at 250 K. In this video, the droplets continuously decrease in height and bilayers start to grow around the droplets. After 1-2 hours at 250 K, the droplets transform into 3D structures that appear as stepped pyramid-like arrangements composed of several bilayers.

Eventually, after 3 hours only bilayers are left. However, when changing the position at the sample after the video was recorded, droplets are found again. These droplets equal the droplets in the initial stage of the video. Therefore, the ripening must be enhanced by the tip. The tip influence can be minimized if one avoids to scan the same area multiple times. Therefore, we perform series of measurements for three different coverages, with each image taken on a new area. Figure 22 shows an overview of the three series after comparably long annealing times at 250 K. Below each image a color-coded image highlights the individual layers, and a height profile provides a vertical scale. The images indicate that the initial droplet sizes increase with higher coverage. With increasing annealing time the droplets decrease in size and bilayers grow, apparently independent on coverage.

For more general insights, statistic data covering multiple images is collected. Figure 23 shows the average lateral and vertical dimensions as well as the distribution of IL between droplets and 2D layers, with respect to the annealing time at 250 K. We find that with higher coverage, mainly the heights of the droplets increase while the numbers and diameters of the droplets remain constant within the margins of error. The numbers and especially the heights of the droplets decrease upon annealing. However, the lateral dimensions remain rather constant. Knowing the number, as well as the lateral and

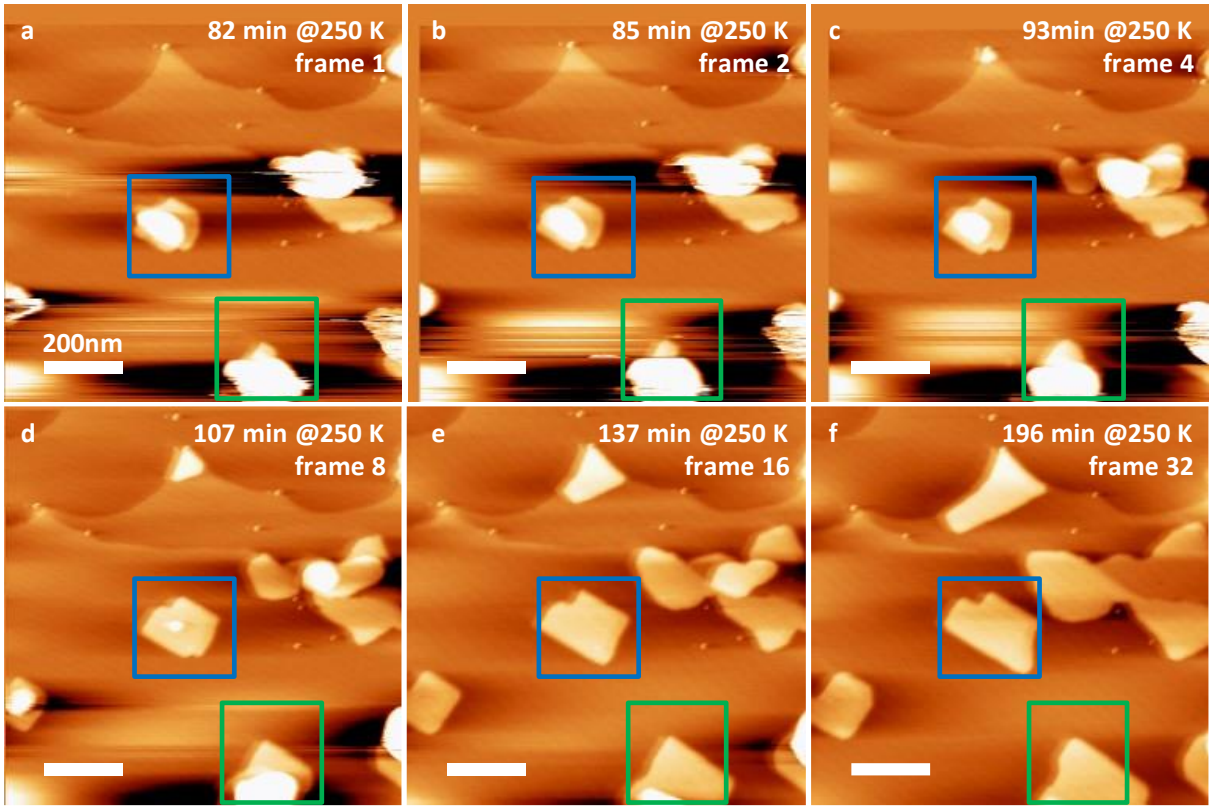

Figure 21: AFM images of 2.2 WLE of [C_1C_1Im][Tf_2N] on Au(111), deposited at RT, cooled to 110 K, and then measured at 250 K over a time span of 114 min. The images are part of an AFM video that is available in the SI of [P4]. The images show the evolution of individual droplets (blue and green frames), that are converted into 2D bilayer islands over time. Imaging parameter: -300 Hz. Original image from [P3].

vertical sizes of the droplets and assuming ellipsoid-like shapes of the droplets, the average volume of IL in droplets can be calculated. This droplet volume is compared to the volume of IL in bilayers and wetting layer, as well as the total amount deposited. We find that the conversion of the 3D droplets to the 2D islands takes several hours to days at 250 K, and hours at RT (Figure 23). We explain the slow conversion with a high activation barrier for the growth of the 2D structures, caused by slow deattachment or emission of ion pairs from a droplet. Possibly also a Schwoebel barrier,[117] that would limit the diffusion over island edges, is involved. The irreversible transformation into bilayered structures indicates that the 2D bilayers are thermodynamically favored over the 3D droplets. We explain this with the higher degree of order in the layers compared to the droplets, as a long-range crystalline order is present in WL and BLs, that is especially strong for the WL (above RT, c.f. 3.1.1 [P1]).

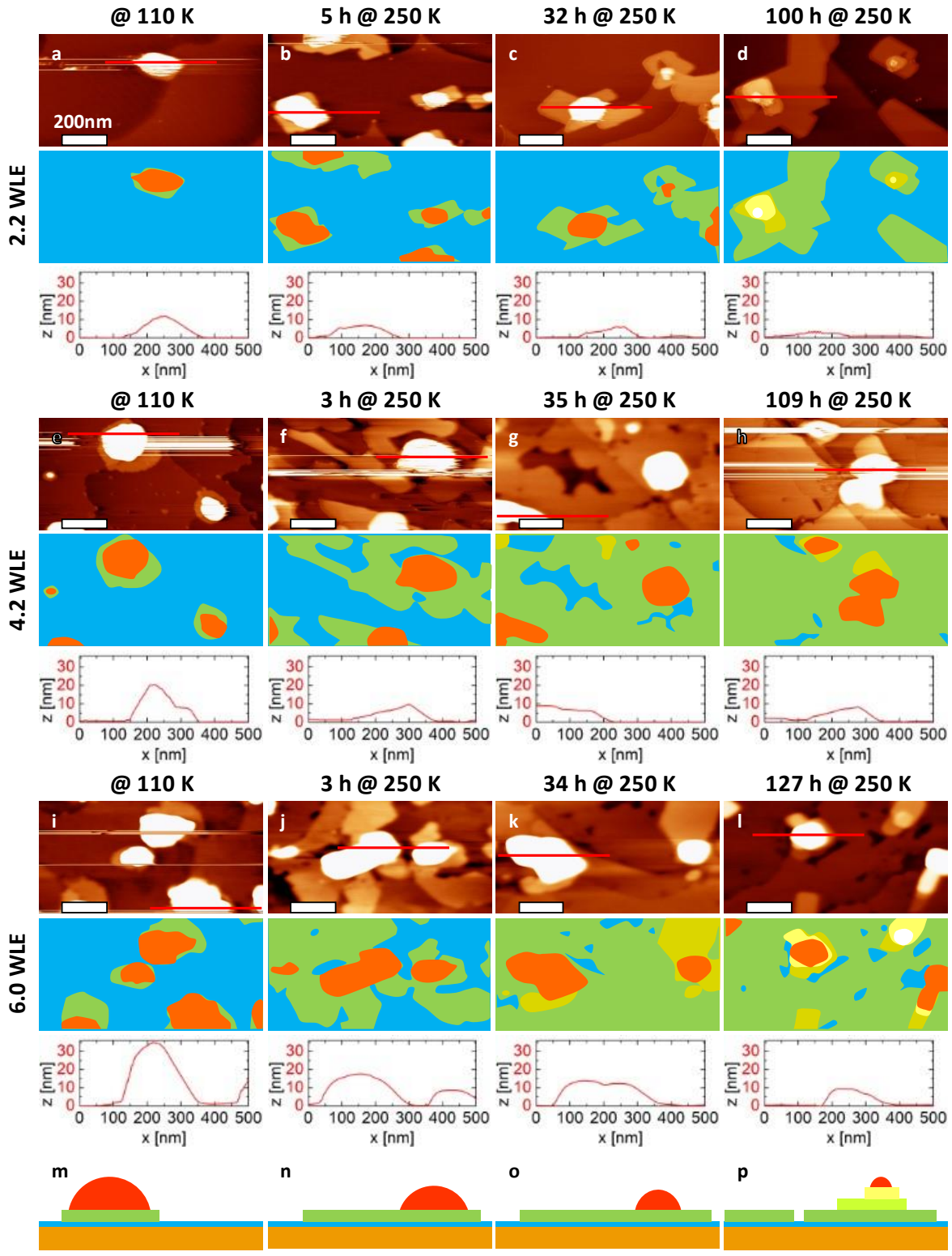

Figure 22: AFM images of 2.2, 4.2 and 6.0 WLE of [C_1C_1Im][Tf_2N] on Au(111), deposited at RT, cooled to 110 K and then measured at the temperature and time denoted above the images. Below the images, color-coded images highlight the different layers (blue for the WL - green, lime, and yellow for BLs – red for droplets) and line scans indicate the height of the droplets. With increasing time at 250 K the droplets decrease in size and transform into BLs. Imaging parameter: a) -300 Hz, b) -300 Hz, c) -300 Hz, d) -200 Hz, e) -300 Hz, f) -300 Hz, g) -20 Hz, h) -300 Hz, i) -20 Hz, j) -20 Hz, k) -20 Hz, l) -20 Hz. Original image from [P3].

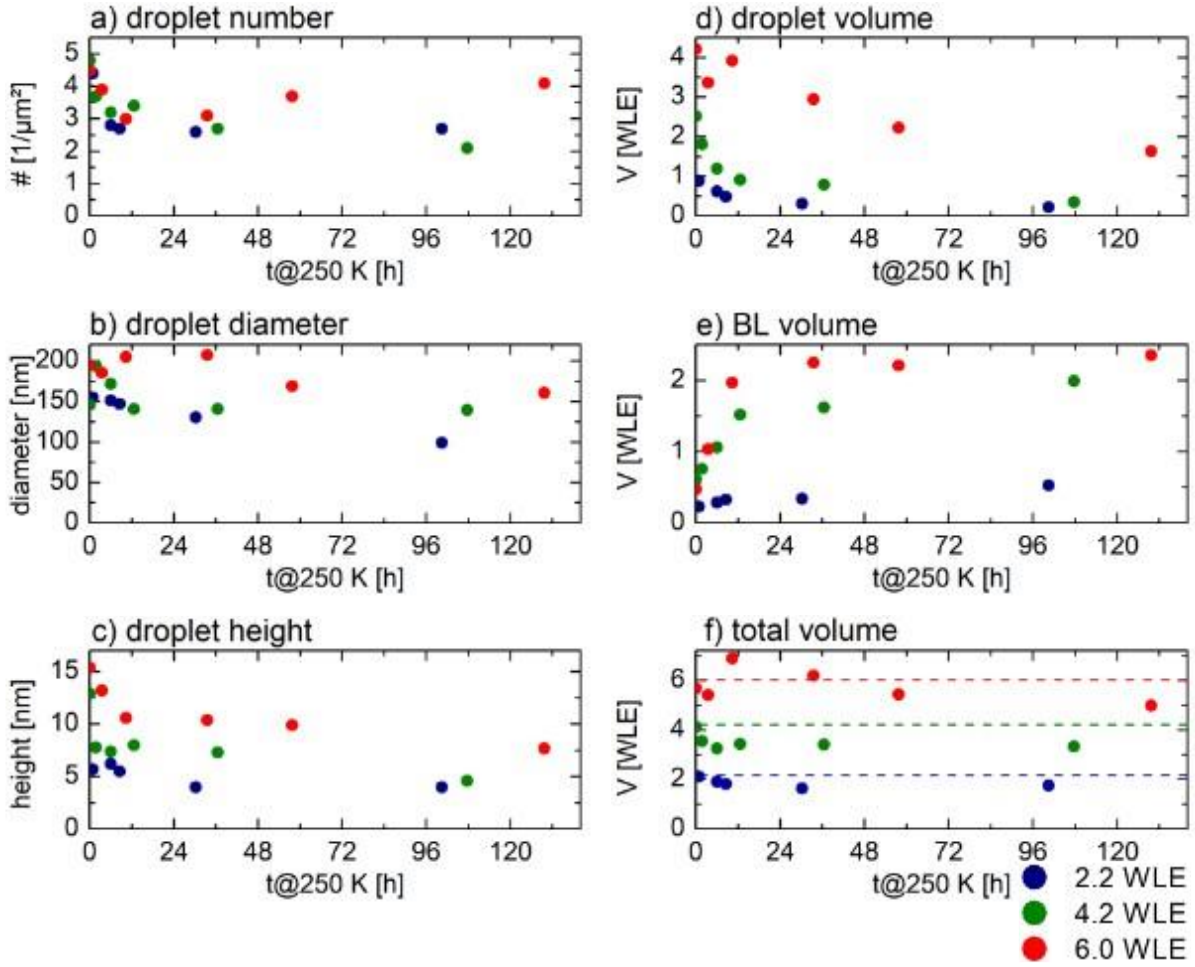

Figure 23: Statistical evaluation of AFM images with coverages of 2.2, 4.2 and 6.0 WLE of [C_1C_1Im][Tf_2N] on Au(111), deposited at RT, were analyzed. The numbers, diameters, heights, droplet volume, BL volume and total volume are plotted against the total annealing time at 250 K. Original image from [P3].

3.2. TOWARDS MORE COMPLEX SYSTEMS - Pt ON h-BN/Rh(111) [P4]

The success of surface science is highly related to the extremely well-defined conditions that are achievable when using typical techniques. While it is an enormous advantage for the understanding of fundamental principles to work on single crystals in ultrahigh vacuum, it remains a challenging task to relate those results to real conditions. This challenge is often referred to as pressure gap and material gap. For SCILL systems, the understanding of fundamental processes on a solid-IL interface, especially a metal-IL interface is of utmost importance. However, real catalysts are not single crystals but are often porous material or nanoparticles with kinks, steps, edges, and defects. To approach more realistic systems, we investigate a system of nanoparticles that are grown on a templating nanomesh. This system represents a more realistic model system for catalyst nanoparticles that is still accessible to surface science methods under highly controlled conditions.[118]

Deposition of Pt Nanoclusters on h-BN/Rh(111)

Hexagonal boron nitride (h-BN) forms a Moiré pattern if grown on single crystalline surfaces. In the case of h-BN on Rh(111) this leads to a porous hexagonal structure with sharply defined pores and so-called wires that are the elevated rim around the pores. The pores act as a template for the growth of metal nanoclusters. In this part, we investigate the growth and the thermal evolution of Pt clusters in such a h-BN nanomesh on Rh(111). Beforehand, the coverage of Pt is determined by depositing Pt on a bare Rh(111) surface and measuring the occupied area of the resulting two-dimensional Pt islands. With the assumption of epitaxial growth of Pt on Rh(111), one monolayer (ML) corresponds to a coverage of 1 Pt atom per Rh substrate atom. Note that this definition of ML is different to the other coverage definitions (WL, BL) used in this thesis in the context of ILs in Chapter 3.1 [P1-P3] (This is due to different conventions in the definitions in those fields). A special preparation technique for the deposition of Pt is used for some preparations, namely a coverage wedge, that is a coverage gradient over the whole single crystal. It allows for coverage dependent investigations at identical preparation conditions and enables the comparison of different coverages prepared in a single experiment. Also, this preparation technique reduces the production time for multiple

preparations to only one preparation, what is especially beneficial in synchrotron XPS experiments. More details on this topic are available in the dissertation of Fabian Düll.[119]

First, we compare Pt nanoclusters in the h-BN nanomesh of Rh(111) that were grown at different doses of Pt; see Figure 24. With the known size of the nanomesh, the coverages can be translated into an average number of atoms per unit cell of the Moiré pattern. For a very low Pt coverage of 0.005 ML, that is, 2.3 atoms per cluster, roughly 27% of the pores are filled with Pt clusters. Given this low number and the variation in the apparent size of the clusters, we think some of the clusters are just one single Pt atom. Interestingly, the clusters are remarkably stable, even at RT. We could not observe Pt atoms hopping to other pores in subsequently recorded images; however, it was possible to observe movement within the pores in STM videos. At a coverage of 0.09 ML (12 atoms per cluster) all pores of the h-BN nanomesh are filled with uniformly appearing clusters. Finally, also at a coverage of 0.42 ML (on average 55 atoms) all pores are filled, but now the clusters exhibit variations in the height to width ratio. The larger appearing clusters are susceptible to cluster-tip interactions that enable large clusters to leave the pores. The mobility of clusters can also be greatly increased by co-adsorption of CO, enabling also small clusters to leave the pores. Besides this, the clusters are stable for hours to days at RT.

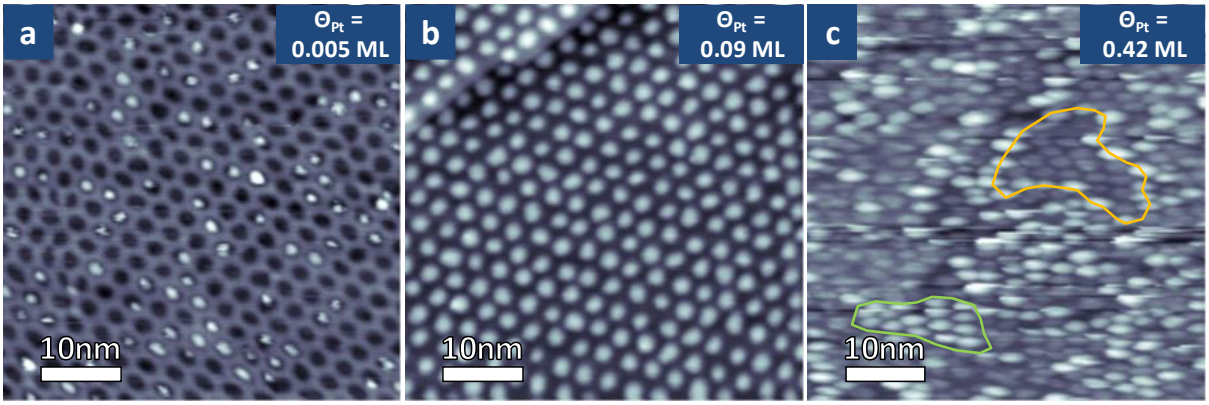

Figure 24: STM images of Pt clusters on h-BN/Rh(111) with Pt coverages of 0.005 ML (a), 0.09 ML (b) and 0.42 ML (c). At low coverage, the pores of the h-BN nanomesh are partially filled. Some of the "clusters" must be single Pt atoms in one pore. Around 0.09 ML (~12 atoms/pore) a remarkable uniform distribution of the clusters in the pores is found. At higher coverage, smaller (orange) and larger (green) clusters are found. Imaging parameter and Pt coverage Θ_{Pt}: a) -1.0 V, 1.0 nA, 0.005 ML; b) 1.5 V, 1.0 nA, 0.09 ML; c) 1.2 V, 1.0 nA, 0.42 ML. Original image from [P4].

Cluster Size Distribution in the Nanomesh

Figure 25 shows a statistical analysis of the relation between the Pt coverage (θ_{Pt}) and the fraction of filled pores in the low coverage regime up to 0.1 ML. In good agreement between STM and XPS experiments, we found a nearly linear relation. This contrasts a Poisson distribution, which is the distribution expected for a simple hit and stick mechanism with a single atom deposition technique. Thus, the experimental data suggest less but larger clusters. After the deposition, no movement of clusters between pores was observed. We conclude that a ripening process just after or within the deposition must be present and propose a hot precursor mechanism, where the Pt atoms can diffuse across multiple pores of the h-BN template before dissipating their kinetic energy. However, after deposition the energy barrier of the pores is too high to be overcome at RT.

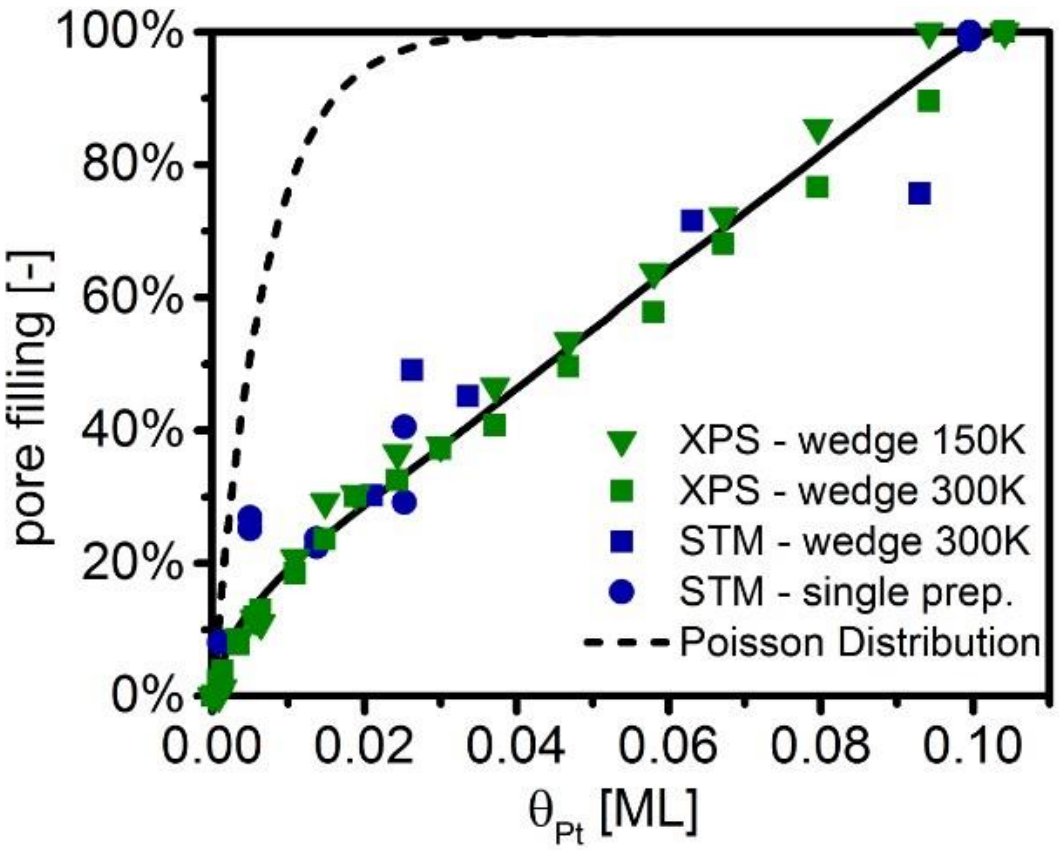

Figure 25: Fraction of filled h-BN pores as function of the Pt coverage (θ_{Pt}). The graph shows combined data from XPS and STM. The solid line serves as guide to the eye and the dashed line shows the expected curve for a Poisson distribution. Original image from [P4].

Ostwald Ripening of the Pt Clusters on h-BN/Rh(111)

As a next step, we investigate the thermal evolution of the nanoclusters during annealing (Figure 26). Up to 400 K, no significant changes in XP spectra or STM images are observed. However, after annealing to 500 K, a visible change of the size distribution of the clusters begins to emerge, and pores of the h-BN support start to become vacant again. In agreement with XPS, this trend is continued at higher temperature and eventually leads to few but very large Pt clusters on an otherwise free h-BN support. This behavior suggests an Ostwald type ripening process of the Pt clusters at elevated temperatures.

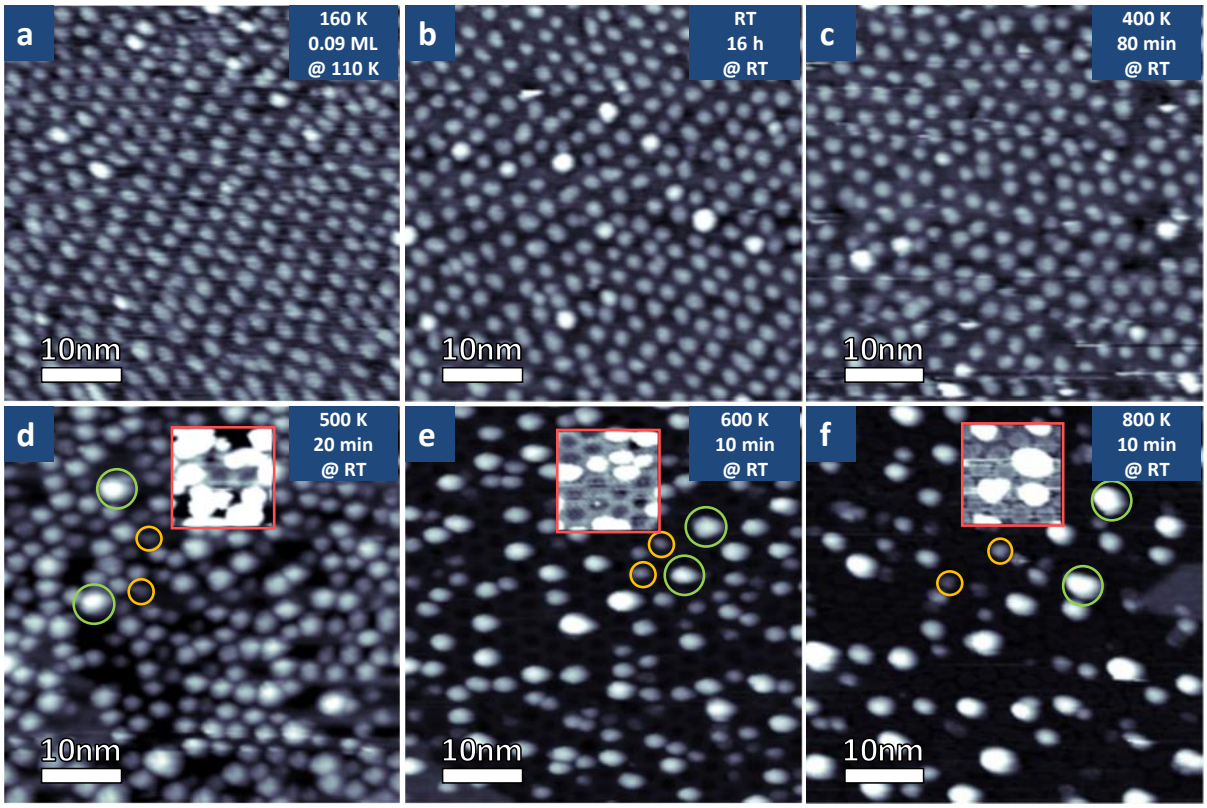

Figure 26: STM images of 0.09 ML Pt on h-BN/Rh(111), measured at RT. After deposition at 160 K, the sample was measured at 110 K (a) and then successively annealed up to 800 K. The Pt clusters are stable up to 400 K (a-c). Beginning at 500 K (d-f), some free pores can be observed again (red frame with enhanced contrast) and some cluster begin to appear smaller (orange) or larger (green). Imaging parameter and Pt coverage Θ_{Pt}: a) -1.5 V, 1.0 nA, 0.09 ML; b) 1.8 V, 1.0 nA, 0.09 ML; c) 1.8 V, 1.0 nA, 0.09 ML, d) -1.8 V, 1.0 nA, 0.09 ML; e) 1.0 V, 1.0 nA, 0.09 ML; f) 1.5 V, 1.0 nA, 0.09 ML. Original image from [P4].

4. SUMMARY

4.1. ENGLISH VERSION

This thesis addresses the structure and fundamental processes at the interface between ionic liquids (IL) and metals, as obtained by scanning tunneling microscopy (STM) and atomic force microscopy (AFM). Microscopic real space information is highly complementary to results from spectroscopic investigations, which were mostly used until today. The concerted picture, drawn from multiple systems that are investigated with multiple techniques, eventually enables to grasp the fundamentals of the underlying processes and set the stage for developing or enhancing novel catalytic concepts. The thesis at hand is a cumulative thesis based on four publications, [P1] to [P4]. Its central topic is the characterization of $[C_1C_1Im][Tf_2N]$ on Au(111) as a model system for the structure and growth of ionic liquid films at the ionic liquid to metal interface.

The first topic [P1] concerns the very first layer of ionic liquid directly on the metal substrate, the so-called wetting layer (WL). It is demonstrated that the WL has a long-range crystalline order that is stable up to 30-50 K above the bulk melting point of the IL. The ions are arranged in a primitive hexagonal lattice at RT. At 110 K, the orientation of the molecules becomes visible in STM and AFM, yielding two orientational superstructures of the lattice, while preserving the overall primitive hexagonal arrangement found at RT. The first is referred to as hexagonal phase with a $(\sqrt{3}x\sqrt{3})R30°$ superstructure, and the second is referred to as striped phase with a (2x1) superstructure. To the best of our knowledge, this study was the first AFM study of an ionic liquid on a metal substrate under UHV conditions, and also the first STM study at room temperature, which revealed molecular resolution. The comparison between the AFM and STM results revealed that for the system at hand, STM yields higher resolution for wetting layer coverages at low temperatures, while AFM proved to be superior at elevated temperatures and at coverages exceeding one WL.

The second topic [P2] concerns the multilayer regime of $[C_1C_1Im][Tf_2N]$ on Au(111), and addresses coverage dependence and thermal evolution. As first step, the coverage determination and calibration of the QCM is explained, followed by the description of growth characteristics of wetting layer and multilayer films. In comparison to sub-WL coverages, multilayer films initially form an unordered snow-like structure upon deposi-

tion around 170 K. Upon annealing, the formation of 2D bilayer (BL) islands is observed. Above 280 K, the investigation of multilayer films with AFM is impeded, likely by IL attaching to the tip. The relation between deposition dose and covered area in AFM images reveals the bilayered structure of the layers on top of the WL. This interpretation is supported by considering the height of the BLs. At the edges of BL islands, the arrangement in bilayers is not ultimately preferred. High-resolution images reveal small (few nm) terraces at the edges and provide an unimpeded view on the structure of both halves of the bilayer; both resemble the structure of the striped phase of the WL.

The third topic [P3] again addresses multilayers of $[C_1C_1Im][Tf_2N]$ on Au(111), but now with a focus on multilayer films deposited on a warm substrate (sample at around RT). It describes the formation and evolution of 3D droplets that can form upon deposition at RT or upon fast and short annealing to RT after deposition on a cold substrate (with the sample at 170 K and below). These droplets have heights between 2 and 30 nm and lateral dimensions up to 500 nm. The droplets are stable at RT up to days. Since AFM imaging of this IL is not possible above 280 K, cooling is applied to be able to characterize the droplets. However, cooling also initiates a transformation of the droplets into bilayers; at RT this will complete within hours and is irreversible. The temperature required for the droplets to form and for initializing the spreading into BLs is between 250 and 300 K. To obtain further insights, we follow the droplet spreading at a constant temperature of 250 K for different coverages. These results are statistically evaluated and discussed. The formation of the droplets occurs because the agglomeration into droplets is too fast for bilayer nuclei to compete. Cooling the sample allows sufficient nuclei to form, to initialize the transformation to a bilayered structure upon subsequent annealing. The arrangement of the IL in bilayers, however, is energetically favored over the agglomeration into droplets.

After the detailed characterization of one specific IL-metal interface in the first three topics, the final topic [P4] aims at a model system that resembles more realistic conditions. It addresses Pt clusters grown in the Moiré structure of hexagonal boron nitride (h-BN) on Rh(111). First, the preparation of the h-BN nanomesh and the deposition of Pt is described. The preparation via a coverage wedge allows for the investigation of a coverage range in one single sample preparation. Pt clusters grow in the pores of the h-BN nanomesh. This templating effect leads to a narrow size distribution of the nanoclusters.

We discuss a cluster size range that translates to 1-50 atoms per cluster. At very low coverages, some of the observed “clusters” are expected to be single Pt atoms entrapped in the pores of the nanomesh. At an average of 12 atoms per cluster (0.09 ML), we observe a strong uniformity of the clusters. Below ~0.1 ML, surprisingly we do not find a Poisson distribution, which would be expected for a hit and stick mechanism. To explain the observed tendency towards less and larger clusters, we propose a hot precursor mechanism upon deposition of Pt. The Pt clusters are stable up to 400 K, for several hours. Higher temperatures give rise to Ostwald ripening. While very low coverages (<0.2 ML) inhibit the ripening process, the presence of CO strongly enhances ripening of the clusters. Our work shows that Pt nanoclusters can be prepared in high uniformity. This system thus can possibly be applied as model system for forthcoming investigations about catalyst nanoparticles on inert substrates; it particularly opens a route towards studying the influence of IL adsorption onto well-defined metal clusters in the framework of the SCILL concept with surface science techniques.

4.2. GERMAN VERSION (DEUTSCHE ZUSAMMENFASSUNG)

Diese Arbeit befasst sich mit der Struktur und den grundlegenden Prozessen an der Grenzfläche zwischen ionischen Flüssigkeiten (IL) und Metallen und den Erkenntnissen, die darüber mittels Rastertunnelmikroskopie (STM) und Rasterkraftmikroskopie (AFM) gewonnen werden können. Mikroskopische Realrauminformationen sind in hohem Maße komplementär zu Ergebnissen aus spektroskopischen Untersuchungen, die bisher oft genutzt wurden. Ein konzertiertes Bild, welches aus mehreren Systemen mittels vielerlei Techniken gezeichnet wird, kann es schließlich ermöglichen, die Grundlagen der zugrunde liegenden Prozesse zu verstehen und die Voraussetzungen für die Entwicklung oder Verbesserung neuer katalytischer Konzepte zu schaffen. Die vorliegende Arbeit ist eine kumulative Dissertation basierend auf vier Publikationen, [P1] bis [P4]. Das zentrale Thema ist die Charakterisierung von $[C_1C_1Im][Tf_2N]$ auf Au(111), als Modellsystem für die Struktur und das Wachstum von ionischen Flüssigkeitsfilmen an der Grenzfläche ionischer Flüssigkeiten zu Metall.

Das erste Thema [P1] betrifft die allererste Schicht ionischer Flüssigkeit direkt auf dem Metallsubstrat, die sogenannte „wetting layer“ (WL, deutsch: Benetzungsschicht). Es wird gezeigt, dass die WL eine weitreichende kristalline Ordnung hat, die bis zu 30-50 K über dem Schmelzpunkt der flüssigen Phase der IL stabil ist. Die Ionen sind bei Raumtemperatur (RT) in einem primitiven hexagonalen Gitter angeordnet. Bei 110 K wird die Orientierung der Moleküle in STM und AFM sichtbar. Es existieren zwei Orientierungsüberstrukturen des Gitters, während die bei RT gefundene primitive hexagonale Anordnung erhalten bleibt. Die erste, mit einer $(\sqrt{3}x\sqrt{3})R30°$-Überstruktur, wird als hexagonale Phase bezeichnet, und die zweite, mit einer (2x1)-Überstruktur, wird als gestreifte Phase bezeichnet. Nach unserem besten Wissen war diese Studie die erste AFM-Untersuchung einer ionischen Flüssigkeit auf einem Metallsubstrat unter UHV-Bedingungen und auch die erste STM-Studie bei Raumtemperatur, die eine molekulare Auflösung ergab. Der Vergleich zwischen den AFM- und STM-Ergebnissen zeigte, dass STM für das vorliegende System eine höhere Auflösung für WL-Bedeckungen bei niedrigen Temperaturen liefert, während sich AFM bei erhöhten Temperaturen und größeren Bedeckungen als einer WL als überlegen erwies.

Das zweite Thema [P2] betrifft Mehrschichtsysteme von $[C_1C_1Im][Tf_2N]$ auf Au(111) und befasst sich mit deren Bedeckungsabhängigkeit und thermischer Entwicklung. Im ersten

Schritt wird die Bedeckungsbestimmung und Kalibrierung des Schwingquarzes (QCM) erläutert, gefolgt von der Beschreibung des Wachstumsverhaltens von WL- und Mehrschichtfilmen. Im Vergleich zu Sub-WL-Bedeckungen bilden Filme im Mehrschichtregime bei der Abscheidung um 170 K zunächst eine ungeordnete schneeähnliche Struktur. Beim Tempern wird die Bildung von 2D-Bilageninseln, (oder Doppelschichten, BL) beobachtet. Oberhalb von 280 K ist die Untersuchung von Mehrschichtfilmen mit AFM nicht möglich, wahrscheinlich durch die Anlagerung von IL an der Spitze. Die Beziehung zwischen Aufdampfdosis und bedeckter Fläche in AFM-Bildern ergibt für Schichten auf der WL eine zweischichtige Struktur. Diese Interpretation wird durch Höhenprofile der BLs unterstützt. An den Rändern von BL-Inseln ist die Anordnung in Doppelschichten nur eingeschränkt vorhanden. Hochauflösende Bilder zeigen kleine (wenige nm) Terrassen an den Rändern und geben einen ungehinderten Blick auf die Struktur beider Hälften der Doppelschicht; beide ähneln der Struktur der gestreiften Phase der WL.

Das dritte Thema [P3] befasst sich erneut mit Mehrschichtsystemen von $[C_1C_1Im][Tf_2N]$ auf Au(111), jetzt jedoch mit Fokus auf Filmen, die auf einem warmen Substrat (etwa bei RT) abgeschieden werden. Es befasst sich mit der Bildung und Entwicklung von 3D-Tröpfchen, die sich während der Abscheidung bei RT, oder nach der Abscheidung auf einem kalten Substrat (bei 170 K oder darunter) gefolgt von schnellem und kurzem Tempern auf RT, bilden können. Diese Tröpfchen haben Höhen zwischen 2 und 30 nm und laterale Abmessungen bis zu 500 nm. Die Tröpfchen sind bei RT mehrere Tage stabil. Da AFM Messungen oberhalb von 280 K nicht möglich sind, muss gekühlt werden, um die Tröpfchen trotzdem charakterisieren zu können. Durch Abkühlen wird jedoch auch eine Umwandlung der Tröpfchen in Doppelschichten eingeleitet; bei RT geschieht dies innerhalb von Stunden und ist irreversibel. Die zur Bildung der Tröpfchen und zur Initialisierung der Ausbreitung in BLs erforderliche Temperatur liegt zwischen 250 und 300 K. Um weitere Erkenntnisse zu gewinnen, verfolgen wir die Tropfenausbreitung bei einer konstanten Temperatur von 250 K für verschiedene Bedeckungen. Diese Ergebnisse werden statistisch ausgewertet und diskutiert. Die Tröpfchen bilden sich, da die Agglomeration zu Tröpfchen zu schnell ist, als dass Doppelschichtkeime konkurrieren könnten. Das Abkühlen der Probe ermöglicht die Bildung ausreichend vieler oder großer Keime, um beim anschließenden Tempern die Umwandlung in eine Doppelschichtstruktur zu initialisieren. Die Anordnung der IL in Doppelschichten ist gegenüber der Agglomeration zu Tröpfchen energetisch begünstigt.

Nach der detaillierten Charakterisierung einer spezifischen IL-Metall-Grenzfläche in den ersten drei Themen, zielt das letzte Thema [P4] auf ein Modellsystem ab, das realistischeren Bedingungen ähnelt. Es befasst sich mit Pt-Clustern, die in der Moiré-Struktur von hexagonalem Bornitrid (h-BN) auf Rh(111) gewachsen sind. Zunächst wird die Herstellung des h-BN-Nanomeshs und die Abscheidung von Pt beschrieben. Die Präparation über einer keilförmigen Bedeckungsverteilung ermöglicht die Untersuchung eines ganzen Bereichs verschiedener Bedeckungen in einer einzigen Probenpräparation. Pt-Cluster können innerhalb der Poren des h-BN-Nanomeshs wachsen. Dieser Templateffekt führt zu einer engen Größenverteilung der Nanocluster. Wir diskutieren einen Clustergrößenbereich von 1-50 Atomen pro Cluster. Wir vermuten, dass einige der bei sehr geringen Bedeckungen beobachteten „Cluster“ einzelne Pt-Atome sind, die in den Poren des Nanomeshs eingeschlossen sind. Bei durchschnittlich 12 Atomen pro Cluster (0,09 ML) beobachten wir sehr einheitliche Cluster. Unterhalb von ~0,1 ML finden wir überraschenderweise keine Poisson-Verteilung. Diese wäre für einen Hit-and-Stick-Mechanismus zu erwarten. Um die beobachtete Tendenz zu sowohl weniger als auch größeren Clustern zu erklären, schlagen wir einen „hot-precursor”-Mechanismus bei der Abscheidung von Pt vor. Die Pt-Cluster sind bis 400 K über mehrere Stunden stabil. Höhere Temperaturen führen zu Ostwald-Reifung. Während sehr niedrige Abdeckungen (<0,2 ML) den Reifungsprozess hemmen, fördert die Anwesenheit von CO die Reifung der Cluster stark. Insgesamt zeigt diese Arbeit, dass sehr einheitliche Pt-Nanocluster hergestellt werden können. Dieses System kann möglicherweise als Modellsystem für zukünftige Untersuchungen zu Katalysator-Nanopartikeln auf inerten Substraten verwendet werden. Im Rahmen des SCILL-Konzepts eröffnet dies einen Weg für die Untersuchung der Einflüsse von IL-Adsorption auf wohldefinierte Metallcluster mittels Techniken der Oberflächenwissenschaften.

5. REFERENCES

1. Wasserscheid, P.; Welton, T., *Ionic Liquids in Synthesis*. Wiley: 2008.
2. Weingärtner, H., Understanding ionic liquids at the molecular level: facts, problems, and controversies. *Angew. Chem. Int. Ed.* **2008,** *47*, 654-670.
3. Plechkova, N. V.; Seddon, K. R., Applications of ionic liquids in the chemical industry. *Chem. Soc. Rev.* **2008,** *37*, 123-150.
4. Steinrück, H.-P., Recent developments in the study of ionic liquid interfaces using X-ray photoelectron spectroscopy and potential future directions. *Phys. Chem. Chem. Phys.* **2012,** *14*, 5010-5029.
5. Lovelock, K. R., Influence of the ionic liquid/gas surface on ionic liquid chemistry. *Phys. Chem. Chem. Phys.* **2012,** *14*, 5071-5089.
6. Hayes, R.; Warr, G. G.; Atkin, R., Structure and nanostructure in ionic liquids. *Chem. Rev.* **2015,** *115*, 6357-6426.
7. Heym, F.; Etzold, B. J. M.; Kern, C.; Jess, A., Analysis of evaporation and thermal decomposition of ionic liquids by thermogravimetrical analysis at ambient pressure and high vacuum. *Green Chem.* **2011,** *13*, 1453-1466.
8. Zaitsau, D. H.; Kabo, G. J.; Strechan, A. A.; Paulechka, Y. U.; Tschersich, A.; Verevkin, S. P.; Heintz, A., Experimental vapor pressures of 1-alkyl-3-methylimidazolium bis(trifluoromethylsulfonyl)imides and a correlation scheme for estimation of vaporization enthalpies of ionic liquids. *J. Phys. Chem. A* **2006,** *110*, 7303-7306.
9. Zaitsau, D. H.; Yermalayeu, A. V.; Emel'yanenko, V. N.; Verevkin, S. P., Thermodynamics of Imidazolium-Based Ionic Liquids Containing the Trifluoromethanesulfonate Anion. *Chem. Eng. Technol.* **2018,** *41*, 1604-1612.
10. Zaitsau, D. H.; Yermalayeu, A. V.; Schubert, T. J. S.; Verevkin, S. P., Alkyl-imidazolium tetrafluoroborates: Vapor pressure, thermodynamics of vaporization, and enthalpies of formation. *J. Mol. Liq.* **2017,** *242*, 951-957.
11. Zaitsau, D. H.; Yermalayeu, A. V.; Emel'yanenko, V. N.; Butler, S.; Schubert, T.; Verevkin, S. P., Thermodynamics of Imidazolium-Based Ionic Liquids Containing PF6 Anions. *J. Phys. Chem. B* **2016,** *120*, 7949-7957.
12. Borra, E. F.; Seddiki, O.; Angel, R.; Eisenstein, D.; Hickson, P.; Seddon, K. R.; Worden, S. P., Deposition of metal films on an ionic liquid as a basis for a lunar telescope. *Nature* **2007,** *447*, 979-981.
13. Binnemans, K., Ionic liquid crystals. *Chem. Rev.* **2005,** *105*, 4148-4204.
14. Johnston, M.; Lee, J. J.; Chottiner, G. S.; Miller, B.; Tsuda, T.; Hussey, C. L.; Scherson, D. A., Electrochemistry in ultrahigh vacuum: underpotential deposition of Al on polycrystalline W and Au from room temperature AlCl(3)/1-ethyl-3-methylimidazolium chloride melts. *J. Phys. Chem. B* **2005,** *109*, 11296-11300.
15. Hapiot, P.; Lagrost, C., Electrochemical reactivity in room-temperature ionic liquids. *Chem. Rev.* **2008,** *108*, 2238-2264.
16. Endres, F.; Hofft, O.; Borisenko, N.; Gasparotto, L. H.; Prowald, A.; Al-Salman, R.; Carstens, T.; Atkin, R.; Bund, A.; Zein El Abedin, S., Do solvation layers of ionic liquids influence electrochemical reactions? *Physical chemistry chemical physics : PCCP* **2010,** *12*, 1724-32.
17. Armand, M.; Endres, F.; MacFarlane, D. R.; Ohno, H.; Scrosati, B., Ionic-liquid materials for the electrochemical challenges of the future. *Nature Mater* **2010,** *8*, 621-629.
18. Weingarth, D.; Foelske-Schmitz, A.; Wokaun, A.; Kötz, R., In situ electrochemical XPS study of the Pt/[EMIM][BF4] system. *Electrochem. Commun.* **2011,** *13*, 619-622.
19. Reyna-González, J. M.; Reyes-López, J. C.; Aguilar-Martínez, M., Silver and silver–copper electrodeposition from a pyridinium-based ionic liquid. *Electrochim. Acta* **2013,** *94*, 344-352.
20. Goossens, K.; Lava, K.; Bielawski, C. W.; Binnemans, K., Ionic Liquid Crystals: Versatile Materials. *Chem. Rev.* **2016,** *116*, 4643-4807.
21. Liu, Z.; Cui, T.; Lu, T. Q.; Ghazvini, M. S.; Endres, F., Anion Effects on the Solid/Ionic Liquid Interface and the Electrodeposition of Zinc. *J. Phys. Chem. C* **2016,** *120*, 20224-20231.
22. Iwahashi, T.; Miwa, Y.; Zhou, W.; Sakai, Y.; Yamagata, M.; Ishikawa, M.; Kim, D.; Ouchi, Y., IV-SFG studies on the effect of Li+ in extending the electrochemical window at the Pt |[C2mim][FSA] interface. *Electrochem. Commun.* **2016,** *72*, 54-58.

23. Greco, F.; Shin, S.; Williams, F. J.; Heller, B. S. J.; Maier, F.; Steinrück, H.-P., Potential Screening at Electrode/Ionic Liquid Interfaces from In Situ X-ray Photoelectron Spectroscopy. *ChemistryOpen* **2019,** *8*, 1365-1368.
24. Shin, S.; Greco, F.; Maier, F.; Steinrück, H.-P., Enrichment effects of ionic liquid mixtures at polarized electrode interfaces monitored by potential screening. *Phys. Chem. Chem. Phys.* **2021,** *23*, 10756-10762.
25. Welton, T., Room-Temperature Ionic Liquids. Solvents for Synthesis and Catalysis. *Chem. Rev.* **1999,** *99*, 2071-2084.
26. Wasserscheid, P.; Keim, W., Ionic Liquids—New "Solutions" for Transition Metal Catalysis. *Angew. Chem. Int. Ed.* **2000,** *39*, 3772-3789.
27. Mehnert, C. P.; Mozeleski, E. J.; Cook, R. A., Supported ionic liquid catalysis investigated for hydrogenation reactions. *Chem. Commun.* **2002**, 3010-3011.
28. Mehnert, C. P.; Cook, R. A.; Dispenziere, N. C.; Afeworki, M., Supported ionic liquid catalysis--a new concept for homogeneous hydroformylation catalysis. *J. Am. Chem. Soc.* **2002,** *124*, 12932-12933.
29. Riisager, A.; Fehrmann, R.; Haumann, M.; Gorle, B. S. K.; Wasserscheid, P., Stability and Kinetic Studies of Supported Ionic Liquid Phase Catalysts for Hydroformylation of Propene. *Ind. Eng. Chem. Res.* **2005,** *44*, 9853-9859.
30. Riisager, A.; Fehrmann, R.; Flicker, S.; van Hal, R.; Haumann, M.; Wasserscheid, P., Very stable and highly regioselective supported ionic-liquid-phase (SILP) catalysis: continuous-flow fixed-bed hydroformylation of propene. *Angew. Chem. Int. Ed.* **2005,** *44*, 815-819.
31. Riisager, A.; Fehrmanna, R.; Haumannb, M.; Wasserscheidb, P., Supported ionic liquids: versatile reaction and separation media. *Top. Catal.* **2006,** *40*, 91-102.
32. Huang, J.; Jiang, T.; Gao, H.; Han, B.; Liu, Z.; Wu, W.; Chang, Y.; Zhao, G., Pd nanoparticles immobilized on molecular sieves by ionic liquids: heterogeneous catalysts for solvent-free hydrogenation. *Angew. Chem. Int. Ed.* **2004,** *43*, 1397-1399.
33. Breitenlechner, S.; Fleck, M.; Müller, T. E.; Suppan, A., Solid catalysts on the basis of supported ionic liquids and their use in hydroamination reactions. *J. Mol. Catal. A: Chem.* **2004,** *214*, 175-179.
34. Gu, Y.; Ogawa, C.; Kobayashi, J.; Mori, Y.; Kobayashi, S., A heterogeneous silica-supported scandium/ionic liquid catalyst system for organic reactions in water. *Angew. Chem. Int. Ed.* **2006,** *45*, 7217-7220.
35. Kernchen, U.; Etzold, B.; Korth, W.; Jess, A., Solid Catalyst with Ionic Liquid Layer (SCILL) – A New Concept to Improve Selectivity Illustrated by Hydrogenation of Cyclooctadiene. *Chem. Eng. Technol.* **2007,** *30*, 985-994.
36. Zhang, Q.; Zhang, S.; Deng, Y., Recent advances in ionic liquid catalysis. *Green Chem.* **2011,** *13*, 2619.
37. Steinrück, H.-P.; Wasserscheid, P., Ionic Liquids in Catalysis. *Catal. Lett.* **2015,** *145*, 380-397.
38. May, B.; Hönle, M.; Heller, B.; Greco, F.; Bhuin, R.; Steinrück, H.-P.; Maier, F., Surface-Induced Changes in the Thermochromic Transformation of an Ionic Liquid Cobalt Thiocyanate Complex. *J. Phys. Chem. Lett.* **2017,** *8*, 1137-1141.
39. Cui, C.; Sa, R.; Hong, Z.; Zhong, H.; Wang, R., Ionic-Liquid-Modified Click-Based Porous Organic Polymers for Controlling Capture and Catalytic Conversion of CO2. *ChemSusChem* **2020,** *13*, 180-187.
40. Wang, W.; Zhang, Y.; Yang, Z.; Zhang, Z.; Fang, W.; Niu, D.; He, H.; Xu, F., Efficient synthesis of isosorbide-based polycarbonate with scalable dicationic ionic liquid catalysts by balancing the reactivity of the endo-OH and exo-OH. *Green Chem.* **2021,** *23*, 973-982.
41. Steinrück, H.-P., Surface science goes liquid ! *Surf. Sci.* **2010,** *604*, 481-484.
42. Steinrück, H.-P.; Libuda, J.; Wasserscheid, P.; Cremer, T.; Kolbeck, C.; Laurin, M.; Maier, F.; Sobota, M.; Schulz, P. S.; Stark, M., Surface science and model catalysis with ionic liquid-modified materials. *Adv. Mater.* **2011,** *23*, 2571-2587.
43. Zhang, G. R.; Etzold, B. J. M., Emerging Applications of Solid Catalysts with Ionic Liquid Layer Concept in Electrocatalysis. *Adv. Func. Mater.* **2021,** *31*, 2010977.
44. Wen, R.; Rahn, B.; Magnussen, O. M., Potential-Dependent Adlayer Structure and Dynamics at the Ionic Liquid/Au(111) Interface: A Molecular-Scale In Situ Video-STM Study. *Angew. Chem. Int. Ed.* **2015,** *54*, 6062-6066.
45. Zhong, Y. X.; Yan, J. W.; Li, M. G.; Chen, L.; Mao, B. W., The Electric Double Layer in an Ionic Liquid Incorporated with Water Molecules: Atomic Force Microscopy Force Curve Study. *Chemelectrochem* **2016,** *3*, 2221-2226.

46. Uhl, B.; Huang, H.; Alwast, D.; Buchner, F.; Behm, R. J., Interaction of ionic liquids with noble metal surfaces: structure formation and stability of [OMIM][TFSA] and [EMIM][TFSA] on Au(111) and Ag(111). *Phys. Chem. Chem. Phys.* **2015,** *17*, 23816-23832.
47. Lexow, M.; Maier, F.; Steinrück, H.-P., Ultrathin ionic liquid films on metal surfaces: adsorption, growth, stability and exchange phenomena. *Adv Phys: X* **2020,** *5*, 1761266.
48. Cremer, T.; Stark, M.; Deyko, A.; Steinrück, H.-P.; Maier, F., Liquid/solid interface of ultrathin ionic liquid films: [C1C1Im][Tf2N] and [C8C1Im][Tf2N] on Au(111). *Langmuir* **2011,** *27*, 3662-3671.
49. Uhl, B.; Cremer, T.; Roos, M.; Maier, F.; Steinrück, H.-P.; Behm, R. J., At the ionic liquid|metal interface: structure formation and temperature dependent behavior of an ionic liquid adlayer on Au(111). *Phys. Chem. Chem. Phys.* **2013,** *15*, 17295-17302.
50. Cremer, T.; Wibmer, L.; Krick Calderón, S.; Deyko, A.; Maier, F.; Steinrück, H. P., Interfaces of ionic liquids and transition metal surfaces-adsorption, growth, and thermal reactions of ultrathin [C1C1Im][Tf2N] films on metallic and oxidised Ni(111) surfaces. *Phys. Chem. Chem. Phys.* **2012,** *14*, 5153-5163.
51. Muller, E. A.; Strader, M. L.; Johns, J. E.; Yang, A.; Caplins, B. W.; Shearer, A. J.; Suich, D. E.; Harris, C. B., Femtosecond electron solvation at the ionic liquid/metal electrode interface. *J. Am. Chem. Soc.* **2013,** *135*, 10646-10653.
52. Rietzler, F.; Piermaier, M.; Deyko, A.; Steinrück, H.-P.; Maier, F., Electrospray ionization deposition of ultrathin ionic liquid films: [C8C1Im]Cl and [C8C1Im][Tf2N] on Au(111). *Langmuir* **2014,** *30*, 1063-1071.
53. Rietzler, F.; Nagengast, J.; Steinrück, H.-P.; Maier, F., Interface of Ionic Liquids and Carbon: Ultrathin [C1C1Im][Tf2N] Films on Graphite and Graphene. *J. Phys. Chem. C* **2015,** *119*, 28068-28076.
54. Rietzler, F.; May, B.; Steinrück, H.-P.; Maier, F., Switching adsorption and growth behavior of ultrathin [C2C1Im][OTf] films on Au(111) by Pd deposition. *Phys. Chem. Chem. Phys.* **2016,** *18*, 25143-25150.
55. Zhang, S.; Lu, Y.; Peng, C.; Liu, H.; Jiang, D., Structure and Interaction of Ionic Liquid Monolayer on Graphite from First-Principles. *J. Phys. Chem. C* **2019,** *123*, 618-624.
56. Lexow, M.; Talwar, T.; Heller, B. S. J.; May, B.; Bhuin, R. G.; Maier, F.; Steinrück, H.-P., Time-dependent changes in the growth of ultrathin ionic liquid films on Ag(111). *Phys. Chem. Chem. Phys.* **2018,** *20*, 12929-12938.
57. Lexow, M.; Heller, B. S. J.; Maier, F.; Steinrück, H.-P., Anion Exchange at the Liquid/Solid Interface of Ultrathin Ionic Liquid Films on Ag(111). *ChemPhysChem* **2018,** *19*, 2978-2984.
58. Lexow, M.; Heller, B. S. J.; Partl, G.; Bhuin, R. G.; Maier, F.; Steinrück, H.-P., Cation Exchange at the Interfaces of Ultrathin Films of Fluorous Ionic Liquids on Ag(111). *Langmuir* **2019,** *35*, 398-405.
59. Massicot, S.; Sasaki, T.; Lexow, M.; Shin, S.; Maier, F.; Kuwabata, S.; Steinrück, H.-P., Adsorption, Wetting, Growth, and Thermal Stability of the Protic Ionic Liquid Diethylmethylammonium Trifluoromethanesulfonate on Ag(111) and Au(111). *Langmuir* **2021,** *37*, 11552-11560.
60. Liu, M.; Shao, Y.; Wu, Q., Charge reduction in ions in the ionic liquid 1-ethy-2,3-dimethylimidazolium bis(trifluoromethanesulfonyl)imide on the Au(111) surface. *Theo. Chem. Acc.* **2020,** *139:24*.
61. Hayes, R.; Borisenko, N.; Tam, M. K.; Howlett, P. C.; Endres, F.; Atkin, R., Double Layer Structure of Ionic Liquids at the Au(111) Electrode Interface: An Atomic Force Microscopy Investigation. *J. Phys. Chem. C* **2011,** *115*, 6855-6863.
62. Endres, F.; Borisenko, N.; El Abedin, S. Z.; Hayes, R.; Atkin, R., The interface ionic liquid(s)/electrode(s): in situ STM and AFM measurements. *Faraday Discuss.* **2012,** *154*, 221-233.
63. Li, H.; Endres, F.; Atkin, R., Effect of alkyl chain length and anion species on the interfacial nanostructure of ionic liquids at the Au(111)-ionic liquid interface as a function of potential. *Phys. Chem. Chem. Phys.* **2013,** *15*, 14624-14633.
64. Carstens, T.; Gustus, R.; Höfft, O.; Borisenko, N.; Endres, F.; Li, H.; Wood, R. J.; Page, A. J.; Atkin, R., Combined STM, AFM, and DFT Study of the Highly Ordered Pyrolytic Graphite/1-Octyl-3-methyl-imidazolium Bis(trifluoromethylsulfonyl)imide Interface. *J. Phys. Chem. C* **2014,** *118*, 10833-10843.
65. Zhang, X.; Zhong, Y. X.; Yan, J. W.; Su, Y. Z.; Zhang, M.; Mao, B. W., Probing double layer structures of Au (111)-BMIPF6 ionic liquid interfaces from potential-dependent AFM force curves. *Chem. Commun.* **2012,** *48*, 582-584.
66. Cheng, H.-W.; Stock, P.; Moeremans, B.; Baimpos, T.; Banquy, X.; Renner, F. U.; Valtiner, M., Characterizing the Influence of Water on Charging and Layering at Electrified Ionic-Liquid/Solid Interfaces. *Adv. Mater. Interfaces* **2015,** *2*, 1500159.

67. Li, M.-G.; Chen, L.; Zhong, Y.-X.; Chen, Z.-B.; Yan, J.-W.; Mao, B.-W., The electrochemical interface of Ag(111) in 1-ethyl-3-methylimidazolium bis(trifluoromethylsulfonyl)imide ionic liquid—A combined in-situ scanning probe microscopy and impedance study. *Electrochim. Acta* **2016,** *197*, 282-289.
68. Hoffmann, V.; Pulletikurthi, G.; Carstens, T.; Lahiri, A.; Borodin, A.; Schammer, M.; Horstmann, B.; Latz, A.; Endres, F., Influence of a silver salt on the nanostructure of a Au(111)/ionic liquid interface: an atomic force microscopy study and theoretical concepts. *Phys. Chem. Chem. Phys.* **2018,** *20*, 4760-4771.
69. Sobota, M.; Nikiforidis, I.; Hieringer, W.; Paape, N.; Happel, M.; Steinrück, H.-P.; Gorling, A.; Wasserscheid, P.; Laurin, M.; Libuda, J., Toward ionic-liquid-based model catalysis: growth, orientation, conformation, and interaction mechanism of the [Tf2N]- anion in [BMIM][Tf2N] thin films on a well-ordered alumina surface. *Langmuir* **2010,** *26*, 7199-7207.
70. Biedron, A. B.; Garfunkel, E. L.; Castner, E. W., Jr.; Rangan, S., Ionic liquid ultrathin films at the surface of Cu(100) and Au(111). *J. Chem. Phys.* **2017,** *146*, 054704.
71. Foulston, R.; Gangopadhyay, S.; Chiutu, C.; Moriarty, P.; Jones, R. G., Mono- and multi-layer adsorption of an ionic liquid on Au(110). *Phys. Chem. Chem. Phys.* **2012,** *14*, 6054-6066.
72. Syres, K. L.; Jones, R. G., Adsorption, Desorption, and Reaction of 1-Octyl-3-methylimidazolium Tetrafluoroborate, [C(8)C(1)Im][BF(4)], Ionic Liquid Multilayers on Cu(111). *Langmuir* **2015,** *31*, 9799-9808.
73. Wiesendanger, R.; Mulvey, T., *Scanning Probe Microscopy and Spectroscopy, Methods and Applications*. Cambridge University Press: 1994.
74. Morita, S.; Meyer, E.; Wiesendanger, R., *Noncontact Atomic Force Microscopy*. Springer: 2002.
75. Voigtländer, B., *Atomic Force Microscopy*. Springer: 2019.
76. Meyer, E.; Hug, H.-J.; Bennewitz, R., *Scanning probe microscopy*. Springer: 2021; Vol. 2.
77. Binnig, G.; Rohrer, H.; Gerber, C.; Weibel, E., Surface Studies by Scanning Tunneling Microscopy. *Phys. Rev. Lett.* **1982,** *49*, 57-61.
78. Binnig, G., Tunneling through a controllable vacuum gap. *App. Phys. Lett.* **1982,** *40*, 178.
79. Tersoff, J.; Hamann, D. R., Theory of the scanning tunneling microscope. *Phys. Rev. B* **1985,** *31*, 805-813.
80. Viernow, J.; Petrovykh, D. Y.; Kirakosian, A.; Lin, J.-L.; Men, F. K.; Henzler, M.; Himpsel, F. J., Chemical imaging of insulators by STM. *Phys. Rev. B* **1999,** *59*, 10356.
81. Avouris, P.; Wolkow, R., Scanning tunneling microscopy of insulators: CaF2 epitaxy on Si (111). *Appl. Phys. Lett.* **1989,** *55*, 1074-1076.
82. Atkin, R.; El Abedin, S. Z.; Hayes, R.; Gasparotto, L. H. S.; Borisenko, N.; Endres, F., AFM and STM Studies on the Surface Interaction of [BMP]TFSA and [EMIm]TFSA Ionic Liquids with Au(111). *J. Phys. Chem. C* **2009,** *113*, 13266-13272.
83. Kazinczi, R.; Szöcs, E.; Kálmán, E.; Nagy, P., Novel methods for preparing EC STM tips. *Appl. Phys. A* **1998,** *66*, S535–S538.
84. Sass, J.; Gimzewski, J.; Haiss, W.; Besocke, K.; Lackey, D., Theoretical aspects and experimental results of STM studies in polar liquids. *J. Phys.: Condens. Matter* **1991,** *3*, S121-S126.
85. Binnig, G.; Quate, C. F.; Gerber, C., Atomic force microscope. *Phys. Rev. Lett.* **1986,** *56*, 930-933.
86. Meyer, G.; Amer, N. M., Novel optical approach to atomic force microscopy. *Appl. Phys. Lett.* **1988,** *53*, 1045.
87. Giessibl, F. J., High-speed force sensor for force microscopy and profilometry utilizing a quartz tuning fork. *Appl. Phys. Lett.* **1998,** *73*, 3956-3958.
88. Giessibl, F. J., Advances in atomic force microscopy. *Rev. Mod. Phys.* **2003,** *75*, 949-983.
89. Hanke, F.; Björk, J., Structure and local reactivity of the Au(111) surface reconstruction. *Phys. Rev. B* **2013,** *87*, 235422.
90. Corso, M.; Auwärter, W.; Muntwiler, M.; Tamai, A.; Greber, T.; Osterwalder, J., Boron nitride nanomesh. *Science* **2004,** *303*, 217-220.
91. Berner, S.; Corso, M.; Widmer, R.; Groening, O.; Laskowski, R.; Blaha, P.; Schwarz, K.; Goriachko, A.; Over, H.; Gsell, S.; Schreck, M.; Sachdev, H.; Greber, T.; Osterwalder, J., Boron nitride nanomesh: functionality from a corrugated monolayer. *Angew. Chem. Int. Ed.* **2007,** *46*, 5115-5119.
92. Bunk, O.; Corso, M.; Martoccia, D.; Herger, R.; Willmott, P. R.; Patterson, B. D.; Osterwalder, J.; van der Veen, I.; Greber, T., Surface X-ray diffraction study of boron-nitride nanomesh in air. *Surface Science* **2007,** *601*, L7-L10.
93. Laskowski, R.; Blaha, P., Ab initiostudy of h−BN nanomeshes on Ru(001), Rh(111), and Pt(111). *Phys. Rev. B* **2010,** *81*, 075418.

94. Ng, M. L.; Preobrajenski, A. B.; Vinogradov, A. S.; Martensson, N., Formation and temperature evolution of Au nanoparticles supported on the h-BN nanomesh. *Surface Science* **2008,** *602*, 1250-1255.
95. N'Diaye, A. T.; Gerber, T.; Busse, C.; Myslivecek, J.; Coraux, J.; Michely, T., A versatile fabrication method for cluster superlattices. *New J. Phys.* **2009,** *11*, 103045.
96. Gotterbarm, K.; Späth, F.; Bauer, U.; Bronnbauer, C.; Steinrück, H.-P.; Papp, C., Reactivity of Graphene-Supported Pt Nanocluster Arrays. *ACS. Catal.* **2015,** *5*, 2397-2403.
97. Gotterbarm, K.; Steiner, C.; Bronnbauer, C.; Bauer, U.; Steinrück, H.-P.; Maier, S.; Papp, C., Graphene-Templated Growth of Pd Nanoclusters. *J. Phys. Chem. C* **2014,** *118*, 15934-15939.
98. Papp, C., From Flat Surfaces to Nanoparticles: In Situ Studies of the Reactivity of Model Catalysts. *Catal. Lett.* **2017,** *147*, 2-19.
99. Will, M.; Atodiresei, N.; Caciuc, V.; Valerius, P.; Herbig, C.; Michely, T., A Monolayer of Hexagonal Boron Nitride on Ir(111) as a Template for Cluster Superlattices. *ACS Nano* **2018,** *12*, 6871-6880.
100. Hurley, F. H.; Wier Jr, T. P., Electrodeposition of metals from fused quaternary ammonium salts. *J. Electrochem. Soc.* **1951,** *98*, 203.
101. Cooper, E.; Sullivan, E., Proceedings of the 8th International Symposium on Molten Salts. **1992**, 386-396.
102. Bonhôte, P.; Dias, A. P.; Papageorgiou, N.; Kalyanasundaram, K.; Grätzel, M., Hydrophobic, Highly Conductive Ambient-Temperature Molten Salts. *Inorg. Chem.* **1996,** *35*, 1168-1178.
103. Armstrong, D. W.; He, L.; Liu, Y. S., Examination of ionic liquids and their interaction with molecules, when used as stationary phases in gas chromatography. *Anal. Chem.* **1999,** *71*, 3873-3876.
104. Seddon, K. R., Ionic liquids: a taste of the future. *Nat. Mater.* **2003,** *2*, 363-365.
105. Heller, B., Surface Composition and Enrichment Effects in Mixtures of Functionalized and Non-Functionalized Ionic Liquids. *Friedrich-Alexander-Universität Erlangen-Nürnberg* **2020,** *PhD dissertation*.
106. Niedermaier, I.; Kolbeck, C.; Steinrück, H.-P.; Maier, F., Dual analyzer system for surface analysis dedicated for angle-resolved photoelectron spectroscopy at liquid surfaces and interfaces. *Rev. Sci. Instrum.* **2016,** *87*, 045105.
107. Lexow, M., Ultrathin Ionic Liquid Films on Metal Surfaces: Growth, Stability and Exchange Phenomena. *Friedrich-Alexander-Universität Erlangen-Nürnberg* **2020,** *PhD dissertation*.
108. Musket, R. G.; McLean, W.; Colmenares, C. A.; Makowiecki, D. M.; Siekhaus, W. J., Preparation of atomically clean surfaces of selected elements: A review. *Appl. Surf. Sci.* **1982,** *10*, 143-207.
109. Abegunde, O. O.; Akinlabi, E. T.; Oladijo, O. P.; Akinlabi, S.; Ude, A. U., Overview of thin film deposition techniques. *AIMS Mat. Sci.* **2019,** *6*, 174-199.
110. Lovelock, K. R.; Kolbeck, C.; Cremer, T.; Paape, N.; Schulz, P. S.; Wasserscheid, P.; Maier, F.; Steinrück, H.-P., Influence of different substituents on the surface composition of ionic liquids studied using ARXPS. *J. Phys. Chem. B* **2009,** *113*, 2854-2864.
111. Horcas, I.; Fernandez, R.; Gomez-Rodriguez, J. M.; Colchero, J.; Gomez-Herrero, J.; Baro, A. M., WSXM: a software for scanning probe microscopy and a tool for nanotechnology. *Rev. Sci. Instrum.* **2007,** *78*, 013705.
112. Meusel, M.; Lexow, M.; Gezmis, A.; Schötz, S.; Wagner, M.; Bayer, A.; Maier, F.; Steinrück, H.-P., Atomic Force and Scanning Tunneling Microscopy of Ordered Ionic Liquid Wetting Layers from 110 K up to Room Temperature. *ACS Nano* **2020,** *14*, 9000-9010.
113. Uhl, B.; Buchner, F.; Alwast, D.; Wagner, N.; Behm, R. J., Adsorption of the ionic liquid [BMP][TFSA] on Au(111) and Ag(111): substrate effects on the structure formation investigated by STM. *Beilstein J. Nanotechnol.* **2013,** *4*, 903-918.
114. Meusel, M.; Lexow, M.; Gezmis, A.; Bayer, A.; Maier, F.; Steinrück, H.-P., Growth of Multilayers of Ionic Liquids on Au(111) Investigated by Atomic Force Microscopy in Ultrahigh Vacuum. *Langmuir* **2020,** *36*, 13670-13681.
115. Meusel, M.; Gezmis, A.; Jaekel, S.; Lexow, M.; Bayer, A.; Maier, F.; Steinrück, H.-P., Time- and Temperature-Dependent Growth Behavior of Ionic Liquids on Au(111) Studied by Atomic Force Microscopy in Ultrahigh Vacuum. *J. Phys. Chem. C* **2021,** *125*, 20439-20449.
116. Tokuda, H.; Hayamizu, K.; Ishii, K.; Susan, M. A.; Watanabe, M., Physicochemical properties and structures of room temperature ionic liquids. 2. Variation of alkyl chain length in imidazolium cation. *J. Phys. Chem. B* **2005,** *109*, 6103-6110.
117. Schwoebel, R. L.; Shipsey, E. J., Step Motion on Crystal Surfaces. *J. Appl. Phys.* **1966,** *37*, 3682-3686.

118. Düll, F.; Meusel, M.; Spath, F.; Schötz, S.; Bauer, U.; Bachmann, P.; Steinhauer, J.; Steinrück, H.-P.; Bayer, A.; Papp, C., Growth and stability of Pt nanoclusters from 1 to 50 atoms on h-BN/Rh(111). *Phys. Chem. Chem. Phys.* **2019,** *21*, 21287-21295.
119. Düll, F., Metal Nanocluster Arrays as Model System for Catalysts. *Friedrich-Alexander-Universität Erlangen-Nürnberg* **2019,** *PhD dissertation*.

6. ACKNOWLEDGEMENTS (DANKSAGUNG)

Many people have supported me and contributed to where I am today, and for this I want to express my sincere gratitude.

First, I want to thank Prof. Dr. Hans-Peter Steinrück for entrusting me a new machine and for giving me the chance to learn how to establish and utilize such a device. I want to thank him for being a fair supervisor, a mentor and for giving excellent support and invaluable advice wherever possible.

I want to thank Dr. Andreas Bayer, Dr. Florian Maier, PD Dr. Hubertus Marbach, and PD Dr. Christian Papp for encouraging, challenging, mentoring, inspiring and supporting me throughout the last years and I want to appreciate all the discussions ranging from amusing conversations during lunch breaks to precise optimization of scientific work.

I want to express my gratitude to all my colleagues for creating and preserving an enjoyable atmosphere. Especially, I want to thank Dr. Michael Lepper and Dr. Margareta Wagner for being excellent mentors. I wish to thank Dr. Bettina Heller, Dr. Matthias Lexow, Francesco Greco, Rajan Adhikari and Julia Köbl for offering their assistance wherever necessary and possible, and I want to thank Simon Schötz, Stephen Massicot, Ulrike Paap, and Afra Gezmis for sharing their enthusiasm with me when mine got overshadowed by routine.

I want to thank Hans-Peter Bäumler and Bernd Kreß for practical advice when I was planning, building, or improving devices, for the support I needed to achieve most of it on my own, and for a helpful hand if it was required.

And I want to thank Susana Kreß and Andrea Meixner-Wolf for fighting bureaucracy and helping me with many little, but important, things.

Vielen Dank auch an Friedhold Wölfel, Thomas Hofmann, Bernd Hofmann, Werner Höfler und Viola Ziegler für die präzise Fertigung der vielen Bauteile die ich benötigt habe und für die schnelle Reparatur von Geräten bei außerplanmäßigen Wartungsarbeiten.

Vielen Dank an meine Familie und Freunde, besonders an meine Schwester Miriam und an Andreas, auf die ich mich immer verlassen kann, und ganz besonders an meine Partnerin Tabea für ihre Geduld, Unterstützung und aufmunternde Art. Zu guter Letzt, vielen Dank an meinen Vater, und in Gedenken meiner Mutter. Ich erkenne immer wieder Teile von euch in mir, und es sind gerade diese die mich hierhergeführt haben.

7. APPENDIX

Table A1: Summary of limitations, standard parameter, and examples of preparations.

Base pressures	preparation	analysis	load lock	load lock (not pumped)	UHV suitcase	preparation (pre bakeout)
[mbar]	$5 \cdot 10^{-11}$	$5 \cdot 10^{-11}$	$5 \cdot 10^{-8}$	$5 \cdot 10^{-6}$	$1 \cdot 10^{-10}$	$\sim 1 \cdot 10^{-9}$
STM (not AFM) can be operated at ambient pressure (for a function test) but not from 10^{+1} to 10^{-3} mbar.						

Room Temperature
295 ± 2 K

Manipulator position	x	y	z	ϕ	comment
transfer VT	20	5	50	170	
transfer LL	20	3	180	355	
sputtering	8	12	242	0	
evap. organic	8	12	240	210	
evap. IL	8	3	240	210	first manipulator then QCM (5.0 cm)
evap. metal	8	12	240	0	with new rod (45mm): z_{cell} ~ 9mm; careful!
H• source	8	12	240	20	
LEED	12	8	240	90	

Shutter positions	cell 1	cell 2	cell 3	cell 4	all closed
evap. organic	0°	90°	185°	270°	45°, 140°, 230°, 320°
evap. metal	154°	128°	200°	-	174°

Maximum parameter	T_{max}	I_{max}	cooling	comment
annealing in microscope	500 K	1.0 A	-	P_{max}: 8.0 W
annealing with cooling	T_M: 930 K ≙ T_S: ~1400 K	2.5 A	>650 K, N_2	T_M=$T_{manipulator}$, T_S=T_{sample}
annealing direct heating	depends on sample	5.0 A	no	do not use low Ω samples
evap. organic	700 °C	6.0 A	always	
evap. metal	-	2.5 A	always	
evap. IL	watch pressure*	*	always	*homebuild, max. not known
H• source	-	Em-control	always	$I_{Em,max}$: 80 mA

Examples	I	U	I_{Em}	I_{Flux}	p_{gas}	T	t	cooling
sputtering	-	1 kV	10 mA	18µA	Ar: 5E-5	RT	2 h	no
annealing Cu(111)	1.75 A	-450 V	30 mA	-	-	T_M: 630 K	10 min	no
annealing Au(111)	1.75 A	-450 V	30 mA	-	-	T_M: 630 K	10 min	no
annealing Rh(111)	1.95 A	-600 V	100 mA	-	-	T_M: 960 K	10 min	yes
annealing Pt(111)	1.90 A	-600 V	100 mA	-	-	T_M: 960 K	10 min	yes
evap. $[C_1C_1Im][Tf_2N]$	8.5 A	7.7 V	-	-	-	110-130 °C	~5min 1WL ≈ 83a.u.	yes
evap. 2H-TPP	1.5 A	-	-	-	-	375 °C	~5 min	yes
evap. 2H-TCNPP	1.7 A	-	-	-	-	410 °C	~5 min	yes
evap. Co	2.0 A	1 kV	8.7 mA	33.0 µA	-	-	~5 min	yes
evap. Fe	2.0 A	1 kV	6.5 mA	15.0 µA	-	-	~5 min	yes
evap. Cu	2.0 A	1 kV	9.7 mA	8.0 µA	-	-	~5 min	yes
evap. Pt	2.0 A	1 kV	11.0 mA	8.0 µA	-	-	~5 min	yes
T_M= manipulator temperature, T_S= sample temperature								

Thermocontact holder
material: steel
thickness: 2 mm

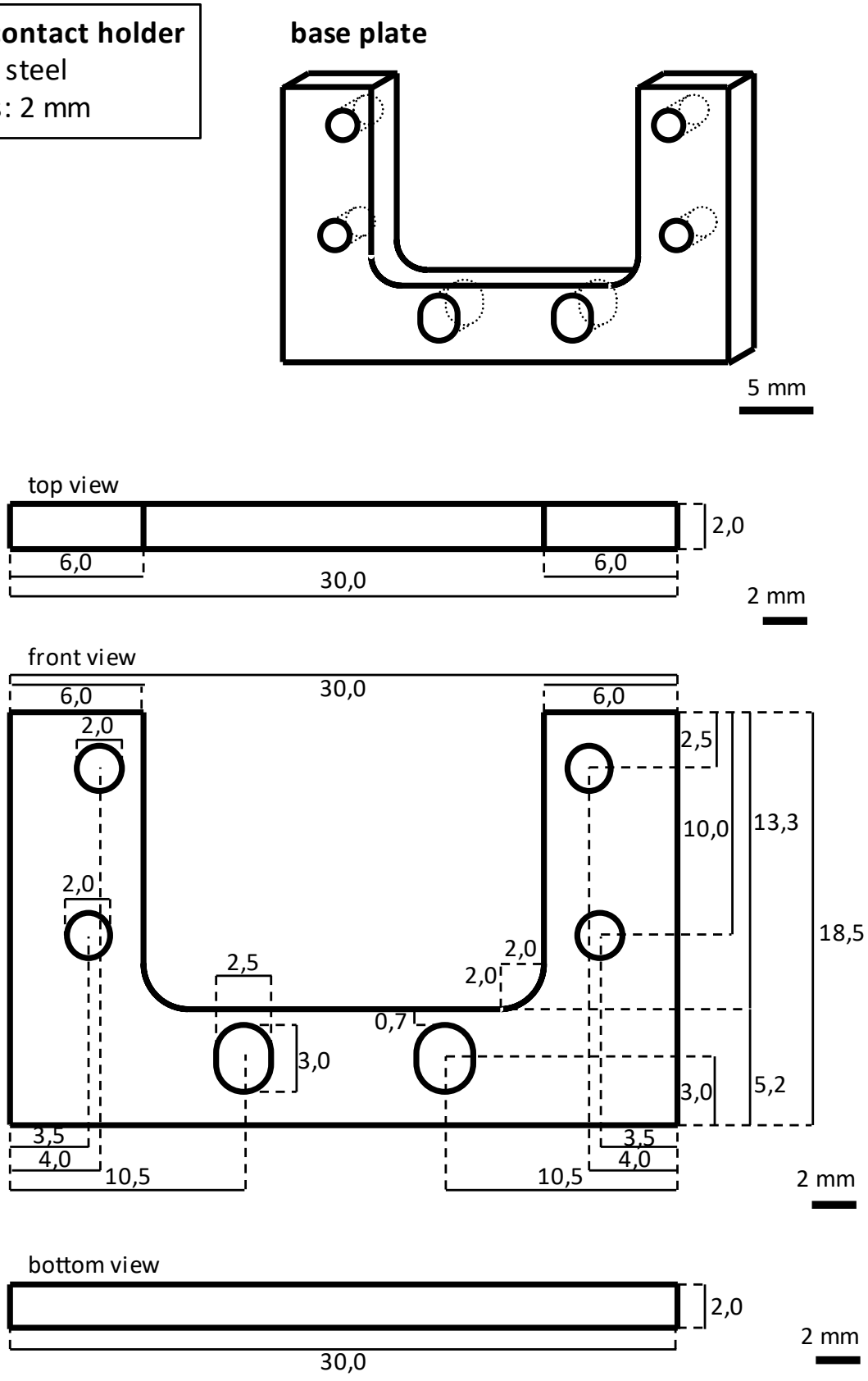

Figure A1: Technical drawings for the thermocontact holder at the manipulator.

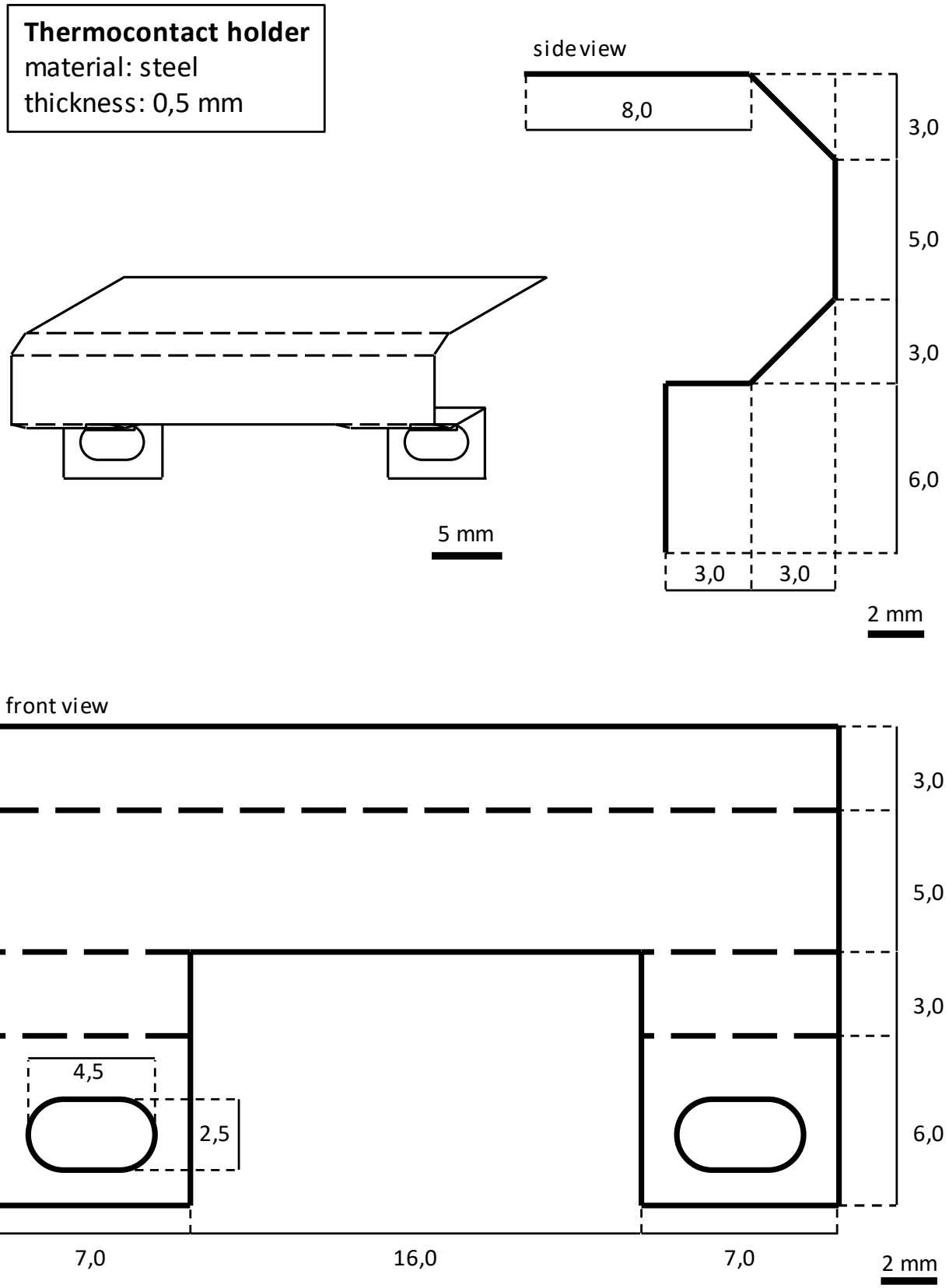

Figure A2: Technical drawings for the thermocontact holder at the manipulator.

Thermocontact holder
material: Al_2O_3

BCE Special Ceramics
2017603200 / 20424

ceramic, page 1

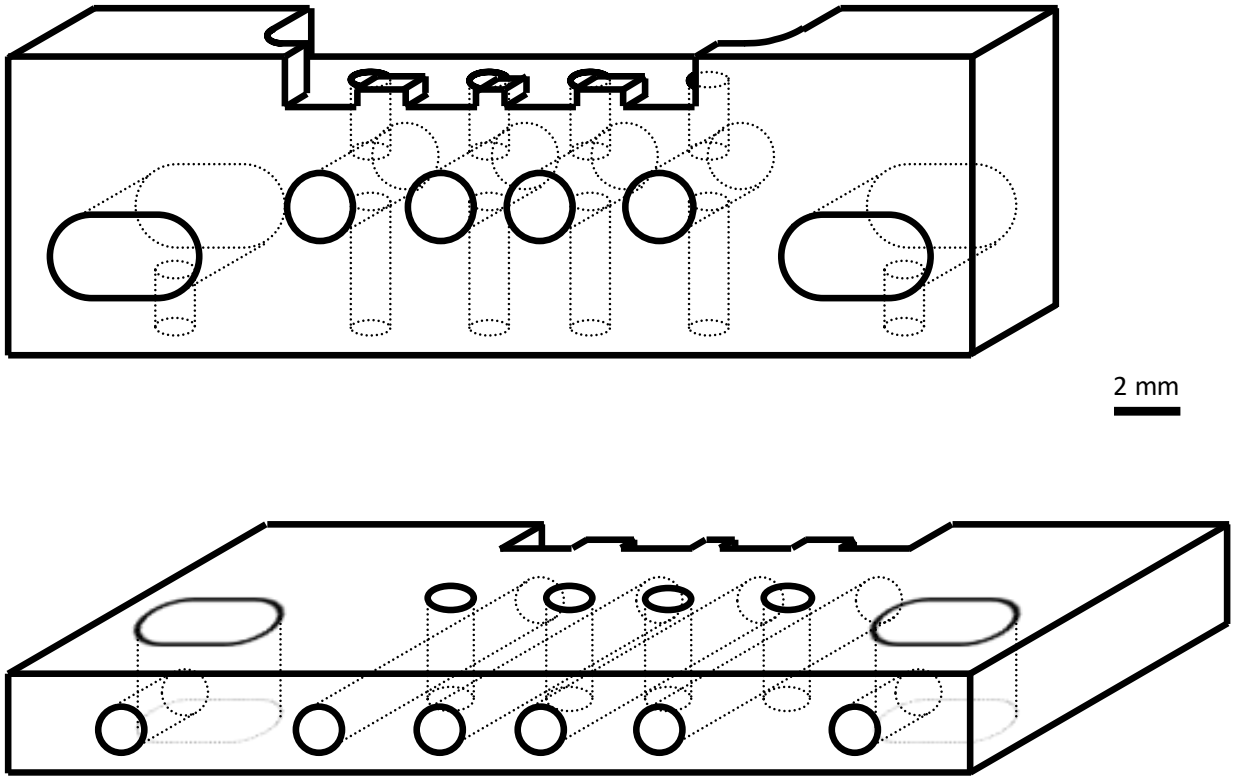

Figure A3: Technical drawings for the thermocontact holder at the manipulator.

ceramic, page 2

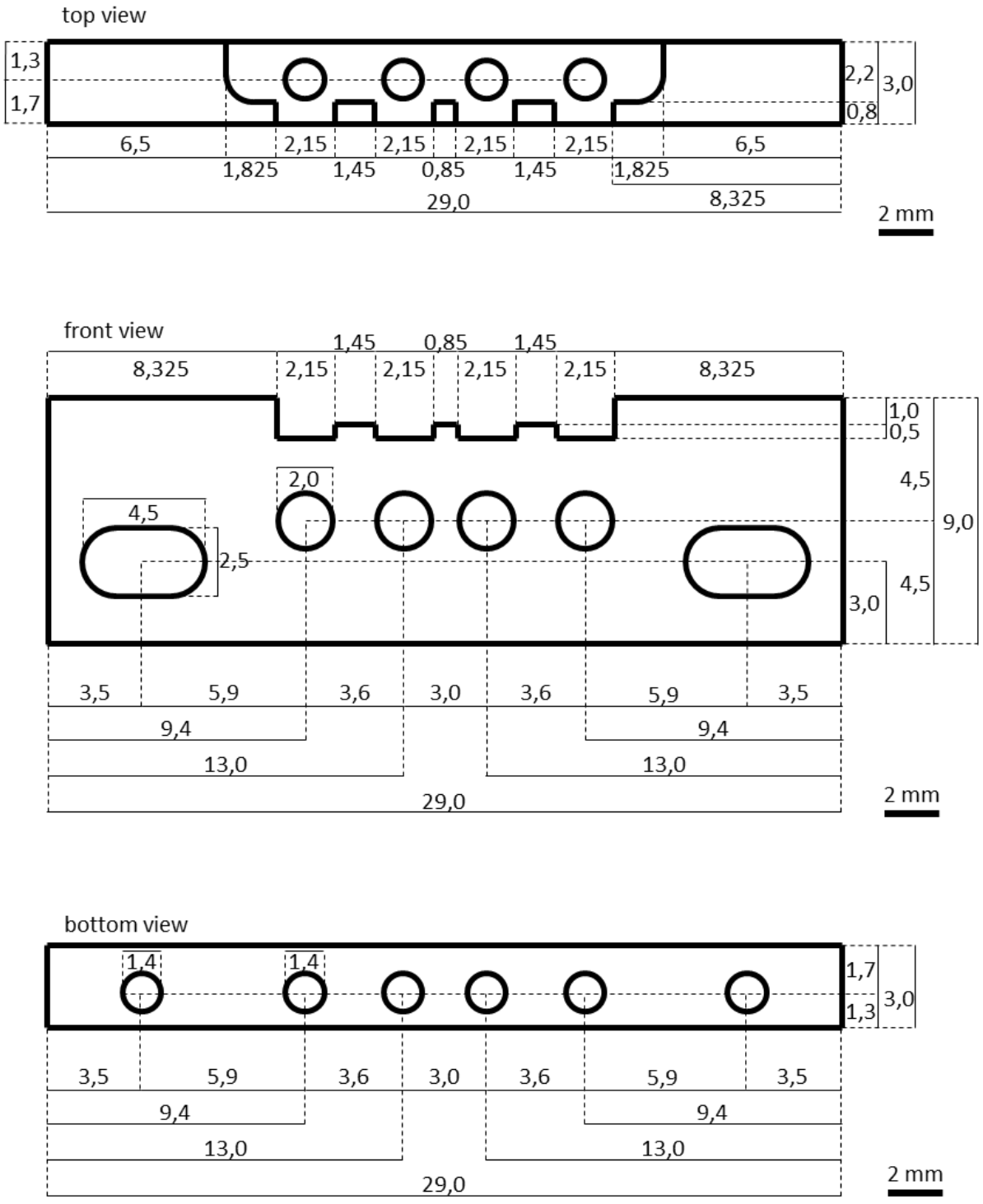

Figure A4: Technical drawings for the thermocontact holder at the manipulator.

Thermocontact holder – accessories

contact springs: 2x alumel, 2x chromel
material: TC type K
thickness: 0,1 mm

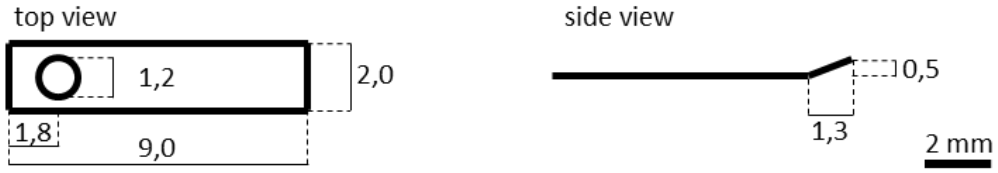

Screws:	- 4x steel	M2	7,7 mm	head: 1,9x3,6 Allen/Inbus
	- 1x alumel	M1,2	11 mm	head: 0,8x2,3 slotted
	- 1x chromel	M1,2	11 mm	head: 0,8x2,3 slotted
Nuts:	- 1x alumel	M1,2		
	- 1x chromel	M1,2		
Washers:	- 8x steel	M2		

Figure A5: Technical drawings for the thermocontact holder at the manipulator.

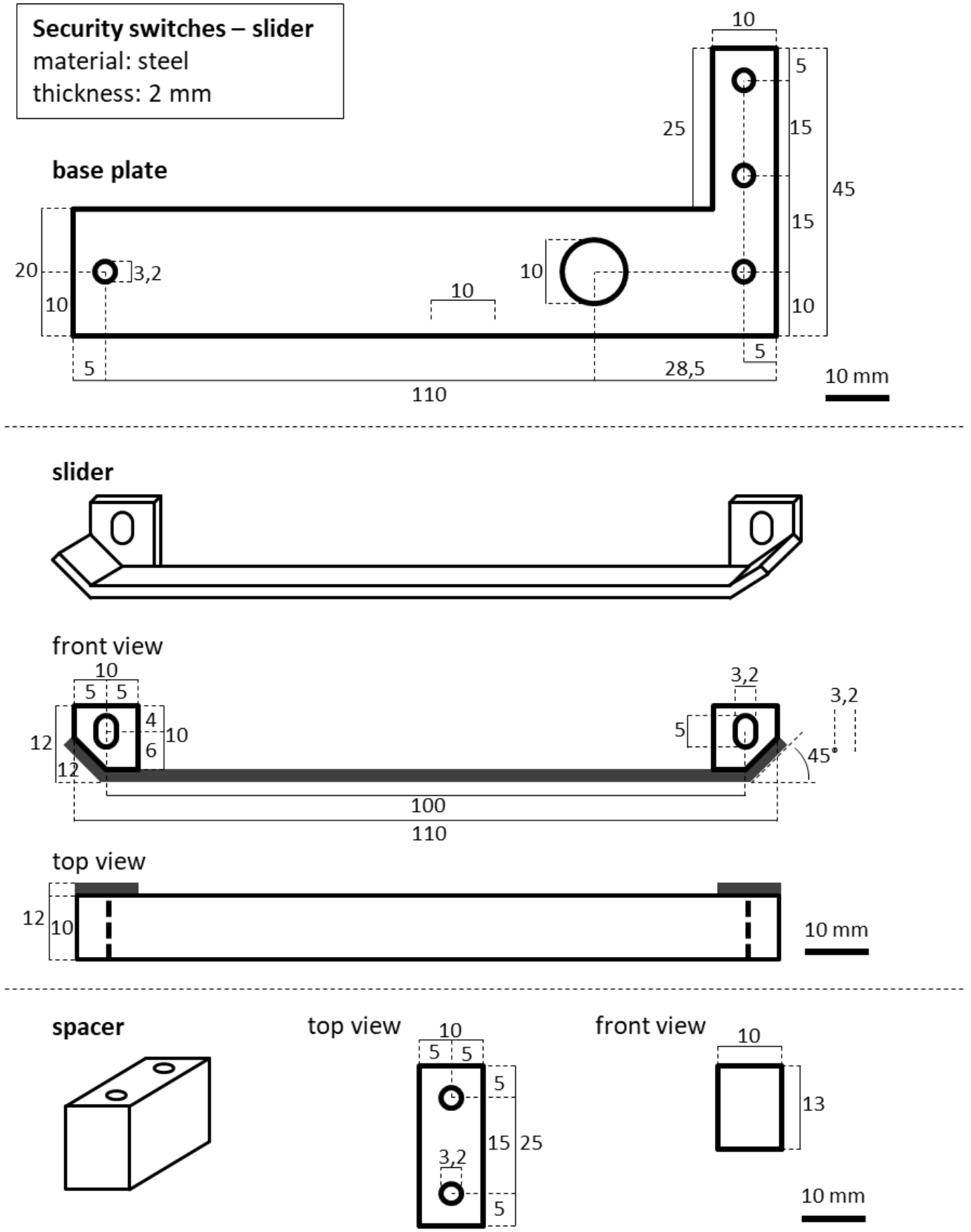

Figure A6: Technical drawings for the security switches for the manipulator z-drive.

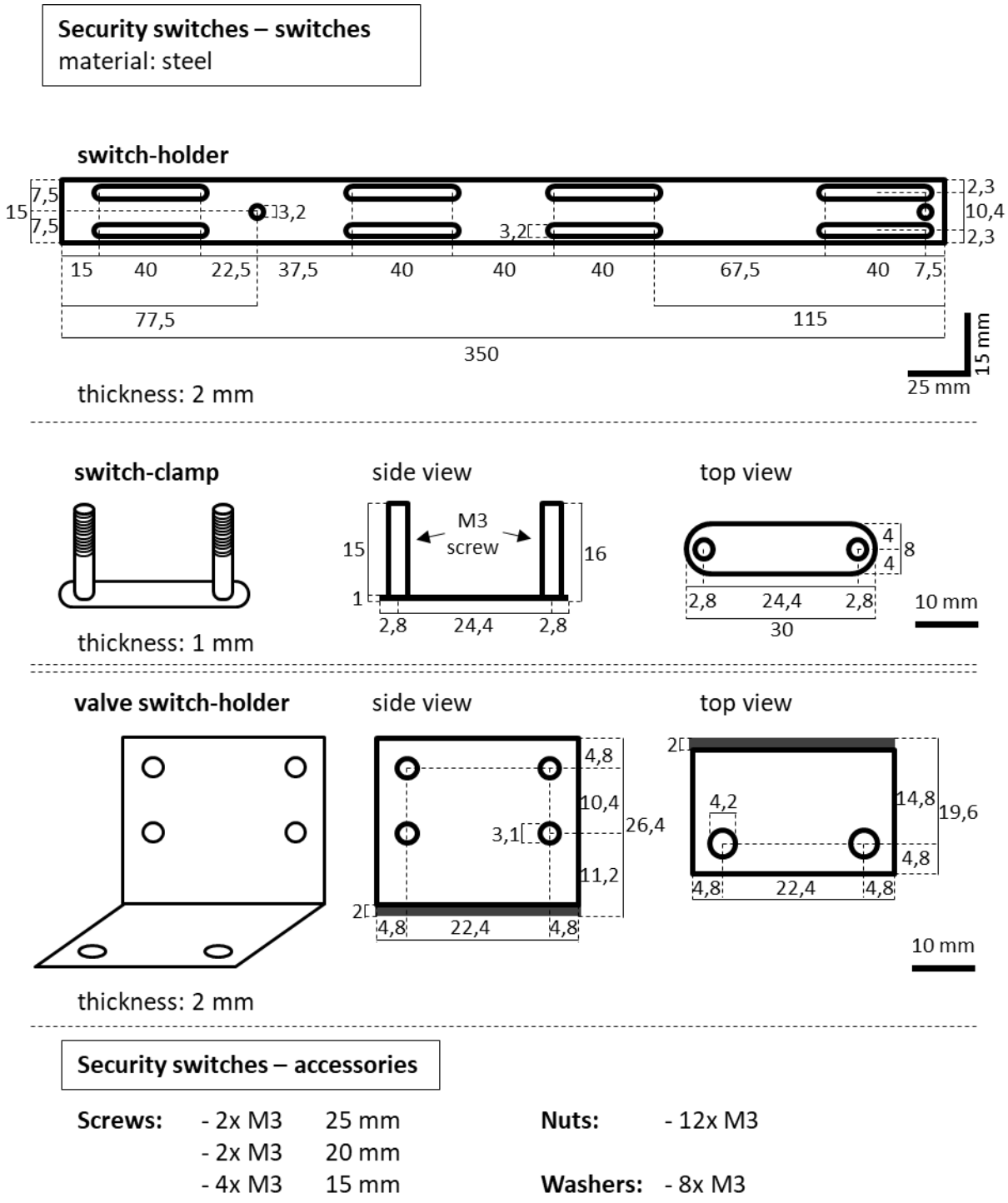

Figure A7: Technical drawings for the security switches for the manipulator z-drive.

7.1. Publications

7.1.1. [P1]

Atomic Force and Scanning Tunneling Microscopy of Ordered Ionic Liquid Wetting Layers from 110 K up to Room Temperature

M. Meusel, M. Lexow, A. Gezmis, S. Schötz, M. Wagner, A. Bayer, F. Maier, and H.-P. Steinrück, *ACS nano*, *14*, 9000-9010 (**2020**), 10.1021/acsnano.0c03841

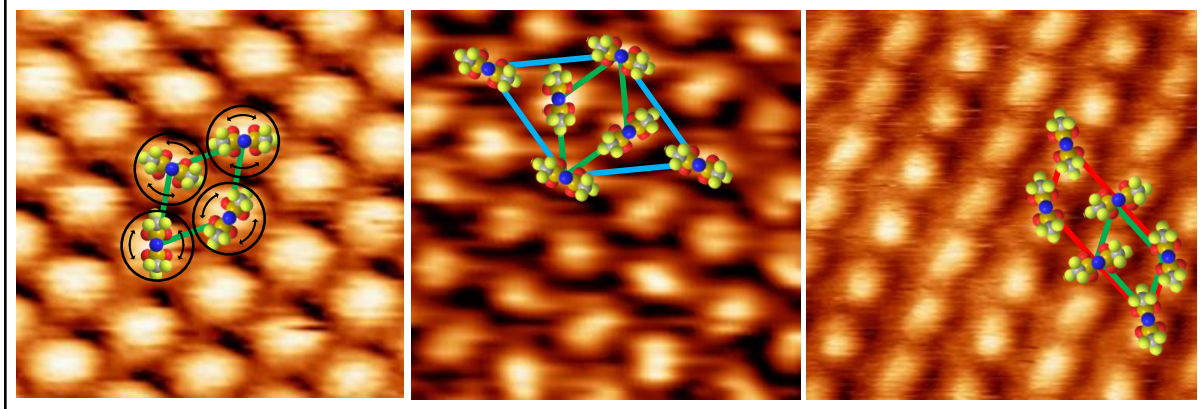

7.1.2. [P2]

GROWTH OF MULTILAYERS OF IONIC LIQUIDS ON Au(111) INVESTIGATED BY ATOMIC FORCE MICROSCOPY IN ULTRAHIGH VACUUM

M. Meusel, M. Lexow, A. Gezmis, A. Bayer, F. Maier, and H.-P. Steinrück, *Langmuir, 36,* 13670-13681 (**2020**), 10.1021/acs.langmuir.0c02596

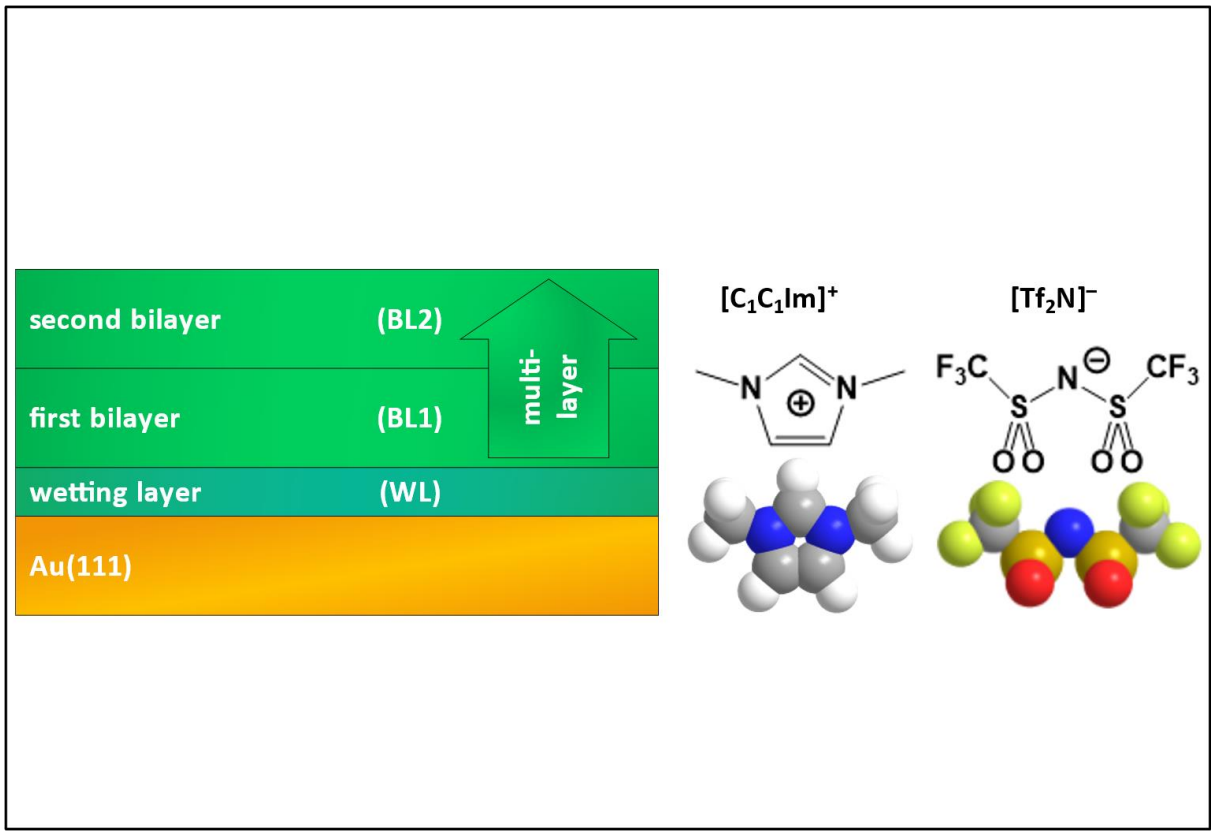

7.1.3. [P3]

TIME- AND TEMPERATURE-DEPENDENT GROWTH BEHAVIOR OF IONIC LIQUIDS ON Au(111) STUDIED BY ATOMIC FORCE MICROSCOPY IN ULTRAHIGH VACUUM

M. Meusel, A. Gezmis, S. Jaekel, M. Lexow, A. Bayer, F. Maier, and H.-P. Steinrück,

J. Phys. Chem. C, 125, 20439-20449 (**2021**), 10.1021/acs.jpcc.1c06613

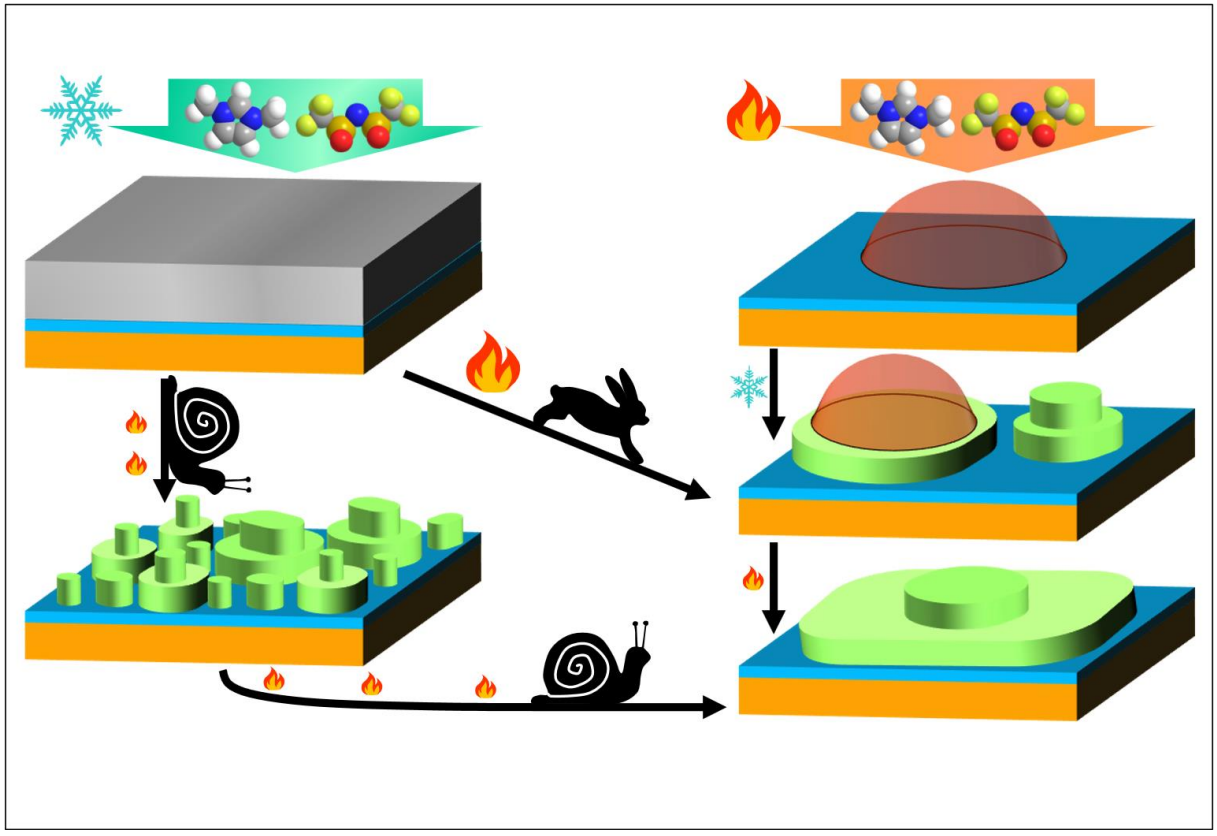

7.1.4. [P4]

GROWTH AND STABILITY OF Pt NANOCLUSTERS FROM 1 TO 50 ATOMS ON h-BN/Rh(111)

F. Düll*, M. Meusel*, F. Späth, S. Schötz, U. Bauer, P. Bachmann, J. Steinhauer, H.-P. Steinrück, A. Bayer, and C. Papp, *Phys. Chem. Chem. Phys., 21*, 21287-21295 (**2019**), 10.1039/C9CP04095A,

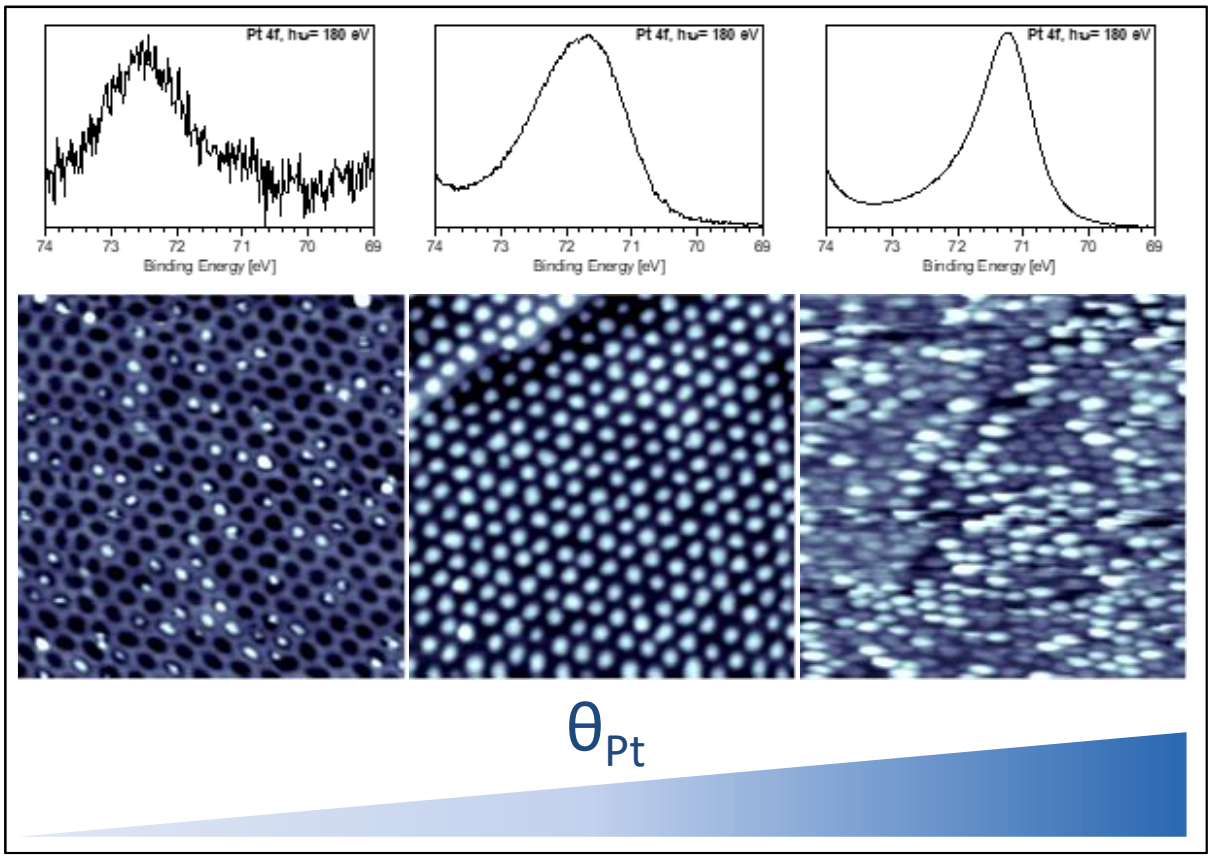

*shared first-authorship. The author's contribution is the STM part.